Stark spectroscopy on rare gas atoms

Document Version:
Publisher's PDF, also known as Version of Record (includes final page, issue and volume numbers)

Please check the document version of this publication:

• A submitted manuscript is the version of the article upon submission and before peer-review. There can be important differences between the submitted version and the official published version of record. People interested in the research are advised to contact the author for the final version of the publication, or visit the DOI to the publisher's website.
• The final author version and the galley proof are versions of the publication after peer review.
• The final published version features the final layout of the paper including the volume, issue and page numbers.

Link to publication

Stark spectroscopy
on rare gas atoms

PROEFSCHRIFT

ter verkrijging van de graad van doctor aan de
Technische Universiteit Eindhoven, op gezag van de
Rector Magnificus, prof.dr.ir. C.J. van Duijn, voor een
commissie aangewezen door het College voor
Promoties in het openbaar te verdedigen
op maandag 20 november 2006 om 16.00 uur

door

Tao Jiang

geboren te Shaanxi, China

Dit proefschrift is goedgekeurd door de promotoren:

prof.dr.ir. G.M.W. Kroesen
en
prof.dr.ir. H. Tolner

Copromotor:
dr.ir. E. Stoffels-Adamowicz

To my lovely wife, Xiangming Cheng.

Contents

Chapter 1

Inroduction

1.1 Plasma

Plasma, in contrast to solids, liquids and gases, is an ionized gas. It was first identified in a discharge tube and called "radiant matter" by W. Crookes in 1879 [1]. It hadn't been named as "Plasma" until the year of 1927 by Irving Langmuir [2], who wrote:

> "Except near the electrodes, where there are *sheaths* containing very few electrons, the ionized gas contains ions and electrons in about equal numbers so that the resultant space charge is very small. We shall use the name *plasma* to describe this region containing balanced charges of ions and electrons"
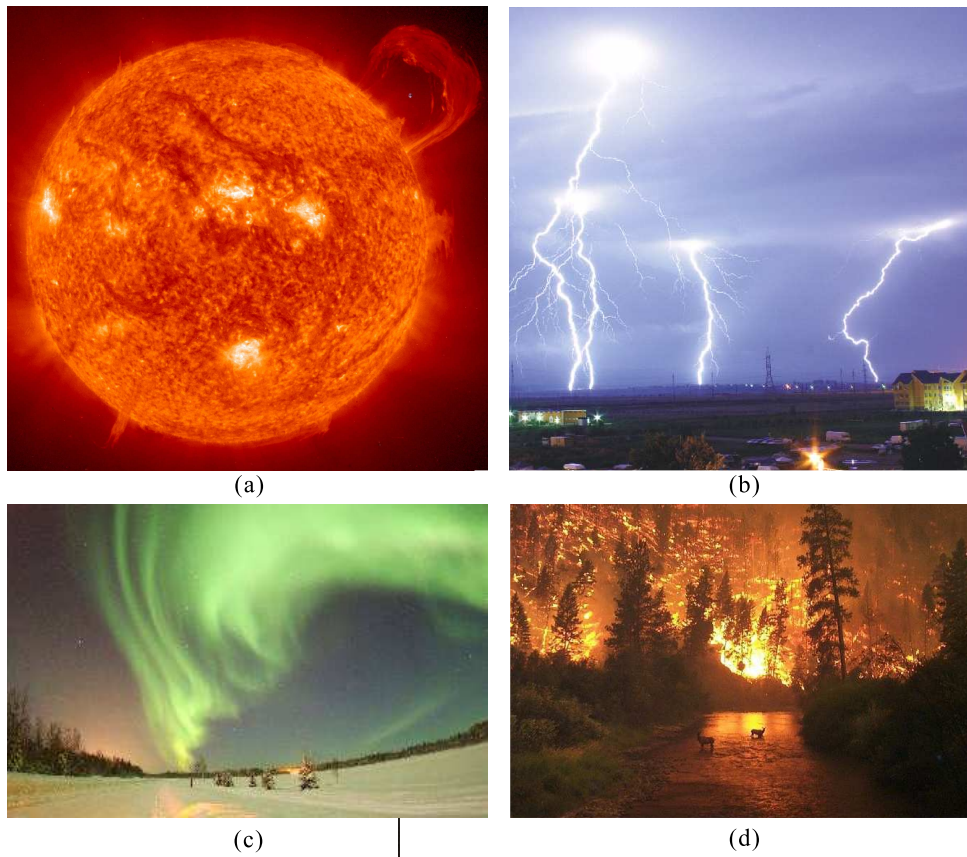
Figure 1.1: Plasmas in nature. (a) A photo of the sun taken by NASA. (b)Lightning over Oradea Romania taken by M. Madau. (c) The Aurora-Polar light; author unknown (d)Forest fire in Bitterroot National Forest in Montana, USA, on Aug. 6th, 2000 by John McColgen.

There are many different types of plasma in nature such as the sun, the aurora, lightning and fire (see the figure 1.1). Over 99% of the entire visible universe is in the plasma state [3].

Plasma also can be created in artificial devices, such as in discharge lamps, plasma display panels for large-size flat TV's, Hall thrusters used for space applications and the plasma needle for new biomedical treatment methods (see figure 1.2)
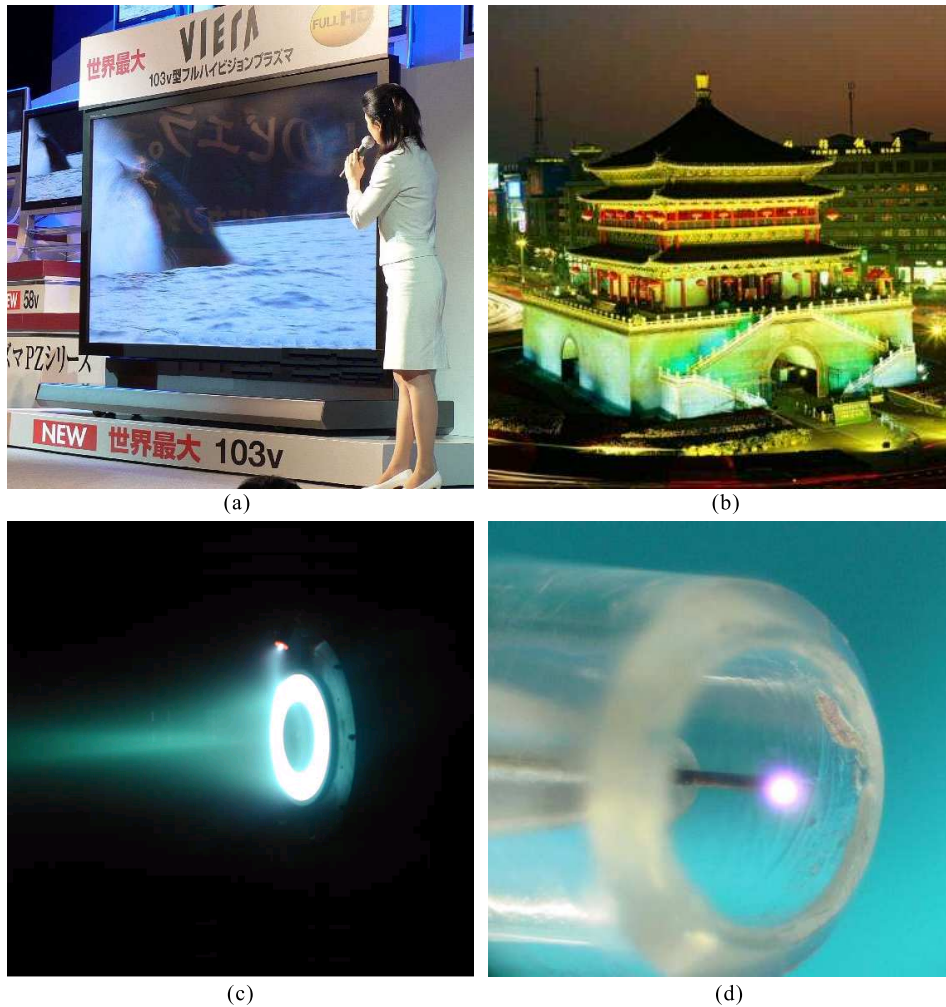
Figure 1.2: Man-Made Plasma. (a) The Wall-hanging Plasma display panel with 103-inch diagonal screen made. (b)Lamps lighting an old building with more than 600 years history in Xi'an China. (c) 2kW laboratory Hall thruster in operation at the Princeton Plasma Physics Laboratory. (d) Plasma needle developed at Eindhoven University of Technology.

1.2 Outline of the thesis

In order to improve the applications of plasma, we should know how plasmas are created and sustained. Diagnostics of the bulk parameters in plasmas is one of the major challenges.

The electric field in the plasma, especially in the boundary, is one of the most important parameters. It is the driving force behind many processes and also connects to other parameters, such as the charge density. There are only few methods available to measure the electric field. Commonly, Langmuir probes are applied. The main problem with this technique is the perturbation of the plasma by the presence of the probe, and also the emission or absorption of charges. Another method for electric field measurement is Stark spectroscopy.

The Stark effect is the splitting and shifting of a spectral line of an atom or molecule in the presence of an electric field. The effect is named after Johannes Stark, who discovered it in 1913. It was independently discovered in the same year by the Italian physicist Antonino Lo Surdo, and it is sometimes called the Stark-Lo Surdo effect.

The advantage of measuring the electric field by monitoring the emission lines of a plasma is that it is non-perturbative and can also give good spatial and temporal resolution. However, most of the emission lines in a plasma relate to the lower energy levels of atoms, which are not sensitive to the electric field. So the method is only useful if the electric field in the plasma is high enough.

Some of the higher energy levels of atoms are sensitive to the electric field, so we can measure the electric field by exciting the atoms to these higher energy levels and monitor the transitions related to these levels.

A laser is a near-monochromatic and high energy density light source, but the wavelength of common lasers is fixed, so they can not be used for the purpose of exciting atoms to a higher level. It wasn't until the 1970's that the dye laser, a tunable laser, was invented, which has made it possible to accurately measure the energy levels of atoms and molecules.

Chapter 2 and 3 introduce the active measurement methods for determining electric fields in plasmas by means of laser excitation.

Plasma breakdown is the process that occurs when an electrically neutral gas absorbs enough energy to become ionised and electrically conducting. Normally the time of breakdown is very short, from 10^{-9} to 10^{-3} second, so it is difficult to study because of the highly transient nature. Chapter 4 of this thesis deals with the breakdown in 3 different cases by detecting optical emission by means of a fast camera.

Plasmas for biomedical treatment is a new application and research area. Applying a plasma for medical treatments demands that the plasma should be operated at atmospheric pressure and at low temperature, without thermal damage to the living materials. It is a

challenge to create this kind of plasma because normally the non-equilibrium (non-thermal or "cold") plasma can be easily obtained at low pressure, but difficult at atmospheric pressure. Recently, several atmospheric cold plasmas have been reported in the literature [4–7], and we have also developed an atmospheric helium dielectric surface discharge panel with a low operation voltage. In chapter 5 of this thesis we introduce the development of atmospheric cold plasmas and its potential applications in biomedical technology. Furthermore, we will discuss the design and operation of helium atmospheric plasmas created by a Micro Plasma Array Plate, and the analysis of the electric and optical measurement results on this plate.

References

[1] Crookes. Crookes presented a lecture to the British association for the Advancement of Science, in Sheffield on Aug. 22th 1879.

[2] I. Langmuir. Oscillations in ionized gases. *Proc. Nat. Acad. Sci. U.S.*, 14:628, 1928.

[3] D. A. Gurnett and A. Bhattacharjee. Introduction to plasma physics. *Cambridge university press ISBN: 0521364833*, 2005.

[4] J. Waye. Delivery system for argon coagulator offers non-contact method for control of GI bleeding. *Gastroenterology Endoscopy News, June*, 1997.

[5] V. Léveillé and S. Coulombe. Design and preliminary characterization of a miniature pulsed RF APGD torch with downstream injection of the source of reactive species. *Plasma Sources Sci. Technol.*, 14:467–476, 2005.

[6] R. Pompl, T. Shimizu, H.-U. Schmidt, W. Bunk, F. Jamitzky, B. Steffes, K. Ramrath, B. Peters, W. Stolz, T. Urayama, R. Ramasamy, S. Fujii, and G.E. Morfill. *Proc. 6th International conference on Reative Plasma and 23rd Symposium on Plasma Processing, Matsushima/Sendai, Japan, January 24-27*, 2006.

[7] E. Stoffels, A.J. Flikweert, W.W. Stoffels, and G.M.W. Kroesen. Plasma needle: a non-destructive atmospheric plasma source for fine surface treatment of (bio)materials. *Plasma Sources Sci. Technol.*, 11:383–388, 2002.

Chapter 2

Diagnostics of the E-field in plasma using Stark spectroscopy of Kr and Xe atoms

Abstract

We report the development of laser diagnostic techniques based on Stark spectroscopy of xenon and krypton atoms. Measurement of Stark spectra from the sheath regions of glow discharges were performed, and experimental results were compared to theoretical calculations by solving the Schrödinger equation for xenon and krypton atoms. A good agreement between the calculation results and experimental results for the excitations from $5s$ to nf for krypton and $6s$' to nf for xenon was achieved. Furthermore we found that energy levels of higher p states of krypton atoms were also clearly shifted in the presence of an electric field.

2.1   Introduction

The electric field is one of the most important discharge parameters. In glow discharges, it is the driving force behind many processes at the boundary of the glow region. Many applications that employ discharges depend on the behaviour at the boundary. Furthermore, the electric field is closely connected with other discharge parameters, such as charge densities, fluxes of electrons and ions, and energy distribution functions. It also serves as input data for plasma discharge modelling. However, although it is necessary to understand the spatial distribution of the electric fields in the discharge, electric fields are still difficult to measure.

One well known way of measuring the electric field in a plasma is by an electrical probe, the Langmuir probe. However, the main problem for using probes is the perturbation of the plasma by the probe used. The probe tip must be inside the plasma, where it can interact with charged particles. The probe itself will change the electric field in the very region where one wants to measure.

Another way of measuring electric fields is by detecting the plasma emission. The basic idea of this method is that the energy levels of atoms and molecules in an electric field are modified due to the Stark effect. This effect can cause splitting of degenerate energy levels, some normally forbidden transitions can partially allow and can shift some energy levels. The electric field can thus be measured by monitoring the plasma emission related to these energy levels. However, these passive methods can only give reliable results when the electric field strength is more than few or few hundreds kV/cm [1], because the transitions observed are often related to levels with small principal quantum numbers, and these energy levels are not very sensitive to the electric field.

An active method to observe the Stark effect is laser spectroscopy. The high energy photons emitted by a laser can excite the target atoms to highly-excited Rydberg states. Because these states are more sensitive to the electric field, the Stark effect can be observed more easily.

Zimmerman et al [2] used laser spectroscopy to investigate the Stark effect in alkali atoms and compared their calculations to experiments. K.A.H. van Leevwen et al investigated the Stark effect in barium atoms, BaI and CaI [3–6]. Kelleher and Saloman [7] extended Zimmerman's work to barium, and subsequent investigations applied this method to investigate the Stark effect in krypton (Delsart and Keller [8]), in argon (Brevet et al [9]) and in xenon (Ernst et al [10] and Knight and Wang [11]). However, none of these investigations observe the Stark effect directly in the plasma.

Moore et al [12] were the first to use the Stark effect to measure the electric field in a glow discharge in BCl. A similar method was applied to a helium glow discharge by

Doughty et al [13] and Ganguly et al [14]. An accuracy 4V/cm was reported [14]. They were extended to argon by Gavrilenko et al [15], with an accuracy of 60V/cm. Other investigators [16–22] have developed electric field diagnostics, such as Booth et al [23] using $2+1$ photon laser Stark spectroscopy for an rf hydrogen discharge, Choi et al [19] in an argon glow discharge using laser induced fluoresence (LIF) and laser optogalvanic spectroscopy, and Czarnetski et al [20] using laser induced fluorescence dip spectroscopy for a hydrogen rf discharge, for which an accuracy of 5V/cm was reported.

The aims of this research are to examine the Stark effect in xenon and krypton atoms, determine the suitability of this principle as a diagnostic for electric field measurement in a plasma, and to verify the applicability of the theoretic calculations developed for argon atoms by Gavrilenko et al [15]. To do this, we measured the Stark effect in the sheath of a DC glow discharge of xenon and krypton using laser optogalvanic spectroscopy. The laser excitations are from metastables to nl states of xenon and krypton atoms which orbit quantum number $l \geq 3$. The experimental results were compared to theoretical calculations in order to determine the electric field strength.

The structure of this chapter is as follows. Section 2 contains a description of the experimental system and the results. In section 3, the method of calculation will described and will give a short discussion on the calculated results. In section 4, we compare the experimental and calculated results. A brief conclusion is given in Section 5.

2.2 Experiment

Laser optogalvanic (LOG) spectroscopy in a plasma is based on the detection of laser-induced excitation of atomic or molecular energy levels by monitoring the current through the plasma. In this process, atoms or molecules are excited to high-lying Rydberg energy levels, the so-called Rydberg states[1], which are easily ionized by collisions. This reduces the plasma resistance and increases the plasma current. By scanning the excitation wavelength, various excited states can be detected.

The spectroscopic scheme used in this work is shown in figure 2.1. Laser excitation of the xenon atom was performed from the metastable level $6s'[1/2]_0$ to nf Rydberg levels. The fact that lower level $6s'[1/2]_0$ is mixed with the $5d[1/2]_0$ [18] allows for excitation from the metastable state to nf Rydberg states. A similar structure in krypton enables laser excitation from $5s[3/2]_2$ (mixed with $4d[3/2]_2$) to nf Rydberg states.

---

[1]Rydberg state is a state of an atom or molecule in which one of the electrons has been excited to a high principal quantum number orbital, of which the dimensions are very large compared to the size of the ion core. The state is similar to a hydrogen atom, so it also called a hydrogen-like atom.
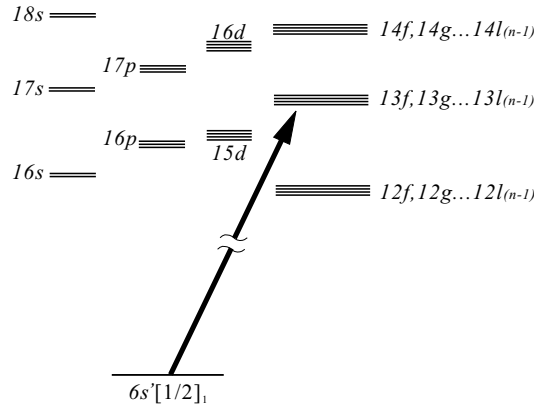
Figure 2.1: Scheme of partial energy levels of a xenon atom, arrow indicates laser excitation.

2.2.1 Experimental arrangement

Experimental set-up for xenon

The experimental arrangement is schematically shown in figure.2.2

The electrodes were round stainless steel plates with a diameter of 4cm, placed parallel and separated by 10 mm. Pure xenon gas ($\geq$ 99.998%) at 2.4×10^3 Pa pressure was used. A DC voltage was applied between the electrodes (figure 2.3). The discharge is close to an abnormal glow discharge for stability of the discharge. The voltage between the two electrodes is about 350 V.

A tunable dye laser (Lambda Physik LPB3002), pumped by an excimer laser, was operated at $\sim$ 480nm (Dye: Coumarin 102). The laser pulse duration was about 5ns and the spectral width was $\sim$ 8 pm. A cylindrical lens was used to focus the laser beam into a sheet-like beam with a thickness of about 0.15 mm and a width of about 4 mm. The laser beam was directed through the sheath of the plasma parallel to the electrode surfaces. The excitation pulse energy was near 1 mJ.

The voltage between the electrodes was monitored with a high pass filter which is connected to a data acquisition system. The data acquisition system sampled the voltage signal as a function of the time. A delay generator was used to synchronize the laser and data acquisition system. Measurements were performed by scanning the dye laser wavelength and measuring the plasma current (LOG signal). The accuracy of laser wavelength is about 3 pm (it can be calibrated by scanning the known zero field transition in a discharge).
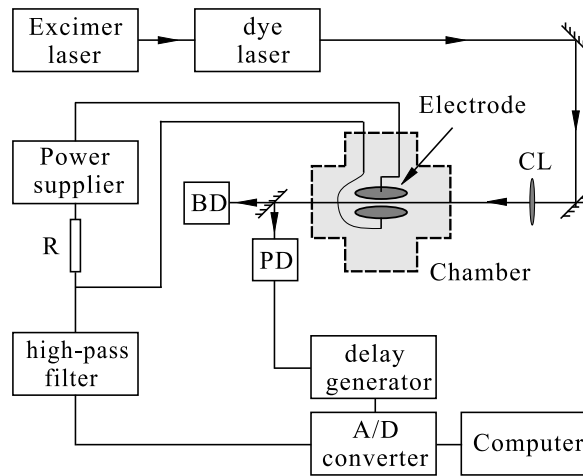
Figure 2.2: Experimental apparatus for LOG measurements in a DC glow discharge, BD is laser beam dump, PD is a photodiode and CL is cylinder lens. R is a 20 kΩ resistance for current limited.
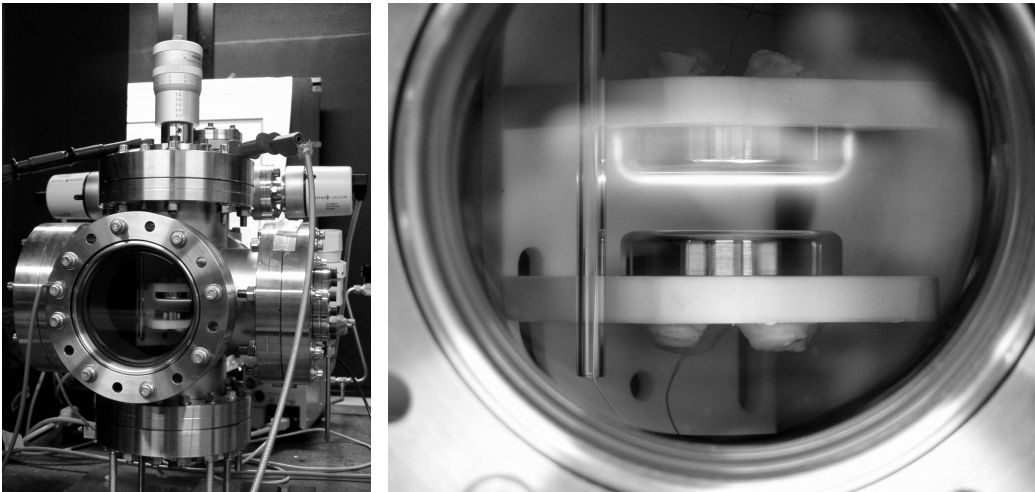
Figure 2.3: Experimental apparatus for LOG measurements in a DC glow discharge, left: vacuum vessel, right: discharge between two parallel plates and the direction of the electrical field in sheath is vertical.

Experimental set-up for krypton

The experimental set-up for krypton is similar to that of xenon. The difference in the laser system was that the pumping laser was replaced by a Nd:YAG laser (Continuum Powerlite 8000) at 532nm. The dye laser was operated at wavelengths from 611 to 662nm

(The laser dye: Rhodamine 101) and its frequency was doubled to generate radiation which wavelength from 306 to 330nm. The pulse energy of the excitation laser was about 1 mJ. The vacuum chamber was filled with 99.99% pure krypton gas at a pressure of 700 Pa.

2.2.2   Experimental results

LOG Spectroscopy

Laser optogalvanic (LOG) spectroscopy in a plasma is performed by using the laser photons for exciting atoms or molecules from a lower energy level to a higher level, which can easily be ionized by collisions. This will induce an increase of the density of charged particles in the plasma. The process will reduce the plasma resistance and increases the plasma current. Figure 2.4 shows a curve of the plasma current (LOG signal) as function of time after the laser pulse is sent into the krypton plasma. The distance of the laser beam to the cathode is 0.1 mm. There is a small current increase after the 311.3nm pulse is sent into the krypton plasma, even if there is no energy gap between two levels of krypton atom that equals to the energy of the laser photon. This occurs because the laser photon can ionize some highly excited krypton atoms in the plasma by colliding with them. However, a larger number of these krypton atoms can be excited to a high Rydberg state when the energy of the laser photon is equal to the gap of the two energy levels and the transition is allowed by the selection rules. Then they will collide with other particles in the plasma. Subsequently, a larger plasma current can be observed. The top curve in figure 2.4 is the consequence of a the laser photon with wavelength 311.437nm exciting krypton atoms from $5s[3/2]_2$ to $12p[3/2]_2$.

By scanning the excitation wavelength, various excited states can be detected.

Figure 2.5 shows the typical experimental LOG spectra for krypton atoms. In this case the laser was scanned from 315.3nm to 315.6nm with a step of 1pm, and for each wavelength the data of LOG spectrum was averaged by 50 laser shots. The increase of the LOG signal coinciding with the laser pulse and the relaxation of the laser-induced plasma current are visible. The intensity rise is small when no transition is allowed at the laser wavelength, but a stronger signal can be observed when the photons can excite the atoms from a lower energy level to a higher one. The two peaks in figure 2.5 (a) correspond to the transitions of krypton atoms from $5s[3/2]_2$ to $12p[3/2]_2$ and $12p[5/2]_3$, respectively. Excitation spectra can be obtained by averaging the LOG signal between 0.8 and 1.6 μs after the laser shot. The result of the averaging is shown in figure 2.5 (b).

Figure 2.6 shows a laser scan from 314-323nm in a krypton discharge. The distance of the laser beam to the cathode is 0.1mm . The stronger transitions from the metastable state $5s[3/2]_2$ to 12 and 13p are observed, and the transitions from the metastable state to
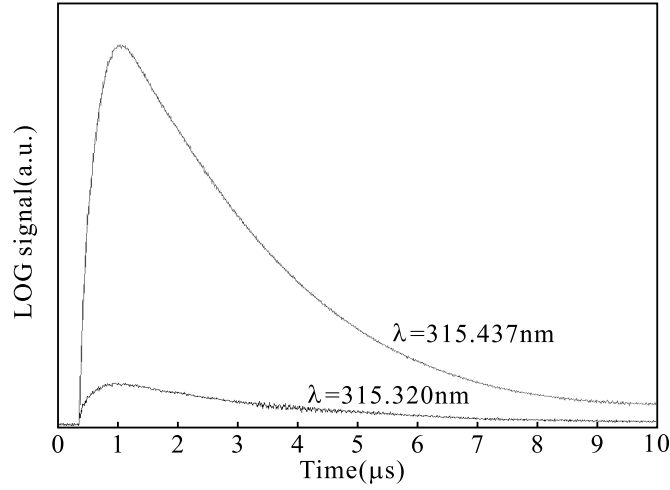
Figure 2.4: The plasma current signals obtained after the laser pulse is sent to the sheath of a krypton discharge

$8f$ and $9f$ can also be recognized, as well as some other transitions from $5s[3/2]_1$ to 13',14' and $15p$'.

Experimental results for xenon

Figure 2.7 shows the LOG spectra obtained in a xenon glow discharge: (a) and (b) are the sets of spectra excitations from $6s'$ state to $10f$ and $13f$ for xenon different positions to the cathode. The main features of the experimental spectra in figure 2.7 are:

1. When the laser beam is far from the cathode (d>2.1mm) the electric field is low, approaching zero. The LOG spectrum shows a single peak which is corresponding to the $6s'[1/2]_0$ to $nf[3/2]_1$ transition.

2. In the vicinity of the cathode, where the electric field is strongest, the spectra show many peaks, because the Stark effect restructures the energy levels.

3. The number of spectra peaks increases with increasing principal quantum number n (also see the experimental spectra in figure 2.11), as expected.

4. The intensity of the LOG signal near the cathode is much larger than far from the cathode, because the electrons produced by laser excitation can be accelerated throughout almost all of the sheath. These electrons can get more energy from the electrical field to create more ionizations. Therefore, a stronger LOG signal was obtained.
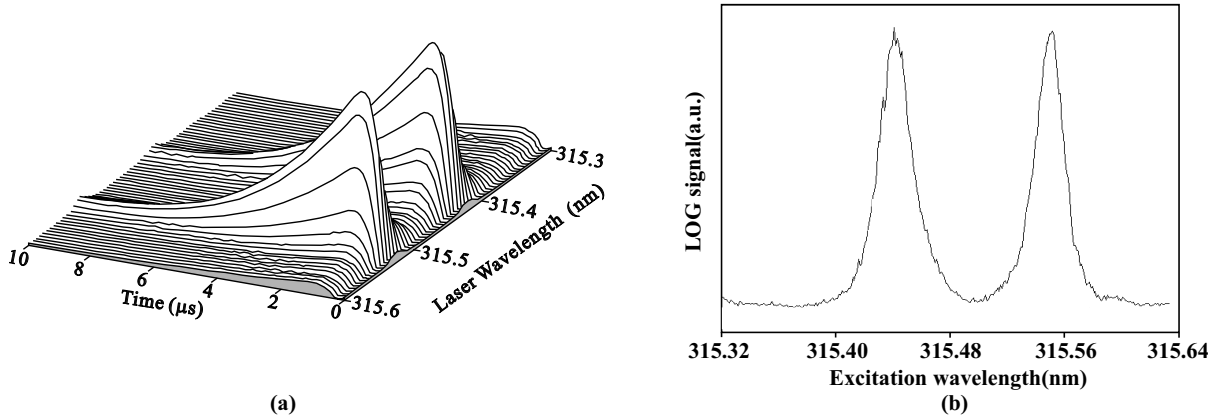
Figure 2.5: (a) Three dimensional plot of the LOG signal (laser-induce plasma current) while scanning the laser wavelength over the $5s[3/2]_2$ to $12p[3/2]_2$ and $12p[5/2]_3$ transitions of krypton atoms. The front axis shows the laser wavelength, the side axis is the time after laser excitation, and the vertical axis is the measured voltage(the convertor of plasma current by a resistance). (b) the resulting excitation spectrum is plotted by an averaging method described in Section.2.2.2

5. In spectra with many peaks, the central peaks are narrower than the peripheral ones. This is related to the spatial profile of the laser beam. Further discussion of this phenomenon is given in Section 5.

Experimental results for krypton

Figure 2.8 shows the LOG spectra obtained in a krypton glow discharge: (a) is the set of spectra resulting from excitation from the $5s$ state to $8f$ and (b) corresponds to excitation to $10f$, and shows spectra at different distances from the cathode. Most features of the experimental spectra are similar to the xenon features, such as many Stark components in high field, higher LOG signal obtained near the cathode etc. When the distance of the laser beam to cathode is larger than ≥ 1.1mm, the electric field is lower (near zero). Unlike the case of xenon, the LOG spectra of krypton for zero electric field or near zero electric field show the undisturbed transitions. Two peaks corresponding to the fine structure are present in figure 2.8 (a) and (b), corresponding to the transitions from $5s[3/2]_2(4d[3/2]_2)$to $nf[3/2]_{2,3}$ and $nf[5/2]_{1,2}$ (here (a) $n = 8$ and (b) $n = 10$).

14
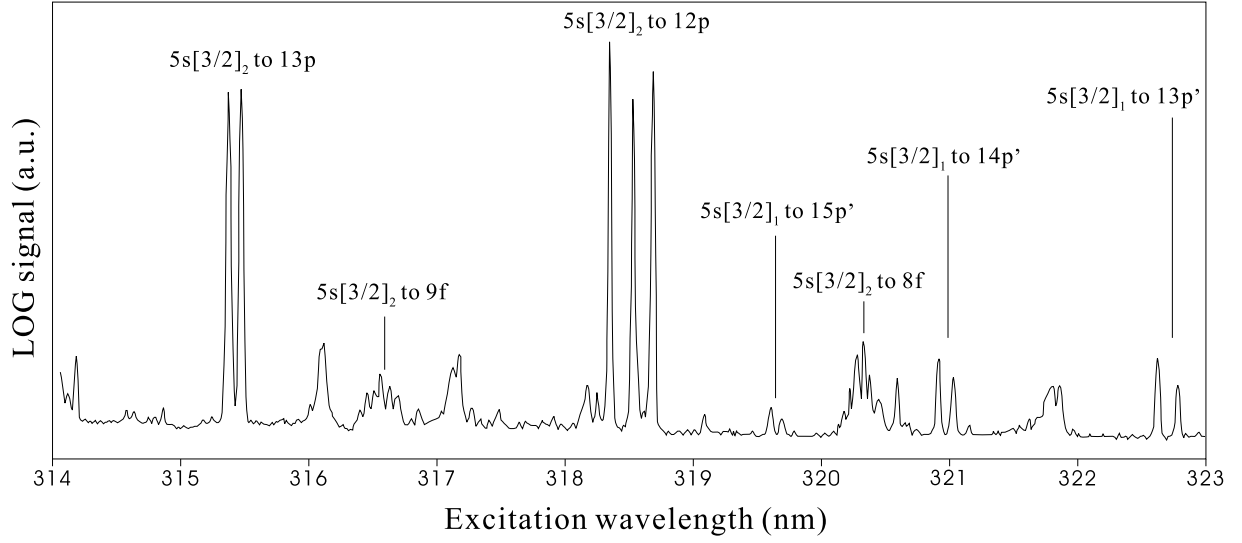
Figure 2.6: Scheme of partial energy levels of a krypton atom obtained by LOG method.
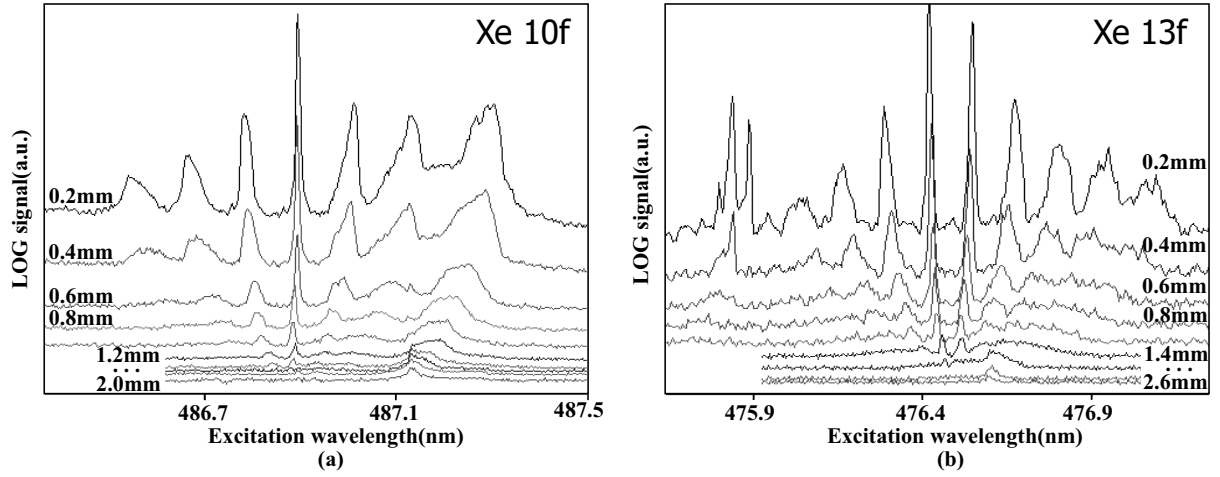
Figure 2.7: The LOG spectra obtained in a xenon discharge: (a) and (b) are the sets of LOG spectra excitations from $6s'$ state to $10f$ and $13f$. The top spectrum in each figure was measured 0.2mm from the cathode, and others were obtained with a step 0.4mm.

2.3   Theoretical calculations

To determine the electric field in a plasma using Stark spectroscopy, the observed spectra need to be compared to spectra which are either calculated theoretically or obtained by experiments with known electric fields. In this section, a theory calculation on the Stark
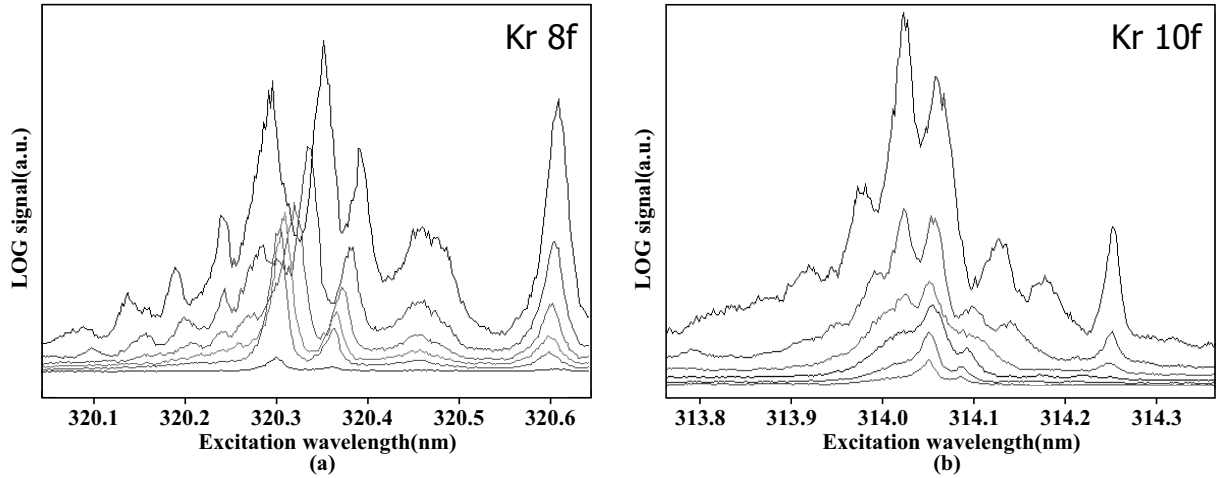
Figure 2.8: The LOG spectra obtained in a krypton discharge: (a) and (b) are the sets of LOG spectra excitations from $5s$ state to $8f$ and $10f$. The top spectrum in each figure was measured 0.2mm from the cathode, and others obtained with a step 0.2mm.

effect is discussed.

2.3.1 Calculation method

To calculate the Stark effect of energy levels of Rydberg states of rare-gas atoms, the time-independent Schödinger equation needs to be solved:

$$H\psi = E\psi \tag{2.1}$$

here H is the Hamiltonian of the system, ψ is the electron wave function and E is the corresponding energy level. Solving this equation theoretically is difficult. However, if the rare gas atom is considered as hydrogen-like, the equation can indeed be solved.

If an electric field F is present, the interaction of this atom with the electric field F can be described approximately as a dipole interacting with an electric field and the Hamiltonian of the system can be written as:

$$H = H_0 + H_{Stark} = H_0 + eFz \tag{2.2}$$

where H_0 is the unperturbed Hamiltonian. Mathematically, the Hamiltonian H can be expressed in a matrix form. Therefore, the unperturbed Hamiltonian H_0 is a diagonal matrix and the diagonal elements are the zero-field energy levels. For calculating the Stark effect on the nf states, the Stark coupling between the nf states and energy levels in the vicinity have to be considered. Therefore, the elements of the unperturbed Hamiltonian H_0 matrix

should not only include the energy levels excited by the laser, but also the neighboring Rydberg states, such as ng, ..., nl_{n-1}.

Some s, p or d levels should also be included in the matrix if they are very close to the nf states. Some of these zero-field energy levels, such as ns, np, nd and nf, can be found in the literature [24, 25], but others, such the levels ($l \geq 4$), have to be calculated.

The jK coupling scheme is applied for the Rydberg states of krypton and xenon atoms [26, 27]. However, this scheme has some deficiencies [11]. In this scheme, there is a strong coupling between the orbital angular momentum **l** of the Rydberg electron and the total angular momentum of the ion core **j$_c$**. This coupling is described by the angular momentum $\mathbf{K} = \mathbf{j_c} + \mathbf{l}$. The total angular momentum of the atom is then described by $J = K \pm s$, where s is the spin of the Rydberg electron.

The energy level corresponding to quantum numbers n, l, K, and j can expressed as follows [7] :

$$E_{nlKj} = E_m(nl) + \Delta E \tag{2.3}$$

where the $E_m(nl)$ is the mean energy with principal quantum number n and degenerate level l for the quantum defect δ_{nl} [1], and ΔE is the electrostatic fine-structure splitting around the mean energy.

Table 2.1: List of the Quantum defects for different orbit quantum number of xenon atom.

s	p	d	f	g	l≥5
4.00±0.02	3.52±0.09	2.37±0.16	0.036	0.004	0

The mean energy levels can be described by the Rydberg hydrogen formula:

$$E_m(n,l) = \frac{E_{ion}}{(n - \delta_{nl})^2} \tag{2.4}$$

where E_{ion} is the first ionization limit. The quantum defect δ_{nl} is very close to zero when the orbit quantum number $l \geq 4$, so we chose $\delta_{nl} = 0.004$ when $l = 4$, and $\delta_{nl} = 0$ when $l \geq 5$. Table 2.1 shows the approximate quantum defects for different orbit quantum number of xenon atom.

---

[1]The Rydberg electrons of a heavy noble gas atoms with low l values have orbits that pass through the core region of shielding electrons, unlike the Rydberg electron in hydrogen. The influence of these penetrating is taken into account by a correction term in Rydberg equation, called "quantum defect". [28]

The electrostatic fine-structure splitting about the mean energy ΔE can be written as follows [29]:

$$\Delta E = -\frac{6h^2 + 3h - 2j(j+1)l(l+1)}{4j(j+1)(2l-1)(2l+3)} \langle r_c^2 \rangle \langle r^{-3} \rangle \tag{2.5}$$

and

$$h = \frac{1}{2}[K(K+1) - j(j+1) - l(l+1)]. \tag{2.6}$$

the mean value $\langle r^{-3} \rangle$ can be approximated by the hydrogenic formula [29]. $\langle r_c^2 \rangle$ is the mean-square radius of the ion core, which can be calculated using experimental values of zero-field energy levels of nf available in the literature [9].

According to the jK coupling scheme, the energy levels are therefore denoted as $nl[K]_J$, and the unperturbed wave functions of the energy levels of rare gas atoms can be denoted as $\varphi = |nl[K]_J\rangle$.

The diagonal elements of the Hamiltonian H are the unperturbed energy levels. The off-diagonal elements, describing the interaction, can be calculated by the integral:

$$\langle (nlj_c)KsJM|z|(n'l'j_c')K'sJ'M'\rangle$$

$$= (-1)^{J+J'+K+K'+l+j_c+s-M}[(2J+1)(2J'+1)(2K+1)(2K'+1)]^{1/2}\delta_{MM'}$$

$$\times \begin{pmatrix} J & 1 & J' \\ -M & 0 & M' \end{pmatrix} \begin{Bmatrix} K & J & s \\ J' & K' & 1 \end{Bmatrix} \begin{Bmatrix} l & K & j_c \\ K' & l' & 1 \end{Bmatrix} \langle nl\|r\|n'l'\rangle$$

where $j_c = \frac{3}{2}, s = \frac{1}{2}$, M is the quantum number of the projection of J onto the axis z, $\delta_{MM'}$ is the Kronecker delta symbol, $\begin{pmatrix} j_1 & j & j_2 \\ m_1 & m & m_2 \end{pmatrix}$ is the 3j symbol, and $\begin{Bmatrix} j_1 & j & j_2 \\ m_1 & m & m_2 \end{Bmatrix}$ is the 6j symbol. For the calculation method of the 3j and 6j symbols see [30]. These symbols are connected to the selection rules and the integral will only give a result when the two wave functions are compatible with the selection rules for dipole transitions for the jK coupling as follows:

$$\Delta J = \pm 1 \quad \text{for} \quad M = 0, \quad \Delta J = 0, \pm 1 \quad \text{for} \quad M \neq 0,$$
$$\Delta K = 0, \pm 1, \qquad \Delta l \pm 1,$$

$\langle nl\|r\|n'l'\rangle$ is the reduced matrix element:

$$\langle nl\|r\|n'l'\rangle = \begin{cases} -(l+1)^{1/2}\langle nl|r|n', l'+1\rangle, & l' = l+1 \\ l^{1/2}\langle nl|r|n', l'-1\rangle, & l' = l-1 \end{cases} \tag{2.7}$$

The radial matrix elements $\langle n, l+1|r|nl \rangle$, can be calculated using the table of Edmonds et al. [31]. For small n, such as 8-11, however, the s, p and d levels are not close to the f levels and the levels with $l \geq 4$, so the coupling between them can be ignored. Therefore, the radial matrix elements can be calculated using the hydrogenic formula [29]:

$$\langle n, l+1|r|nl \rangle = (3n/2)[n^2 - (l+1)^2]^{1/2}a_0, \qquad (2.8)$$

where a_0 is the Bohr radius. This is due to the fact that for the nl configurations with $l \geq 3$, the quantum defects δ_l are small (i.e., $\delta_l \ll 1$). Therefore, we used the hydrogenic formula, shown above, for the matrix elements $\langle n, l+1|r|nl \rangle$ with $l \geq 3$ ($n<12$) while solving Eq2.1.

Solving Eq2.1 can be performed by diagonalizing the matrix of the Hamiltonian H. The eigenvalues of H obtained by diagonalizing the matrix elements of the total Hamiltonian $H = H_0 + H_{Stark}$. When the matrix is diagonalized, a new basis set of wave functions is found with corresponding energy levels. The wave functions are expressed as:

$$\psi_\mu^{(n,M)}(F) = \sum_{l=0}^{n-1} \sum_{K,J} Q_{\mu,lKJ}^{(n,M)}(F)|nl[K]_J, M\rangle \qquad (2.9)$$

The dimension of the matrix under consideration is expressed by μ. The coefficients $Q_{\mu,lKJ}^{(n,M)}$ represent the amount of mixing. When the atom in the external field is excited from ψ_{lower},the electric dipole transition intensity can be written as:

$$I_\mu(F) = P_L \sum_M |\langle \psi_{lower}, M|z|\psi_\mu^{(n,M)}(F)\rangle|^2 \qquad (2.10)$$

Here we assume that the lower level Zeeman states with different M are equally populated. P_L is proportional to the intensity of the laser and is independent of the values of F and μ.

2.3.2 Calculation results

The levels with large principal quantum number n and large l are very closely spaced. Hence, the Stark coupling of these energy levels has to be considered in the calculation. For instance, in the calculation for the Stark effect on krypton $11f$, the zero field matrix should not only include the energy levels of 11f, but also the other levels like $11g$, $11h$, ..., $11l_{n-1}$. However, for calculating xenon $13f$ levels, besides the energy levels with orbit quantum number $l \geq 3$, the zero field matrix needs including the other adjacent levels, such as $16,17,18s$ $16,17p$, $16,17d$. Figure 2.9 shows the calculation results of Stark maps, (a) is for krypton $11f$ (b) is for xenon $13f$. The Stark map of krypton $11f$ shows a splitting of
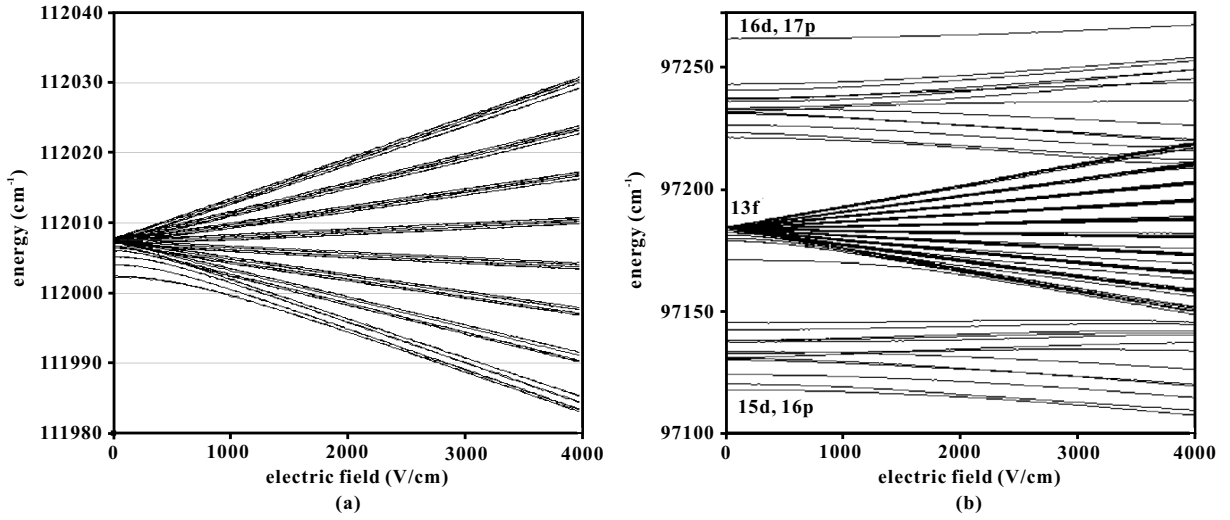
Figure 2.9: Stark map for $11f$ of a krypton atom (a) and $13f$ of a xenon atom (b).

the energy levels of $11f$ and of the degenerate levels $11g$, $11h$ and $11l_{n-1}$. The dependence of the $11f$ energy levels on the electric field is quadratic, in contrast to the linear response of the other levels such as $11g,11h,\ldots$ etc. This different behaviour can be attributed to the fact that levels with $l > 3$ have almost zero quantum defects (no electron orbit penetrates the core of the atom), but for $11f$ the quantum defect is 0.16. From the Stark maps in figure 2.9 (b) it is evident that the special complexity increases in high electric fields. Therefore we can conclude that for principal quantum number $n \geq 13$, some energies of s, p and d are closer to the energies of $f,\ldots, l_{n-1}$, so the coupling between these energy levels with the nf levels cannot be ignored. Hence, the Stark components become more complex.

Figure 2.10 shows the theoretical spectra for the various magnitudes of the electric field. The distance between the peaks increases with the electric field. The calculation shows that the energies of krypton and xenon atoms consist of several equidistant Stark components in high electric fields, and the number of these Stark components is $N = n - 3$ (see figure 2.11 and 2.15 (c) and (d)). Similar results in Argon are observed and explained by V. P. Gavrilenko et al [15].
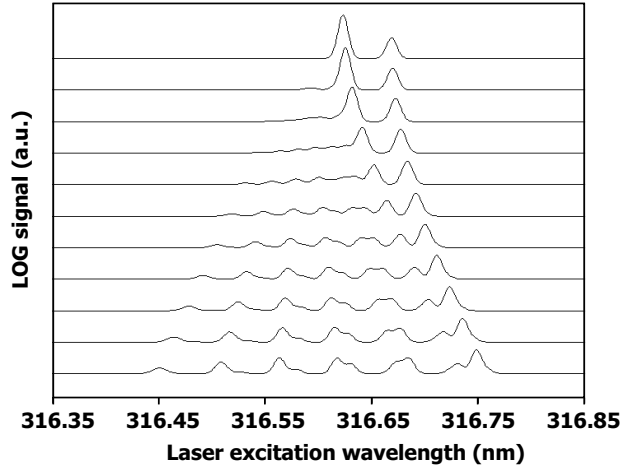
Figure 2.10: Krypton Stark spectrum excited from $5s$ to $9f$.

2.4 Comparison of experiments with theoretical calculation

In this section, the measurement data that were obtained by the method described in section 2.2 are compared with the theoretical results which were calculated by the method described in section 2.3.

2.4.1 Comparison for xenon

Figure 2.11 and 2.12 show the comparison of the results of the experiments with the theoretical calculations. The following features can be deduced:

1. There is a good agreement of peak positions for both large n and small n. Only for 10f, peak number 7, there is a discrepancy in peak position between experiment and calculations, which is probably caused by (minor) inaccuracies in the methods to derive the transition intensities from the calculations.

2. As expected, there are more peaks for larger n. The number of peaks in the experimental spectra is in a good agreement with the calculation data for large n and in poorer agreement for small n in high field.

3. The calculation is less successful at reproducing the (relative) intensity distribution for small n, but better agreement is obtained for larger n, This is probably due to the relatively simple calculation procedure used to calculate transition intensities
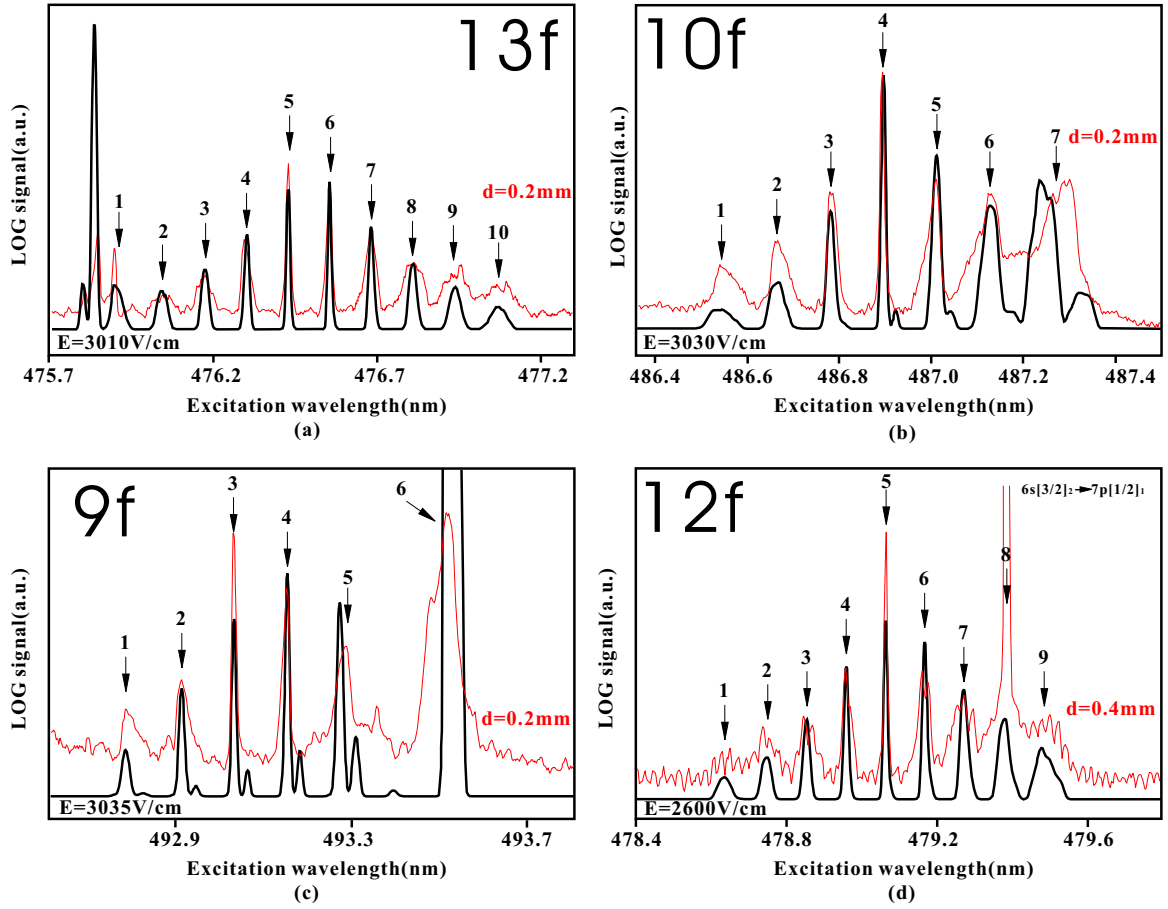
Figure 2.11: Experimental LOG spectra compared with calculated spectra for xenon 9, 10, 12 and $13f$ excitation from $6s'[1/2]_0$.

form Stark maps. Nevertheless, for the determination of the measured electric field strength using the calculation, only the peak position is needed and the calculation method can accurately describe these peak positions.

4. The Stark manifolds for large n are more sensitive to the electric field than the ones for smaller n.

5. The peripheral peaks in the experiments are wider than the central peaks. This can be explained by the gradient of the electric field within the cross-section of the laser beam.

6. The experimental spectrum for the $12f$ manifold shows an additional (strong) peak around 479.38nm, superimposed on the Stark mainfold. This peak corresponds the
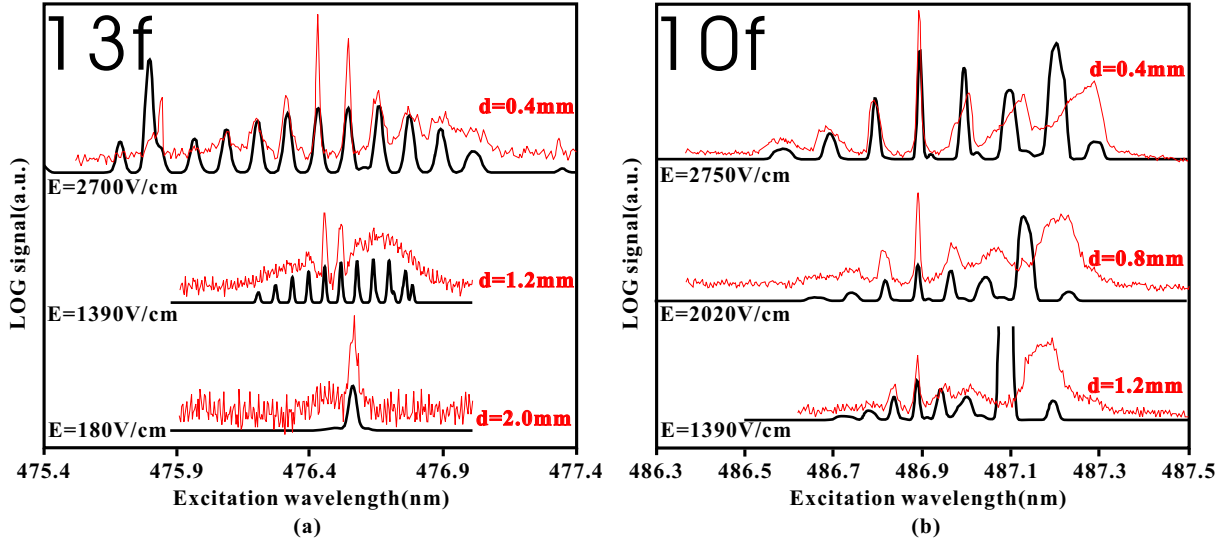
Figure 2.12: The comparison of experiment and calculation (a) for $13f$ and (b) for $10f$. The thin lines are the spectra of experiments, and the bold lines are the theoretical spectra.

transition $6s[3/2]_2$ to $7p[1/2]_1$. Since LOG spectroscopy detects all transitions in a discharge, additional peaks can be observed experimentally, but these transition are not included in the calculation.

Because the laser beam width (FWHM) is about 0.15mm and the sheath is only about 1∼2mm, the electric field in the cross section of the laser beam was inhomogeneous, so the influence of the gradient of the electric field across the laser beam has to be considered. We assume that the intensity distribution of the laser beam in a direction parallel to the electric field is Gaussian, and in the vertical direction is constant. With this simple model, the corrected theoretical spectra $I_c(E, \lambda)$ can be:

$$I_c(E, \lambda) \propto \int_{-0.075}^{0.075} I(E + \Delta E(x), \lambda) G(\frac{\sqrt{2 \ln 2} x}{0.075}) dx \tag{2.11}$$

Here, $I(E + \Delta E(x), \lambda) = I(0, \lambda)$ when $E + \Delta E \leq 0$, and $\Delta E(x) = kx/0.075$, where E is electric field strength, $G(x)$ is the Gaussian distribution, and $I(E, \lambda)$ is the spectrum without integrating over the electric field distribution of the laser beam. k is the coefficient of the linear fit of the electric field in the sheath. By integrating over the electric field distribution in laser beam, the corrected theoretical LOG spectra are obtained and they are presented in the figures 2.11, 2.12, 2.15.
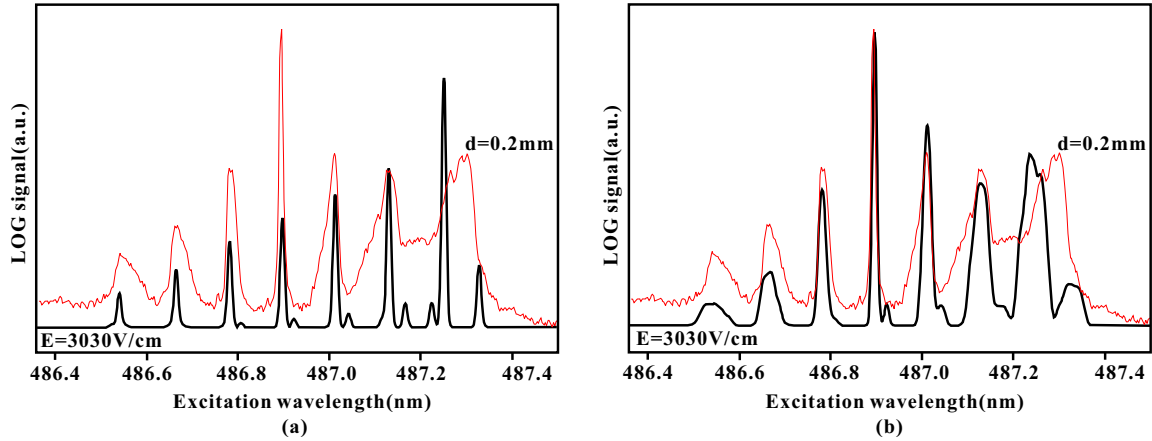
Figure 2.13: Comparison of the uncorrected and corrected calculation spectra with the experimental results obtained from a xenon discharge. (a) is the uncorrected calculation spectrum for (bold line) compare with the experimental data (thin line) for $10f$ and (b)is a corrected calculation spectrum (bold line) compare with experimental data.

Figure 2.13(a) is an uncorrected calculated spectrum compared with an experimental spectrum. The peak positions match well, but the relative intensities of the peaks do not agree and the calculated peaks are much narrower than the experimental ones, because only 15 pm width of laser wavelength was taken into account. Figure 2.13(b) shows a corrected calculation compared with an experimental spectrum. It is clear in this figure that a corrected calculation spectrum does reproduce the experimental data more reliably. There still is some difference in the intensities of the corrected LOG spectra and the experimental result, which may be because the laser beam cross-section are not being modeled adequately.

The electric field strength can be determined by directly matching the peaks position of both spectra in the experiment and in the calculation for larger field $(2000-4000V/cm)$. A very good accuracy, with errors less than $\pm 25V/cm$ for the excitation to $13f$ can be achieved for these fields. The error increases to $100V/cm$ at lower fields because the relative LOG signal is smaller and peaks become difficult to distinguish. The accuracy of the method becomes inadequate. When the field is below $500V/cm$ the peaks tend to single and its shift, compare to the zero field peak, is only few pm. The excitation laser wavelength should be carefully calibrated. One way is matching the experimental and calculated spectra in zero-field to calibrate the laser wavelength, if the zero-field energy is known. Then compare the experimental spectra to theoretical spectra in order to determine the field. The error can be a few hundred V/cm, which is more than 100% of the value to be measured. The
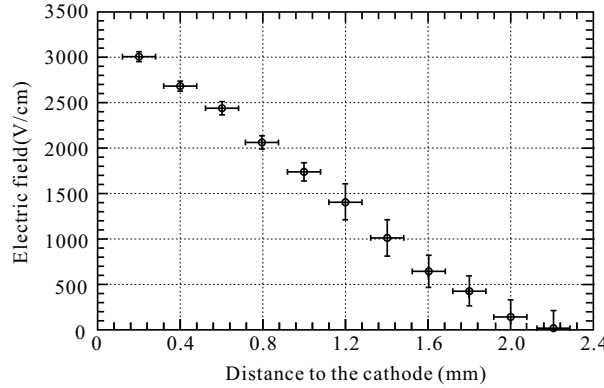
Figure 2.14: The spatial distribution of the electric field measured in the vicinity of the cathode in a xenon discharge using the result of $13f$.

accuracy of the method becomes insufficient.

Figure 2.14 shows the spatial distribution of the electric field measured in the vicinity of the cathode. We can see that the electric field in the sheath is almost linear, as we expect for this kind of discharge [32]. The thickness of sheath in our case was about 2.1 ± 0.2mm. By integrating the electric field over the sheath, we can obtain a potential drop over the sheath of $325V$. This is about 90% of the voltage of $345 \pm 10V$ that was applied across the discharge.

2.4.2   Comparison for krypton

In this section we will present the Stark effect data for krypton atoms.

Figures 2.15 show a comparison of the results of experiments and theoretical calculations. Similar features as described in Sec. 4.1 can be found in these figures: the peaks corresponding to large n are more sensitive to the electric field than the ones with smaller n, the agreement for high field and larger n is the best, and poorer agreement exists in lower fields, even for large n. In zero field conditions there are two fine-structure double transitions, from $5s[3/2]_2$ to $nf[3/2]_{1,2}$ and $nf[5/2]_{2,3}$, and the distance between these two peaks changes in the lower field $(0-800V/cm)$, This makes it easier to measure the electric fields at low value, because exact calibration of the peaks position is not necessary, as is the case for xenon.

The same method as used for xenon was applied to determine the electric field strength distribution in the sheath of a krypton glow discharge. Figure 2.16 shows the spatial distribution of the electric field measured in the vicinity of the cathode. By integrating the
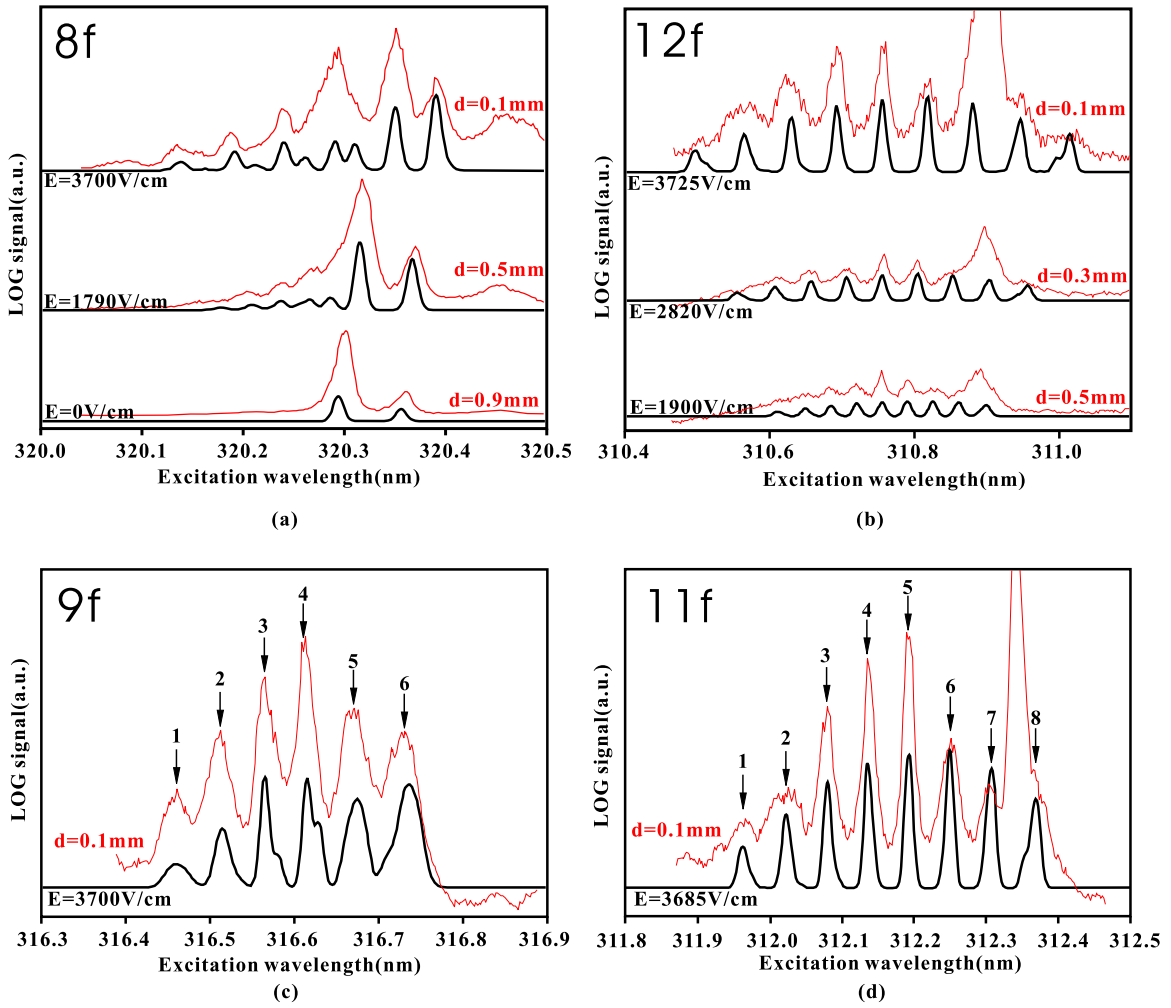
Figure 2.15: The comparison of experiment and calculation for krypton atoms. (a) is for $8f$, (b) is for $12f$, (c) is for $9f$, (d) is for $11f$.

electric field over the sheath, we obtain a potential drop over the sheath of the krypton discharge of $215V$. Similar to xenon, this is about 90% of the voltage of $240 \pm 10V$ that was applied across the discharge gap.

A remarkable shift of the energy levels of higher p states of krypton in the electric field was observed (see figure 2.17). The relatively larger LOG signal in the case of p state excitation is interesting from a diagnostics point of view. The detail will be discussed in next chapter.
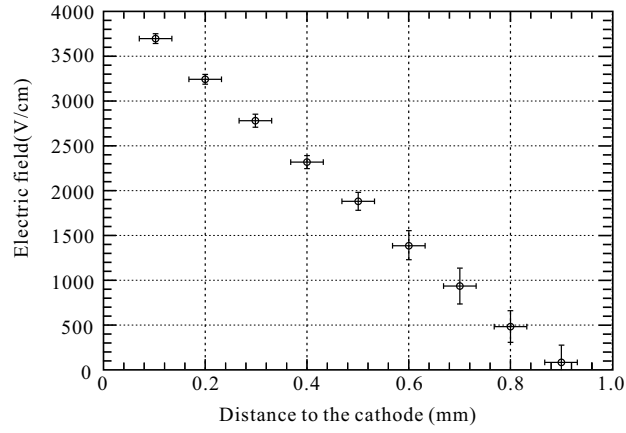
Figure 2.16: The electric field spatial distribution measured in the vicinity of the cathode for krypton.
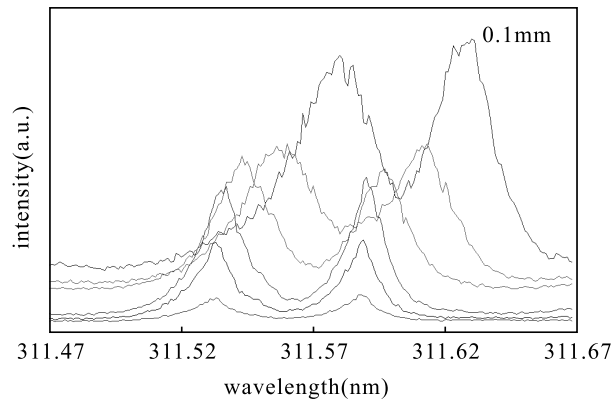
Figure 2.17: A set of LOG spectra for Kr 14p obtained at different distances to the cathode. The marked top spectrum is obtained at 0.1mm. The others spectra are obtained at distances separated by 0.2mm.

2.5 Conclusion

A spectroscopic method for the measurement of the electric field in a glow discharge in xenon and krypton was demonstrated. The results shown here demonstrate that it is possible to measure Stark effects in the sheath of xenon and krypton glow discharges. Measurement of the electric field in sheaths can be performed using the method of comparing the Stark effect measurement with theoretical calculations. The sensitivity of the magnitude of the electric field in both case demonstrates that an even better accuracy could be obtained for high fields or large principal quantum numbers n.

In addition to these f state excitations, we also observed Stark effects of p states. Details for the Stark effect of p states of noble gas will be discussed in the next chapter.

References

[1] J. P. Booth, J. Derouard, M. Fadlallah, and N. Sadeghi. Time-resolved electric-field measurements in 30 kHz hydrogen discharges by optical emission Stark spectroscopy. *J. Appl. Phys.*, 74:862–867, 1993.

[2] M. L. Zimmerman, M. G. Littman, M. M. Kash, and D. Kleppner. Stark structure of the Rd states of alkali-metal atoms. *Phys. Rev. A*, 20:2251–2275, 1979.

[3] K.A.H. van Leeuwen and W. Hogervorst. Stark effect in 6s5d and 5d6p states in barium measured with laser-atomic beam spectroscopy. *Z. Phys. A - Atoms and Nuclei*, 310:37–42, 1983.

[4] K.A.H. van Leeuwen and W. Hogervorst. High-resolution studies of the Stark effect in even-parity Rydberg states of CaI. *J. Phys. B: At. Mol. Phy*, 16:3873–3893, 1983.

[5] K.A.H. van Leeuwen, W. Hogervorst, and B.H. Post. Stark effect in barium 6snd $^1D_2$ ryderg states; evidence of strong perturbations in the $^1F_3$ series. *Phys. Rev. A*, 28(4):1901–1907, 1983.

[6] K.A.H. van Leeuwen and W. Hogervorst. Stark effect, Hyperfine structure and isotope shifts in highly excited states of BaI and CaI. *Z. Phys. A - Atoms and Nuclei*, 316:149–156, 1984.

[7] D. E. Kelleher and E. B. Saloman. Rydberg states with anisotropic ion cores: Stark effect. *Phys. Rev. A*, 35:3327–3338, 1987.

[8] C. Delsart and J.C. Keller. Investigation of the Stark effect in krypton autoionizing Rydberg series with the use of two-step laser excitation. *Phys. Rev. A*, 28:845–849, 1983.

[9] P. F. Brevet, M. Pellarin, and J. L. Vialle. Stark effect in argon Rydberg states. *Phys. Rev. A*, 42:1460–1466, 1990.

[10] W. E. Ernst, T. P. Softley, and R. N. Zare. Stark-effect studies in xenon autoionizing rydberg states using a tunable extreme-ultraviolet laser source. *Phys. Rev. A*, 37:4172–4183, 1988.

[11] R. D. Knight and Liang-guo Wang. Stark structure in Rydberg states of xenon. *Phys. Rev. A*, 32:896–900, 1985.

[12] C.A. Moore, G. P. Davis, and R. A. Gottscho. Sensitive, nonintrusive, In-Situ measurement of temporally and spatially resolved plasma electric fields. *Phys. Rev. Lett.*, 52:538–541, 1984.

[13] E. A. Den Hartog, D. A. Doughty, and J. E. Lawler. Laser optogalvanic and fluorescence studies of the cathode region of a glow discharge. *Phys. Rev. A*, 38:2471–2491, 1988.

[14] B. N. Ganguly. Measurement of high Rydberg ^1P spectra of atomic helium and its application to glow-discharge diagnostics. *J. Appl. Phys.*, 60:571–576, 1986.

[15] V. P. Gavrilenko, T. Kim, H. J.and Ikutake, J. B. Kim, Y. W. Choi, M. D. Bowden, and K. Muraoka. Measurement method for electric fields based on Stark spectroscopy of argon atoms. *Phys. Rev. E*, 62:7201–7208, 2000.

[16] M. D. Bowden, Y. W. Choi, K. Muraoka, and M. Maeda. Measurements of sheath electric fields in a high pressure helium radio frequency discharge. *Appl. Phys. Lett.*, 66:1059–1061, 1995.

[17] K. Takiyama, T. Katsuta, M. Watanabe, S. Li, T. Oda, T. Ogawa, and K. Mizuno. Spectroscopic method to directly measure electric field distribution in tokamak plasma edge. *Rev. Sci. Instrum.*, 68:1028–1031, 1997.

[18] J. B. Kim, K. Kawamura, Y. W. Choi, M. D. Bowden, and K. Muraoka. Studies of the sheath structure in an RF discharge using experimental, analytical and simulation approaches. *IEEE Trans. Plasma Sci.*, 27:1510, 1999.

[19] Y. W. Choi, M. D. Bowden, and K. Muraoka. Electric field measurements in an argon glow discharge using laser spectroscopy. *Appl. Phys. Lett.*, 69:1361–1363, 1996.

[20] U. Czarnetzki, D. Luggenhölscher, and H. F. Döblele. Sensitive electric field measurement by fluorescence-dip spectroscopy of Rydberg states of atomic hydrogen. *Phys. Rev. Lett*, 81:4592–4595, 1998.

[21] M. L. Keeler, H. Flores-Rueda, J. D. Wright, and T. J. Morgan. Scaled-energy spectroscopy of argon atoms in an electric field. *J. Phys. B: At. Mol. Opt. Phys.*, 37(4):809–815, 2004.

[22] U. Czarnetzki, D. Luggenhölscher, and H. F. Döblele. Space and time resolved electric field measurements in helium and hydrogen RF-discharges. *Plasma Sources Sci. Technol.*, 8(2):230–248, 1999.

[23] J. P. Booth, M. Fadlallah, J. Derouard, and N. Sadeghi. Electric field measurements in discharges by 2+1 photon laser Stark spectroscopy of atomic hydrogen. *Appl. Phys. Lett*, 65:819–821, 1994.

[24] Nist atomic spectra database.

[25] M. Bounakhla, J. P. Lemoigne, J. P. Grandin, X. Husson, H. Kucal, and M. Aymar. Laser spectroscopy of even parity Rydberg series of krypton. *J. Phys. B: At. Mol. Opt. Phys.*, 26:345–361, 1993.

[26] I. I. Sobelman. Atomic spectra and radiative transitions. *Springer-Verlag, Heidelberg*, 1979.

[27] G. Racah. On a new type of vector coupling in complex spectra. *Phys. Rev.*, 61:537, 1942.

[28] B. W. Shore and D. H. Menzel. Principles of atomic spectra. *John Wiley and sons, Inc.,*, 1968.

[29] E. E. Salpeter and H. A. Bethe. Quantum mechanics of one-and two-electron atoms. *Springer*, 1979.

[30] M. Rotenberg, R. Bivens, N. Metropolis, and J. K. Wooten. The 3j and 6j symbols. *Cambridge, MA: MIT Press*, 1959.

[31] A. R. Edmonds, R. Pullen, J. Picart, and N. Tran Minh. Tables for the computation of radial integrals in the Coulomb approximation. *J. Phys. B: At. Mol. Opt. Phys.*, 12(17):2781–2787, 1979.

[32] Y. P. Raizer. Gas discharge physics. *Berlin, Springer*, 1997.

Chapter 3

Diagnostics of the Stark effect of p levels of noble gas atoms

Abstract

We have studied the Stark effect for Rydberg p states of noble gas atoms using laser optogalvanic spectroscopy. The measurements were performed in the sheath region of these noble gas discharge. Laser excitation from a metastable state to the np states was monitored by optogalvanic spectroscopy. Clear Stark shifts were observed and the experimental results were compared with the theoretical calculation based on solving the Schrödinger equation of these noble gas atoms in an electric field. There is a good agreement between the calculations and the experimental results. The analysis shows that the Stark shift of np states of noble gas atoms can be used for electric field measurement for its higher transition probability compare to the nf states.

Chapter 3

3.1 Introduction

The Stark effect is the splitting or shift of atomic or molecular spectral lines as a result of an applied electric field. It can be exploited as an electric field measurement by moniting the energy levels of atoms or molecules, especially in plasmas, where normal tools such as Langmuir probes may have the complication of perturbation of the discharge. Stark spectroscopy is a promising candidate to determine the electric field in a plasma.

Zimmerman et al published the first investigation on the Stark effect of Rydberg levels in alkali atoms by using laser spectroscopy [1, 2]. A simple model, a Rydberg electron interacting with the ionic core in the external electric field, was applied for their calculation. K.A.H. van Leeuwen et al investigated the Stark effect in barium atoms, BaI and CaI [3–6]. Kelleher and Saloman [7] also test barium atom with the Zimmerman's method later, and subsequent experiments and calculations developed this method to the noble gas atoms, such as Brevet et al [8], who tested the Stark effect in argon Rydberg states, Delsart and Keller [9], who investigated the Stark effect in krypton, Knight and Wang [10], who studied the Stark structure of the bound Rydberg states of xenon, and Ernst et al [11], who also tested in xenon. The calculations successfully explained the behavior of noble gas atom energy levels, such as the orbit quantum number $l = 3, 4, ..., l - 1$ etc. in external electric fields, and the hydrogenic approximation used was valid. However, for p states of noble gas atoms, this assumption may not be valid, because of the smaller orbital momentum which may induce the orbit of the Rydberg electron to penetrate the ionic core.

The aims of the research described in this chapter are to measure the Stark effect in the p energy levels of krypton, argon and xenon in the sheath of these gas discharges. The excitation was from metastable states to p Rydberg states. The measurement was performed by using laser optogalvanic spectroscopy. The electric field in the sheath was calibrated using excitation to nf levels [12]. Secondly the results of LOG measurements were compared to the results of the calculations, and finally the feasibility for electric field measurement by using p states was examined.

The structure of this chapter is as follows. Section 2 contains a description of the experimental system and results. In section 3, we summarise the method of the calculations and give a short discussion on the calculated results. In section 4, we compare the results of LOG measurements with the calculations. In section 5, the suitability of the Stark effect of p states for the electric field measurement is discussed, and a brief conclusion is given in Section 6.
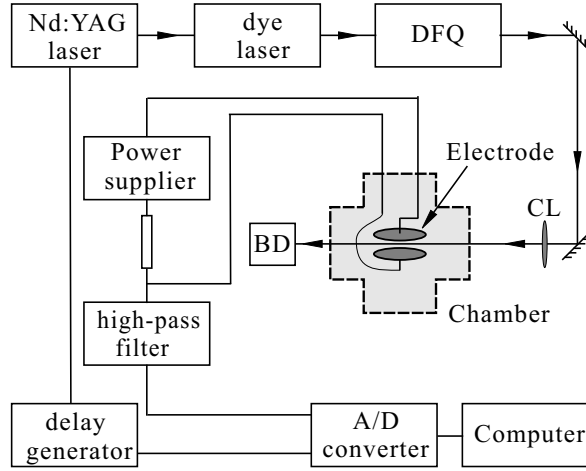
Figure 3.1: Experimental apparatus for LOG measurements in a dc glow discharge, BD is laser beam dump, DFQ is the frequency-doubled crystal and CL is cylinder lens.

3.2 Experiment

3.2.1 Experimental set-up

The experimental arrangement has been described in the previous chapter and will only be summarized here. The experimental setup is shown in figure 3.1. A glow discharge is created by applying a DC voltage to two parallel plate electrodes. The pressure in the chamber was 700 Pa of krypton, argon or xenon. The excited laser beam was sent through the sheath of the plasma. The excitation to the Rydberg states was then detected by opto-galvanic spectroscopy. In this technique, the discharge current change was monitored with a high pass filter connected to a data acquisition system. A delay generator synchronized the data acquisition system and the dye laser. By scanning the dye laser wavelength and measuring the LOG signal, the absorption spectrum can be obtained.

The dye laser was pumped by a Nd:YAG laser (Continuum) with second harmonic output (532 nm) and by using different dyes and frequency-doubled crystal. The laser can be operated at 306-330 nm for krypton measurements, at 295-305 nm for argon measurements and at about 490 nm for xenon (without using the frequency doubling crystal). The laser dye, Coumarin 102, was used for xenon excitation, Rhodamine 101 was for krypton and Rhodamine B was for argon.
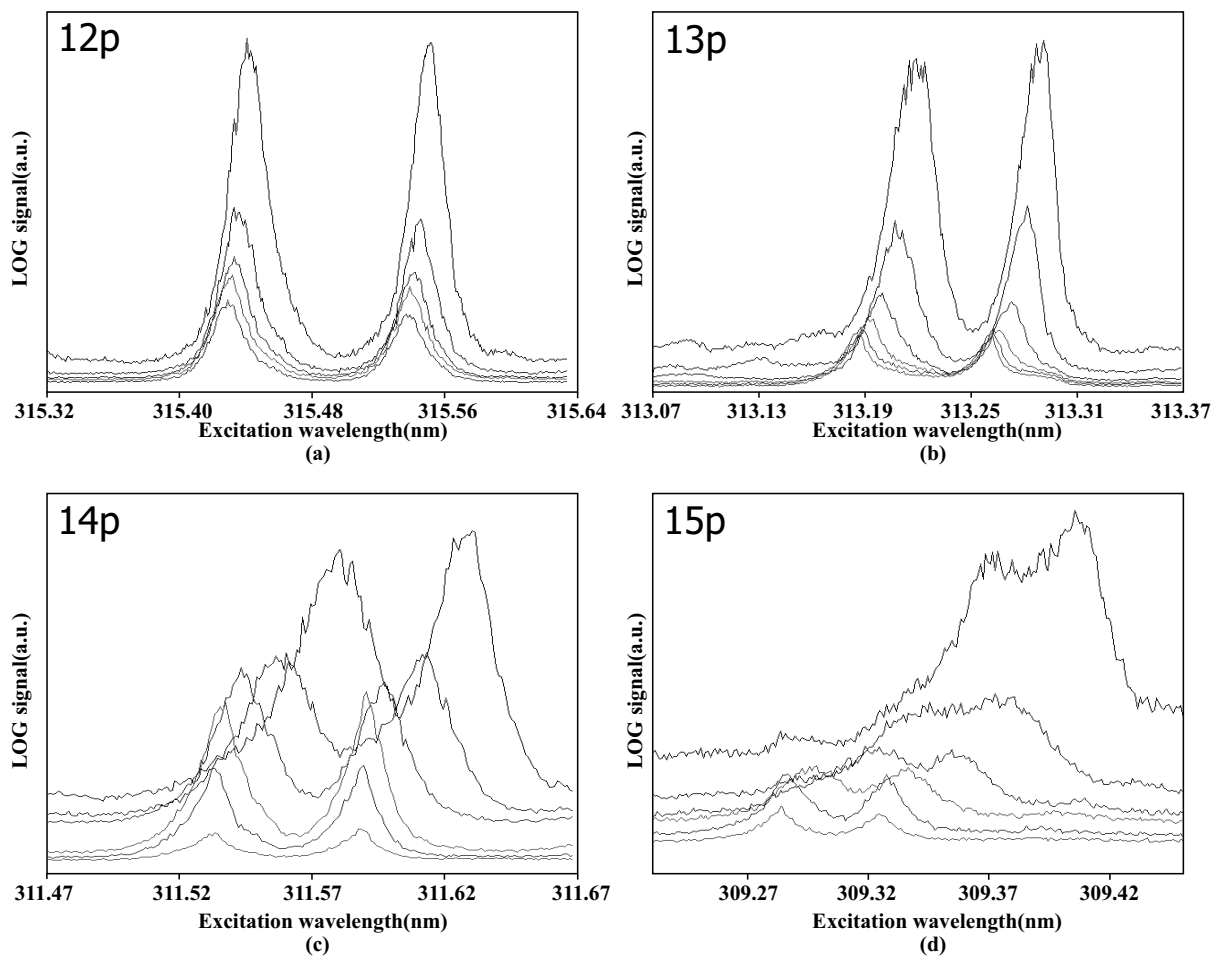
Figure 3.2: Four sets of experimental LOG spectra obtained at different distances to the cathode in a krypton discharge at 700 Par, The figure contains: (a) Spectra exciting from $5s[3/2]_2$ to $12p$, (b) to $13p$, (c) to $14p$ and (d) to $15p$. The top spectra in each figure was obtained at a distance of 0.1mm to the cathode, and following further away with steps of 0.2mm away from cathode.
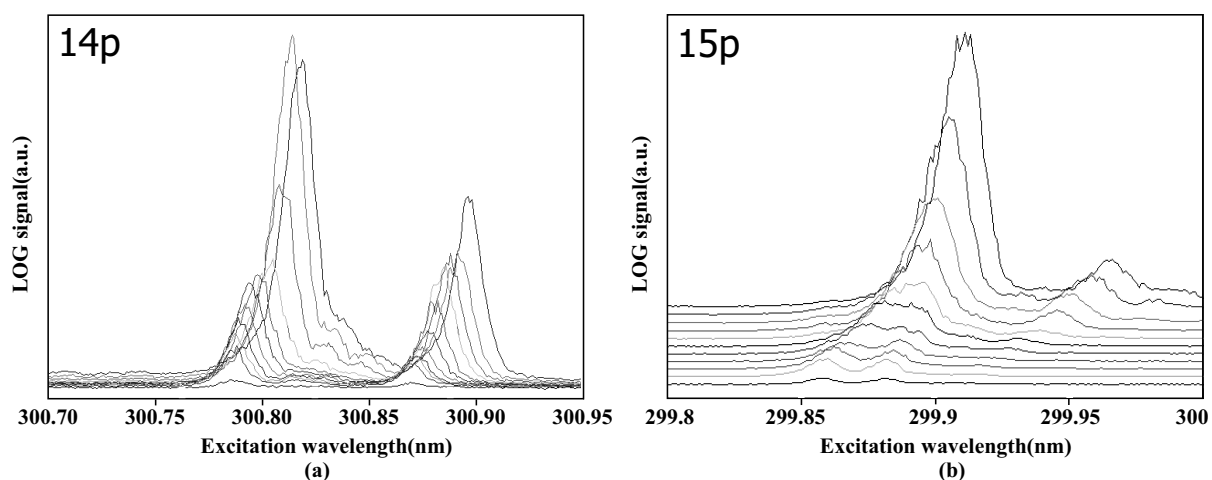
Figure 3.3: Experimental LOG spectra obtained at different distances to the cathode in a argon discharge at 700 Par. (a) a set of spectra excitation from $4s[3/2]_2$ to $14p$, (b) to $15p$. The top spectra in each figure was obtained at a distance of 0.1mm for (a) and 0.2mm for (b) to the electrode. The following were measured further away with steps of 0.1mm, but the steps for last two in (a) and (b) are 0.2mm.
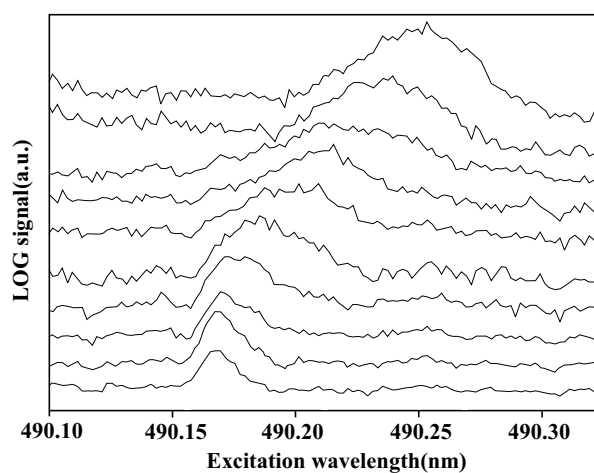
Figure 3.4: Experimental LOG spectra obtained at different distances to the cathode in a xenon discharge at 700 Par, excitation from $6s'[1/2]_0$ to $13p$(the y-scale of LOG signal for each spectrum is adjusted to increase clarity). The top spectra has been obtained at the distance of 0.1 mm to the cathode, the following further away with steps of 0.1mm.

3.2.2 Experimental Results

Figure 3.2-3.4 show LOG spectra measured in krypton, argon and xenon discharges, respectively. It is clear that the energy levels of higher p states of noble gases move to longer wavelengths in an electric field. Several features of these spectra are listed below:

1. The results show the LOG signal increases rapidly with the laser beam approaching the cathode. The reason is that when the laser beam is closer to the cathode, the electrons caused by the laser excitation can obtain more energy from electric field. These electrons can create more ionizations, and subsequently the optogalvanic signal is larger.

2. For the same laser beam position, the shift of the p levels with smaller principle quantum number is smaller than the shift for larger principle quantum numbers. In other words: as expected, the energy levels with larger principle quantum number are more sensitive to the electric field. This is the same for the nf levels.

3. For both krypton and argon discharges, in the LOG spectra for excitation to $n = 15$, the two peaks mix into one where the electric field increases(see figure 3.3 (b)).

4. In our measurement for the p states in a xenon discharge, the initial state is $5s'[1/2]_0$. Only one peak relating to the transition from $6s'[1/2]_1$ to $np[1/2]_1$ was found in the LOG spectra (figure 3.4). The transition to $np[3/2]_1$ should be allowed, but is nevertheless not observed.

5. Unlike the nf Stark manifold [12, 13], which has many components for high fields, only two peaks were found in the LOG spectra of np states of krypton. The data shows that the two peaks related to the transition from $5s[3/2]_2$ to $np[3/2]_{1,2}$ and $[5/2]_{2,3}$. Similar phenomena were found in the measurement for 15 p in an argon discharge. However, the intensity of the transition from $4s[3/2]_2$ to $14p[5/2]_{2,3}$ is very weak, and we can only distinguish it in some of the spectra. It seems that the right hand set of peaks shown in figure 3.3(a) are related to the transition from $4s[3/2]_2$ to $14p[1/2]_1$. These points will be discussed further in Sections 4.

6. The transition intensities from $5s$ for krypton and $4s$ for argon to np is much higher than to nf in krypton and argon discharges. For xenon, the transitions from $6s'$ to np and nf are almost equal. The difference maybe in the initial state which for krypton and argon is s, but for xenon it is s'.

In order to relate the observed the Stark shifts to electric field strengths, the electric field distributions in the sheath of noble gas discharges were measured by using an alternative
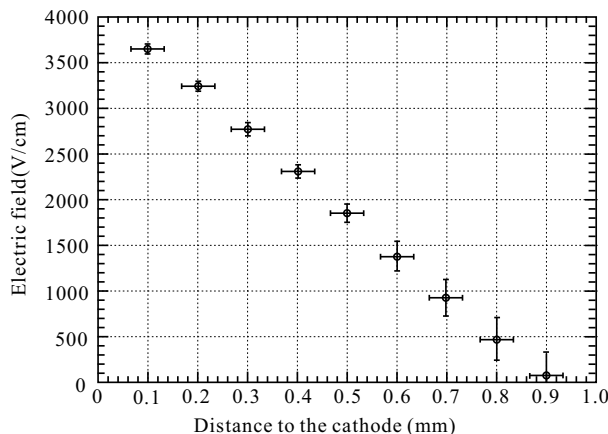
Figure 3.5: Electric field spatial distribution measured in the vicinity of the cathode in krypton discharge using results of $12f$.

method based on the Stark effect of nf levels (see the chapter 2). Figure 3.13 shows the result of the electric field calibration in the sheath of a krypton discharge. Similar measurements were made for argon and xenon discharges.

In the next section, we present a summary of the theoretical calculation methods for the Stark effect of np states, and in section 4 we compare the calculations to our experimental results.

3.3 Theoretical Calculation

3.3.1 Calculation method

In the section 2.3.1, a theoretical calculation method is described for the Stark effect of nf states of xenon and krypton atoms. The results of this method, which is based on the assumption of hydrogen-like atoms, are good predictions for the behavior of the nf energy levels of xenon and krypton in an electric field, specially in high fields. There is a good agreement between the experimental data and the calculation results. However, for p states of xenon, krypton and argon atoms, the assumption of hydrogenic atoms is problematic, because the orbit of the Rydberg electron, which have the smaller orbit quantum number, penetrate the ionic core. Even so, we still try to use this simple model to calculate the Stark effect of the p states. We summarized a few main issues below.

1. In our calculations, the jK coupling scheme is still applied for the np Rydberg states of noble gas atoms [14, 15], as we did in the calculation for nf energy levels.
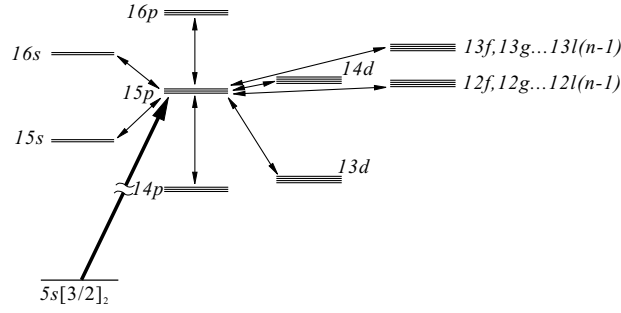
Figure 3.6: The excitation scheme for from 5s to 15p krypton, The bold arrow is the laser excitation and the fine arrows correspond to the neighboring Rydberg states interacting with 15p.

2. The unperturbed Hamiltonian H_0 is an diagonal matrix and its elements are the zero field energy levels. However, now more zero-field energy levels are included in the undisturbed Hamiltonian matrix. As figure 3.6 shows, the undisturbed Hamiltonian should not only include the zero-field energy levels of 15p, but also the zero-field energy levels of $12f$ to $12l_{11}$, $13d$, $13f$ to $13l_{12}$, 14p,d etc. That means a larger matrix is used for the calculations. Some of these energy level data can be found in references [16,17], but most of them have to be calculated with the method described in Chapter 2(also see Brevet et al [8]).

3. Highly excited noble gas atoms interact with electric fields like a dipole in the applied electric field. Therefore, the Stark Hamiltonian can be written as $H_{Stark} = -eEz$. E is the electric field strength, its direction is same to the z axis, z is the distance of the outer orbit electron to the ionic core and e is the electric charge. The axis of dipole is chosen to be parallel to the direction of the electric field.

4. Solving the Schrödinger equation is performed by diagonalizing the total Hamiltonian $H = H_0 + H_{Stark}$ for different electric fields. A Coulomb approximation is adopted for the radial integral in the diagonalisation procedure.

5. The energy levels in an electric field are the eigenvalues of the Hamiltonian H, and the corresponding intensity can be calculated using the eigenfunctions of H.

6. Because the sheath of our plasma is only about 1mm wide, and the width of the laser beam is near 0.15mm, the electric field across the laser beam was inhomogeneous. Therefore, we will measure a superposition of spectra in different electric fields. When we assume the intensity distribution of the laser beam to be Gaussian, we can correct
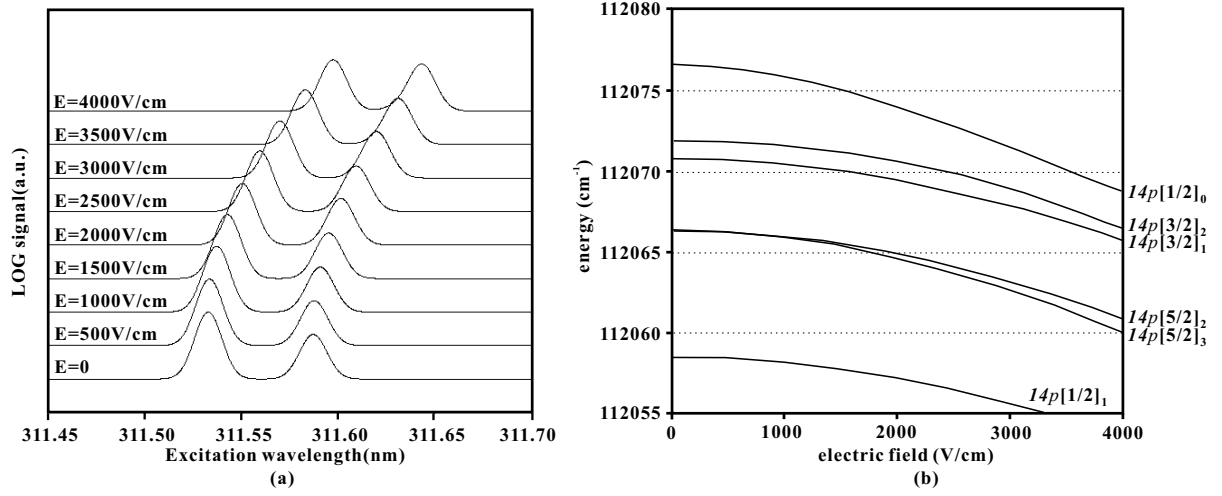
Figure 3.7: The calculated spectra excitation to $14p$ for krypton atom. (a) gives the calculation excitation spectra for different electric fields. (b) is a the Stark map indicating the energies of different levels as function of the electric field.

the calculation spectra by integrating over the electric field distribution in the laser beam. The correction was included in the following calculation for krypton and argon.

3.3.2 Calculation results

Figure 3.7 shows the calculation results of the theoretical spectra for various magnitudes of the electric fields and the Stark map of the $14p$ energy levels of the krypton atom. In figure 3.7(a), we can see two peaks shifting the to direction of longer wavelength with increasing the electric field strength. The Stark map (figure 3.7(b)) show that these two peaks correspond to the transition from $5s[3/2]_2$ to $np[3/2]_{1,2}$ and $[5/2]_{2,3}$. The behavior of p states is completely different with the linear manifold which was calculated for Rydberg levels with orbit quantum number $l \geq 3$ [12]. It seems that the transitions from $5s[3/2]_2$ to $np[3/2]_{1,2}$ and $np[5/2]_{2,3}$ are dominant, even in high fields. Unlike the $l \geq 3$ Stark manifold, the transitions forbidden by selection rules can be found in high electric fields. However, our calculations do not predict an observable transition from $5s[3/2]_2$ to $14p[1/2]_1$ nor for high, nor for low electric field, even if this transition is allowed by selection rules. As expected, the calculation results for argon atom are similar to krypton.
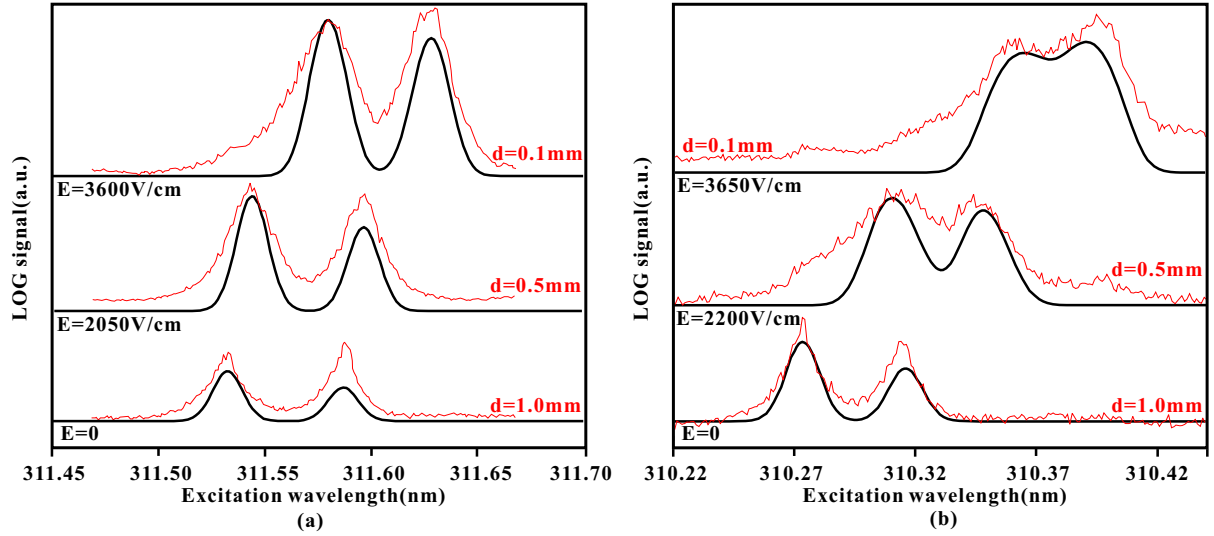
Figure 3.8: The comparison of experimental spectra obtained in a krypton discharge to calculated spectra. (a) and (b) are excited to $14p$ and $15p$, respectively. The thin lines are the experimental spectra and the bold lines are the calculated spectra. d is the distance of the laser beam to the cathode.

3.4 Comparison of experimental data with theoretical calculations

We can compare the experimental results obtained in the sheath of a noble gas discharge with the calculated results based on the method introduced in previous section.

3.4.1 Krypton

The comparisons are done by using a set of theoretical spectra for different electric fields to match an experimental spectrum obtained in the discharge. Figures 3.8 and 3.9 show the comparison of experimental results obtained in the sheath of krypton discharge. In figure 3.8, (a) and (b) are two sets of compared spectra for laser excitation to $14p$ and $15p$ respectively. The thin lines are the experimental spectra and the bold lines are the calculated spectra. d is distance of the laser beam to the cathode. There is a good agreement in the peak positions of experimental results and theoretical calculations, both for low and high fields. Especially the mixing of two $15p$ peaks in high fields is reproduced nicely by the calculation.

In figure 3.9, the lines are the calculation result for $14p$, and the triangular markers are the peak positions of the experimental spectra obtained at different positions in the
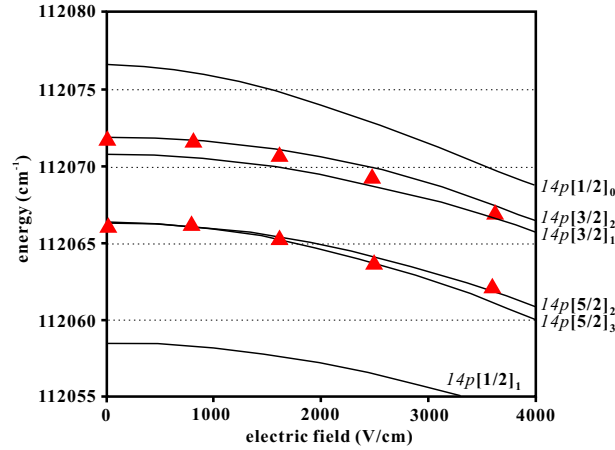
Figure 3.9: The comparison of experimental peak positions for LOG spectra in a krypton discharge. Triangular markers are measurement results and the lines are the theoretical calculations.

sheath of a krypton discharge. The electric field in these positions, as mentioned in the previous section, were calibrated by using the $12f$ linear-like manifold. The experimental data show that the two peaks, which are related the transitions from $5s[3/2]_2$ to $14p[3/2]_{1,2}$ and $14p[5/2]_{2,3}$. This agrees with the calculation results. Unlike the nf energy levels, there is no splitting in high fields. Compared with the shift of peak positions of these two energy levels, the distance of the two peaks changes little with the electric field.

The experimental spectra shows that no clear transition from $5s[3/2]_2$ to $14p[1/2]_1$ was found in a krypton discharge for whichever field value, despite the fact that the selection rules allow it.

In low field ($0 \Rightarrow 1000V/cm$), the shifts of the p levels were only few pm. However, the Stark shifts of energy levels apparently increases in high fields. The shift can be about 20pm (for $14p$) when the electric field changes from $3000 \Rightarrow 3700V/cm$.

3.4.2 Argon

Figure 3.10 shows the comparison of the experimental spectra to the calculated spectra. (a) is the comparison for $14p$, and (b) for 15p. For $14p$, we can see from this figure that there is a good match for the set of peaks which relate to the transition from $4s[3/2]_2$ to $14p[3/2]_{2,3}$ for experimental and calculated spectra in a argon discharge as well. However, the intensities of the transition from $4s[3/2]_2$ to $14p[5/2]_{2,3}$ are very weak. We can only see it in the spectra at a few positions. There is another set of clear peaks in experimental spectra. It seems this is set related to the transition from $4s[3/2]_2$ to $14p[1/2]_1$(see figure 3.11). However our calculation results for spectra do not predict it. For 15p, experimental data
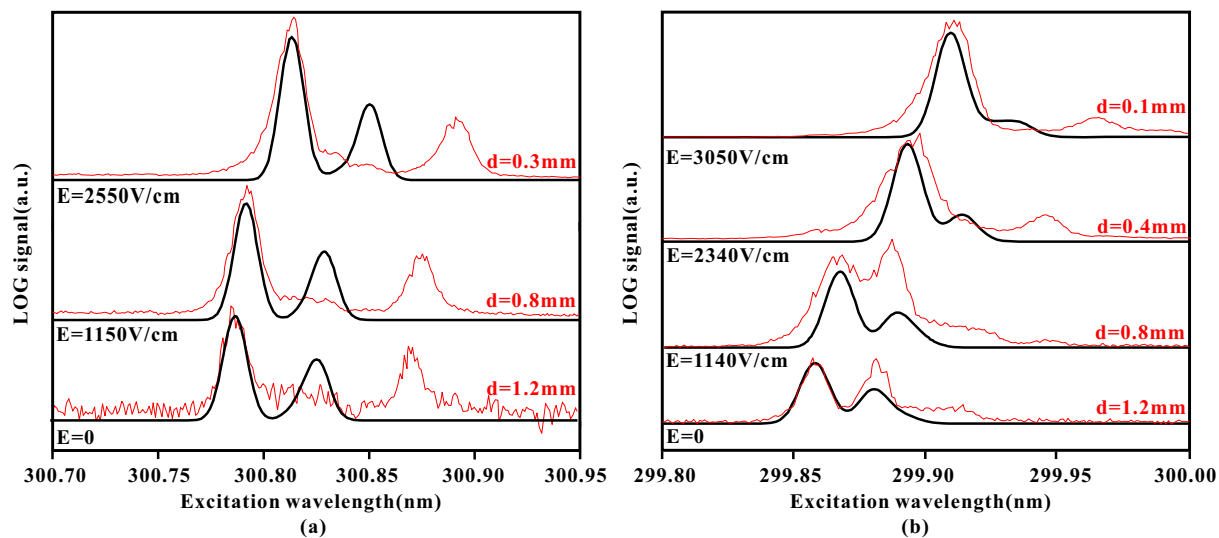
Figure 3.10: The comparison of experimental to calculated spectra for an argon discharge, (a) is excited to 14p and (b) is to 15p.
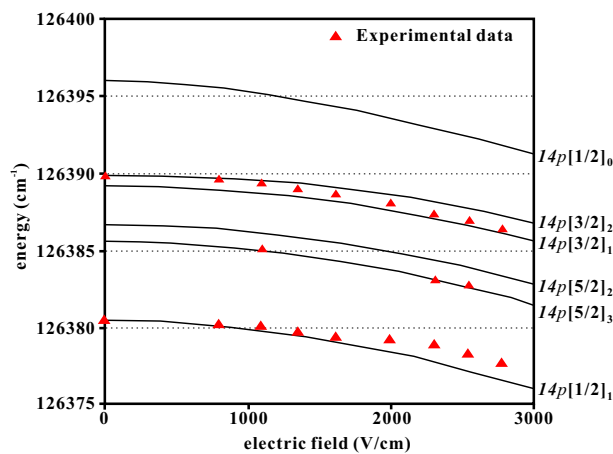
Figure 3.11: The comparison of experimental peak positions got from the LOG spectra in a argon discharge (triangular markers) with the theoretical calculation (lines) for the 14p of krypton atoms.
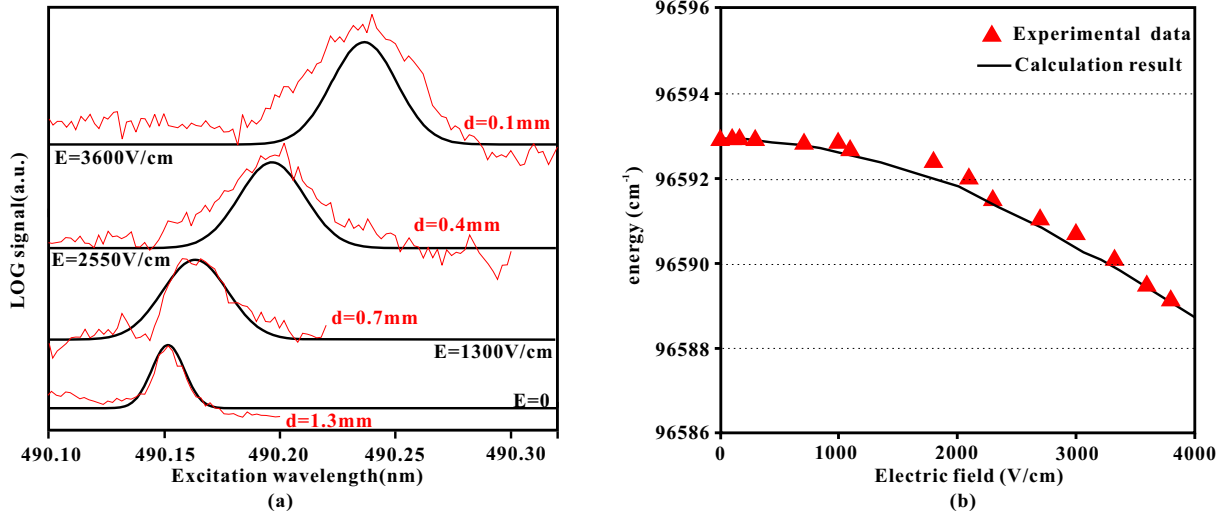
Figure 3.12: The comparison of experimental results obtained in a xenon discharge to calculation results. (a) The comparison of experimental spectra (fine lines) to calculated spectra (solid lines), excited to $13p$ and (b) Comparison of observed peaks positions (triangular markers) with the calculations. (solid line).

shows that the two transitions from $4s[3/2]_2$ to $15p[3/2]_{1,2}$ and $15p[5/2]_{2,3}$ gradually mix with increasing electric field strength. It appears that the intensities of the two transitions are roughly equal during the mixing procedure . However, the calculated spectra show the transition from $4s[3/2]_2$ to $15p[5/2]_{2,3}$ decreasing with the electric field rising. Therefore it is difficult to match the experimental spectra to the calculations.

3.4.3 Xenon

The experimental and calculated spectra are shown in figure 3.12 (a). Figure 3.12(b) gives the calculated result of the peak positions of $13p[1/2]_0$ (Black line) and the experimental data (triangular markers). Both figures show there is a good agreement. Unlike krypton and argon, in which the transition from s to p is much stronger than s to nf, the transition of xenon from $6s$' to $13p$ is similar to the transition from $6s$' to $13f$. The Stark shift of the $13p$ level of xenon atoms in high fields are relatively large. For example, the Stark shift of the $13p$ level of xenon atoms in high field (near 90pm) is almost three times of $14p$ of krypton atoms.
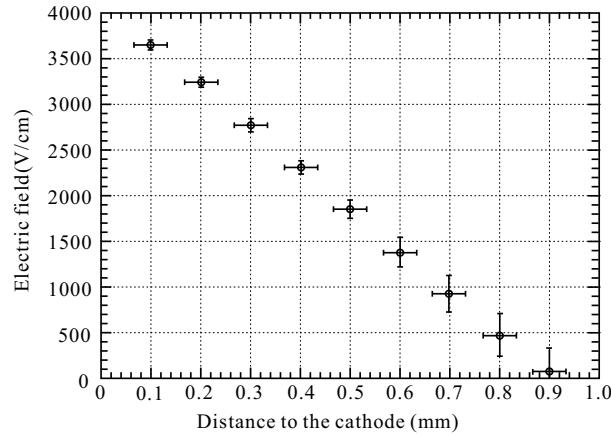
Figure 3.13: Spatial distribution of the electric field measured in the vicinity of the cathode in krypton discharge using $14p$ levels.

3.5 Feasibility of using p excitation for electric field measurement

As mentioned in last section, the transition from s to np is much stronger than to the nf, and the Stark shift for some of np levels is suitable for electric field measurement. Therefore the np states could be interesting alternatives to nf states for electric field measurements.

Figure 3.13 shows the spatial distribution of the electric field in the sheath measured in the vicinity of the cathode of krypton discharge using $14p$ levels. As expected, the electric field distribution is almost linear in the sheath [18]. The shift of the energy levels is larger in high field and the electric field strength could be determined within about 40V/cm. But in lower fields, the error is near 200V/cm, since the peak shift is small. By integrating the electric field over the sheath, we can get the potential drop over the sheath of krypton discharge: $213 \pm 30V$, which is near 90% of the voltage of 240V that was applied across the electrodes. This is in good agreement with the measurements using $12f$ described in chapter 2.

Figure 3.14 shows the shift of several krypton np energy levels as a function of the electric field strength. The shift of the $12p$ in an electric field is too small to allow for determination of the electric field with a reasonable resolution. The shifts of 14 and $15p$ are suitable for diagnosing electric fields in plasmas, for these energy levels have larger shifts in the electric fields and a higher intensity of the p states transition produce a larger LOG signal. For p levels with even higher principle quantum numbers, the expected shifts are larger, but the signal to noise ratio will become worse and, additionally, in plasmas, mixing of these energy levels with other states, such as $d, f, g, \ldots, l = n - 1$ states, make
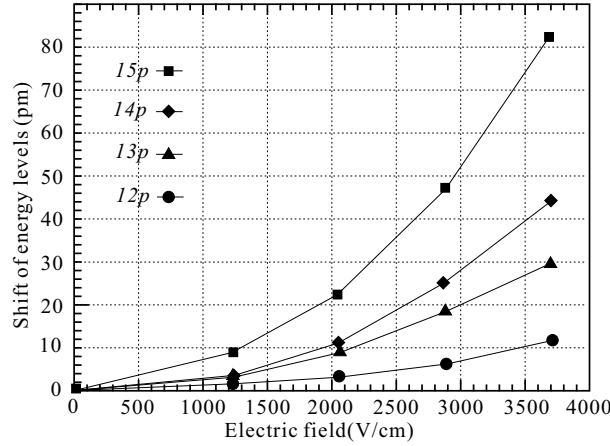
Figure 3.14: Shift of np energy levels of krypton atom depending on the electric field.

the LOG spectra too complex to identify the position of each level .

Figure 3.15 shows the spatial distribution of the electric field in the sheath measured by excitation to $13p$ and $13f$ from the $6s$' level. The overall agreement is within the experimental error for all measurements. However, in the range of $500 - 1500 V/cm$ the $13f$ excitation does not provide good measurement resolution because of the "merging"of the Stark components. The levels of $13p$ still show a clear peak which is easy to distinguish. Therefore, using $13p$ to measure the electric field gives a better resolution than using $13f$ in this range.

The nf levels are split into many components in high fields. They can easily be compared to the calculation spectra directly. Also the p states only show one or two peaks in the LOG spectra in high and low electric field. Therefore the laser wavelength must be carefully calibrated before to using it to compare the calculation results. From this point of view, using nf to measure higher electric field is better than using np.

By integrating the electric field distribution in the sheath (shown in figure 3.15), the voltage drop can be calculated, the magnitude is $215V \pm 15V$ about 81% of the voltage of $265 \pm 5V$ applied on the electrodes.

3.6 Conclusion

We have investigated the Stark effect in the p states of krypton, argon and xenon atoms using laser spectroscopy in the sheath of the discharge. There is a good agreement between the experimental results and the calculations. The results of the comparison of experimental and calculated spectra shows that a simple method of calculation can be used to predict
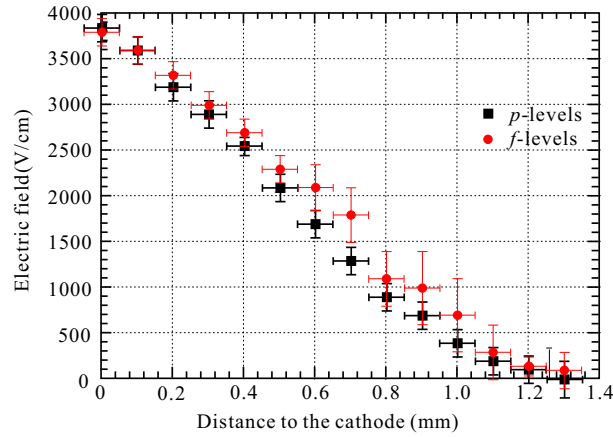
Figure 3.15: Electric field spatial distribution measured in the vicinity of the cathode (black for $13p$ and grey for $13f$).

the behavior of p levels of noble gas atoms in electric fields, and we find the p levels can also be using for electric field measurement. The method to determine the electric field is based on measuring the Stark shift of atoms and the quantification is done by comparing the results of experimental LOG spectra with calculations by solving the Schrödinger equation for noble-gas atoms. The resolution of the measurements of the electric field with Stark shift on p levels is almost the same as the Stark splitting of f levels for argon and krypton. However, the Stark effect of higher transition excited from the metastable state to the p state is easier to measure than for f states. For xenon atoms excited from $6s'[1/2]_0$, the intensities of both LOG signals are almost the same. A higher resolution can be obtained by using 13 p level than by using $13f$ for 500-1500V/cm. A similar effect is also visible in nf spectra of krypton and argon [12, 13]. However, for using np states to measure the electric field, accurate calibration of the exciting wavelength is needed. In high fields the shift of np levels is less sensitive than the splitting of nf states.

References

[1] M. G. Littman, M. L. Zimmerman, T. W. Ducas, R. R. Freeman, and D. Kleppner. Structure of sodium Rydberg states in weak to strong electric fields. *Phys. Rev. Lett.*, 36:788Í C791, 1976.

[2] M. L. Zimmerman, M. G. Littman, M. M. Kash, and D. Kleppner. Stark structure of the Rd states of alkali-metal atoms. *Phys. Rev. A*, 20:2251–2275, 1979.

[3] K.A.H. van Leeuwen and W. Hogervorst. Stark effect in 6s5d and 5d6p states in barium measured with laser-atomic beam spectroscopy. *Z. Phys. A - Atoms and Nuclei*, 310:37–42, 1983.

[4] K.A.H. van Leeuwen and W. Hogervorst. High-resolution studies of the Stark effect in even-parity Rydberg states of CaI. *J. Phys. B: At. Mol. Phy*, 16:3873–3893, 1983.

[5] K.A.H. van Leeuwen, W. Hogervorst, and B.H. Post. Stark effect in barium 6snd $^1D_2$ ryderg states; evidence of strong perturbations in the $^1F_3$ series. *Phys. Rev. A*, 28(4):1901–1907, 1983.

[6] K.A.H. van Leeuwen and W. Hogervorst. Stark effect, Hyperfine structure and isotope shifts in highly excited states of BaI and CaI. *Z. Phys. A - Atoms and Nuclei*, 316:149–156, 1984.

[7] D. E. Kelleher and E. B. Saloman. Rydberg states with anisotropic ion cores: Stark effect. *Phys. Rev. A*, 35:3327ÍC3338, 1987.

[8] P. F. Brevet, M. Pellarin, and J. L. Vialle. Stark effect in argon Rydberg states. *Phys. Rev. A*, 42:1460–1466, 1990.

[9] C. Delsart and J. C. Keller. Investigation of the Stark effect in krypton autoionizing Rydberg series with the use of two-step laser excitation. *Phys. Rev. A*, 28:845–849, 1983.

[10] R. D. Knight and Liang-guo Wang. Stark structure in Rydberg states of xenon. *Phys. Rev. A*, 32:896–900, 1985.

[11] W. E. Ernst, T. P. Softley, and R. N. Zare. Stark-effect studies in xenon autoionizing rydberg states using a tunable extreme-ultraviolet laser source. *Phys. Rev. A*, 37:4172–4183, 1988.

[12] T. Jiang, M. D. Bowden, E. Wagenaars, E. Stoffels, and G. M. W. Kroesen. Diagnostics of electric fields in plasma using Stark spectroscopy of krypton and xenon atoms. *N. J. Phys*, 8:202, 2006.

[13] V. P. Gavrilenko, T. Kim, H. J.and Ikutake, J. B. Kim, Y. W. Choi, M. D. Bowden, and K. Muraoka. Measurement method for electric fields based on Stark spectroscopy of argon atoms. *Phys. Rev. E*, 62:7201–7208, 2000.

[14] I. I. Sobelman. Atomic spectra and radiative transitions. *Springer-Verlag, Heidelberg*, 1979.

[15] G. Racah. On a new type of vector coupling in complex spectra. *Phys. Rev.*, 61:537, 1942.

[16] Nist atomic spectra database.

[17] C. Delsart, J. C. Keller, and C. Thomas. Laser investigation of odd krypton Rydberg levels using the field ionisation detection method. *J. Phys. B: At. Mol. Opt. Phys.*, 14(22):4241–4254, 1981.

[18] Y. P. Raizer. Gas discharge physics. *Berlin, Springer*, 1997.

Chapter 4

Measurements of Plasma Breakdown

Abstract

Breakdown processes are important in plasma science but difficult to study because of the highly transient nature. The breakdown process depends greatly on the discharge parameters such as geometry, gas pressure and applied voltage. The goal of this chapter is to study the breakdown processes experimentally with sufficiently high spatial and temporal resolution for the features of breakdown to be observed. Measurements of breakdown at different pressure levels in three different experimental arrangements were made and the results were compared. The main measurement method was the detection of optical emission.

4.1 Introduction

Plasma breakdown is the process that occurs when an electrically neutral gas absorbs enough energy for it to become ionised and electrically conducting. In laboratory plasmas, this is usually achieved by placing a large voltage across two electrodes: the applied electric field accelerates stray charges and begins the breakdown process. Plasma breakdown, also referred to as plasma ignition, is an important fundamental process in plasma science and has a long history of study. In recent years, it has assumed new importance because many plasma applications are influenced by breakdown, and understanding of the breakdown process is necessary for further development of these devices. Such applications are diverse, including cleaning of exhaust gases [1], ignition of light sources [2,3], and material processing using pulsed plasma sources [4,5].

Breakdown theories appropriate for each type of application and each type of operating regime are needed. At high pressure and large applied fields, breakdown is thought to occur via the formation of intense conducting channels called streamers. At low pressure and small applied fields, breakdown usually leads to a glow discharge via a process in which both ionisation by electron collisions in the gas and electron production by secondary electron emission at the electrode surface are important. This process is often called Townsend breakdown [6]. Apparatus parameters, such as the presence of dielectric materials in the electrode gap or dielectric tubes surrounding the discharge volume, greatly influence the type of breakdown that occurs. The type of voltage waveform that is applied, be it pulsed or continuous, dc or ac, positive or negative, also affects breakdown phenomena.

Breakdown theories appropriate for many situations have been developed [6], and the general features that characterise breakdown in different circumstances have become known. However, even for seemingly simple situations, some aspects are poorly understood. For the more complicated discharge systems used in many applications, even general features such as the timing of the breakdown and the necessary voltage can be hard to predict. There is a clear need for greater understanding of breakdown processes, but until recently the very short timescales associated with breakdown made direct experimental studies difficult.

In the research described in this chapter, we examine breakdown processes for several discharge systems by studying images measurement of the total optical emission. The aim of the work was to gain a general overview of important features of breakdown, and to understand how the discharge geometry and other parameters affect these processes. While direct measurements of specific plasma properties are needed in order to fully understand breakdown phenomena, measurement of visible plasma light emission is a simple diagnostic method that provides a good overview of plasma phenomena. With appropriate detection

optics and a high-speed intensified charge-coupled device (ICCD) camera, images with good spatial and temporal resolution can be obtained.

In this chapter, we present observations of the total plasma emission for three different discharge systems. The first was a planar dielectric barrier discharge similar to the microdischarges used in the cells of a plasma display panel. In this system, two electrodes are embedded in a dielectric layer and the discharge occurs above the dielectric surface. The second was a simple two-electrode system operated at low pressure with metallic electrodes separated by a short distance. The third system was a compact discharge tube, with metal electrodes at each end of a glass tube whose length was much greater than its radius. The results for each discharge system were analysed separately to draw conclusions about breakdown processes in each case. The results of all three systems were then compared in order to draw more general conclusions.

This chapter is structured as follows: In the first three sections, the apparatus and plasma emission measurement for each discharge system are presented. These sections are followed by a discussion of the features of breakdown processes which are either pertinent to or observed in each system.

4.2 Breakdown in a PDP-like discharge

Microdischarges, with a discharge volume less than $1mm^3$, have become more common in everyday life, such as plasma display panels(PDP) for large size screen displays [7], backlight sources for liquid crystal displays, surface treatment, and economic ozone production [8]. A typical structure for a microdischarge is two electrodes embedded in a dielectric layer, which the discharge occurs above the dielectric surface. Typically the discharge gap between the two electrodes in a PDP is about 80μm. Modelling studies have been performed for this discharge geometry [9, 10], but few experimental studies exist [11], mainly because of the small size and short lifetime of the plasma.

The aim of the research described in this section was to use direct measurements of plasma emission to examine the basic ignition mechanism of PDP-like microdischarges, but also other surface dielectric barrier microdischarges. This is of interest for both the direct application of such a microdischarges, and for understanding of the basic manner in which dielectric barrier discharges operate.

4.2.1 Discharge apparatus

The discharge apparatus is shown in figure 4.1. It consists of a PDP cell mounted inside a vacuum chamber, a power supply and vacuum system. The vacuum chamber can reach
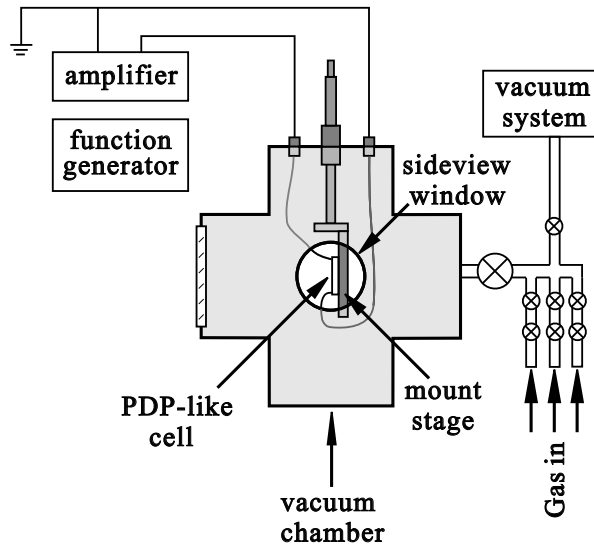
Figure 4.1: Discharge apparatus.

a base pressure of 10^{-4}Pa pumped by a turbo pump and a rotary pump. The PDP cell was mounted on a one-dimensional translation stage such that the vertical position of the cell in the chamber can be changed for easy alignment. Pure argon gas was used for our measurements.

The structure of the PDP-like miscrodischarge cell is shown in figure 4.2, (a) is the cross section of electrode structure. (b) is a picture of the PDP cell. The two square metallic electrodes with 0.26mm side length are embedded in a 30 μm thick dielectric layer, and the surface was covered by a thin MgO layer (600nm) which enhances the secondary electron emission. The two electrodes are separated by 90 μm. We measured the light emission by the discharge from the left pair of electrodes.

An AC voltage was applied to the two electrodes. Its waveform is shown in figure 4.4 and the frequency of the applied voltage was 100kHz, with a peak-peak voltage of about 700V.

4.2.2 Image acquire system

The image acquisition system consisted of an ICCD camera (Andor DH534) and a 5× telescope. The optical diagram of this system is shown in figure 4.3. The size of the sensor chip of the ICCD camera is 13.3×13.3mm^2, and the chip consists of 1024 × 1024 pixels. The photocathode of the ICCD camera was sensitive to all light in the wavelength range from 200-850 nm. Because the window of the vacuum chamber blocks the light which is
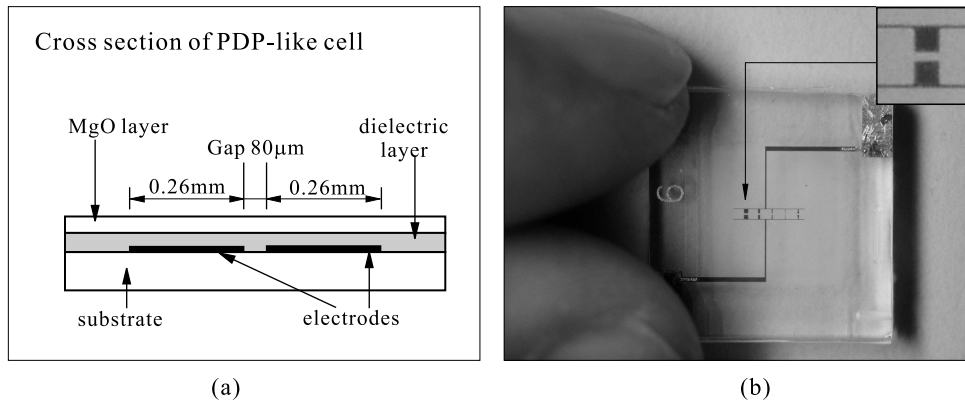
Figure 4.2: PDP-like cell. (a) Cross section of electrode structure, (b) photo of PDP-like cell used in measurement.
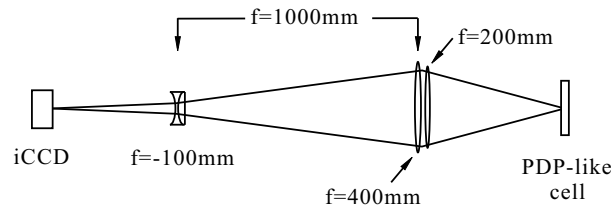
Figure 4.3: Schematic diagram of the ICCD optical system

shorter than 350 nm, it means that only the emission between 350-850 nm can be detected.

The minimal gate width of the ICCD camera is 3 ns and the peak quantum efficiency is about 16% and the maximum gain is about 1000 counts per photoelectron. The gate of the ICCD was synchronized with the discharge voltage pulse by means of a delay generator. By varying the delay between the gating of the ICCD camera and the start of voltage pulse, the light emission for different time intervals in discharge can be obtained. By using the 5× telescope, a spatial resolution of 8 μm (2.7μm/pixel) could be obtained and the temporal resolution was 3 nanoseconds.

4.2.3 Imaging of PDP-like discharge

A set of images measured from the PDP-like microdischarge is shown in figure 4.5. In this part of the voltage cycle, the left electrode was the cathode and right was the anode. Each image in figure 4.5 was obtained with an integration time of 5 ns, and for every image a large number of discharges (near one million) was accumulated. The interval between two images is 50 ns. The figure shows the plasma emission for the most intense part of
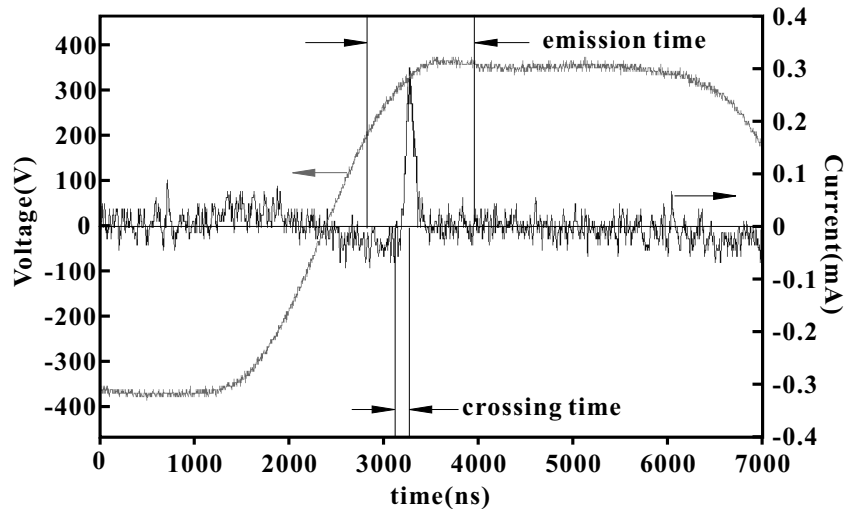
Figure 4.4: Measured current and voltage of PDP-like discharge. The indicated emission time corresponds to the total time span of figure 4.5. The indicated crossing time corresponds to the total time span of figure 4.6

the discharge, and covers a time period of 1.2 μs. By varying the sensitivity of the ICCD camera to record weaker images, emission could be measured for a much longer time.

From the set of images, several distinct phases of the microdischarge were observed. Initially, emission was observed above the anode when the applied voltage increases (see figure 4.4). This phase is corresponding to the images from time of 2800ns to 3050ns. The intensity of the plasma emission gradually increases in this period. Secondly, this emission region moved across the gap between the electrodes until it was above the cathode. This phase is related to the images from time of 3100ns to 3250ns. Thirdly, the emission continued to increase in brightness to a peak; finally it died away gradually. This corresponds to images from time 3300ns to 4000ns.

The images shown in figure 4.5 were obtained with a relatively long interval, so rapidly changing features, especially for the phase when the emission region moveds across the discharge gap, can not been seen very clearly. In order to examine the emission during the time that breakdown occurred, a further set of measurements with better time resolution were obtained and they are shown in figure 4.6. The interval between two images was 5 ns. The total time span of this set of images includes the range where the current is increasing sharply, usually called "breakdown current". The images clearly show that the plasma emission front "jumps" over the electrode gap, while the intensity of the emission increases greatly during the crossing process.

The regions where emission is visible in the images can be associated with regions
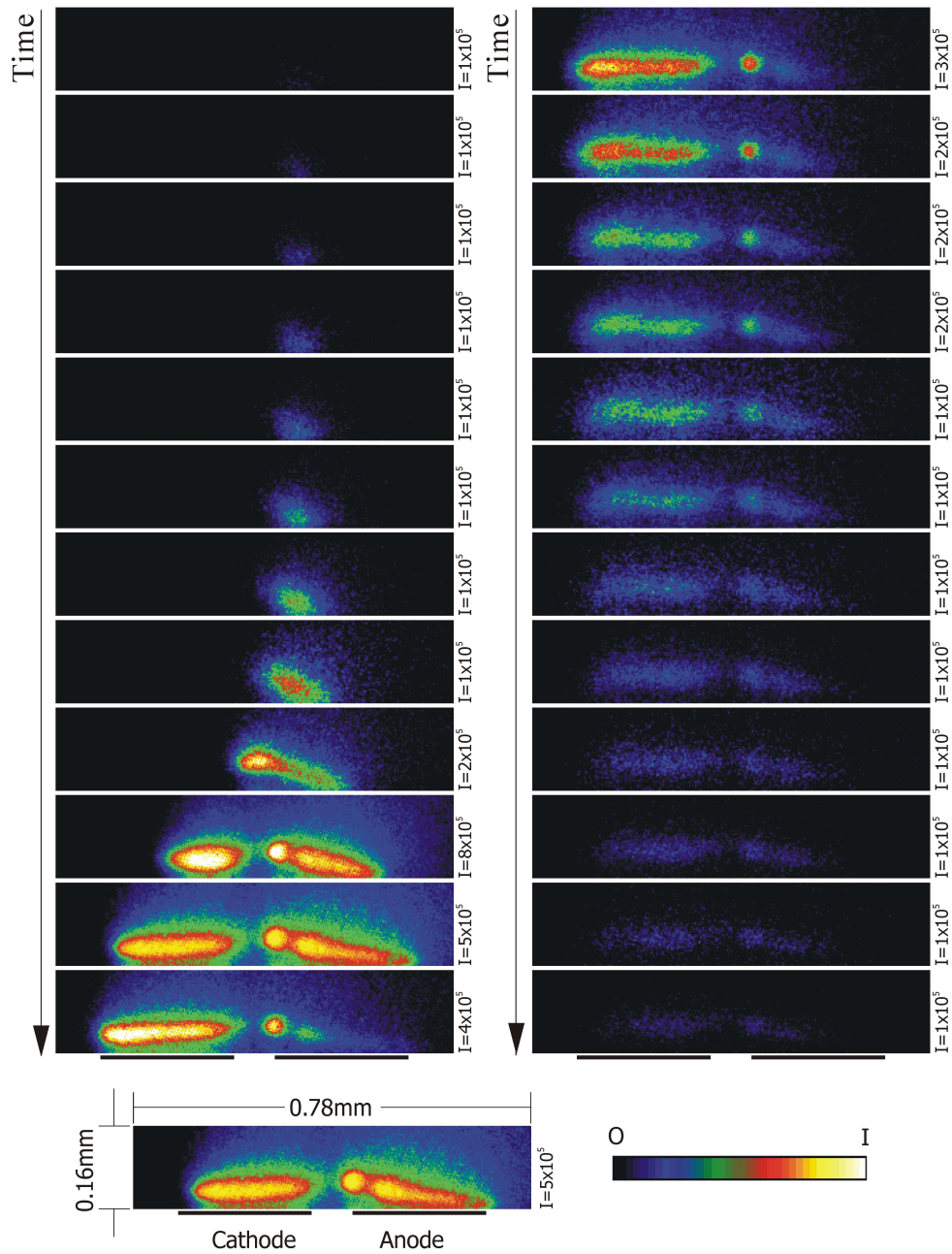
Figure 4.5: Sequence of ICCD images showing the half cycle of PDP-like discharge. Each image was obtained with an integration time of 5 ns, and was the result of the accumulation of all discharges within a total time of 8 seconds. The interval between two images is 50 ns. At the right hand side of each false color picture the value corresponding to the maximum of the false color scale is noted. The first image in time sequence is the top one of the left image group , and the last one is the bottom one of right image group.
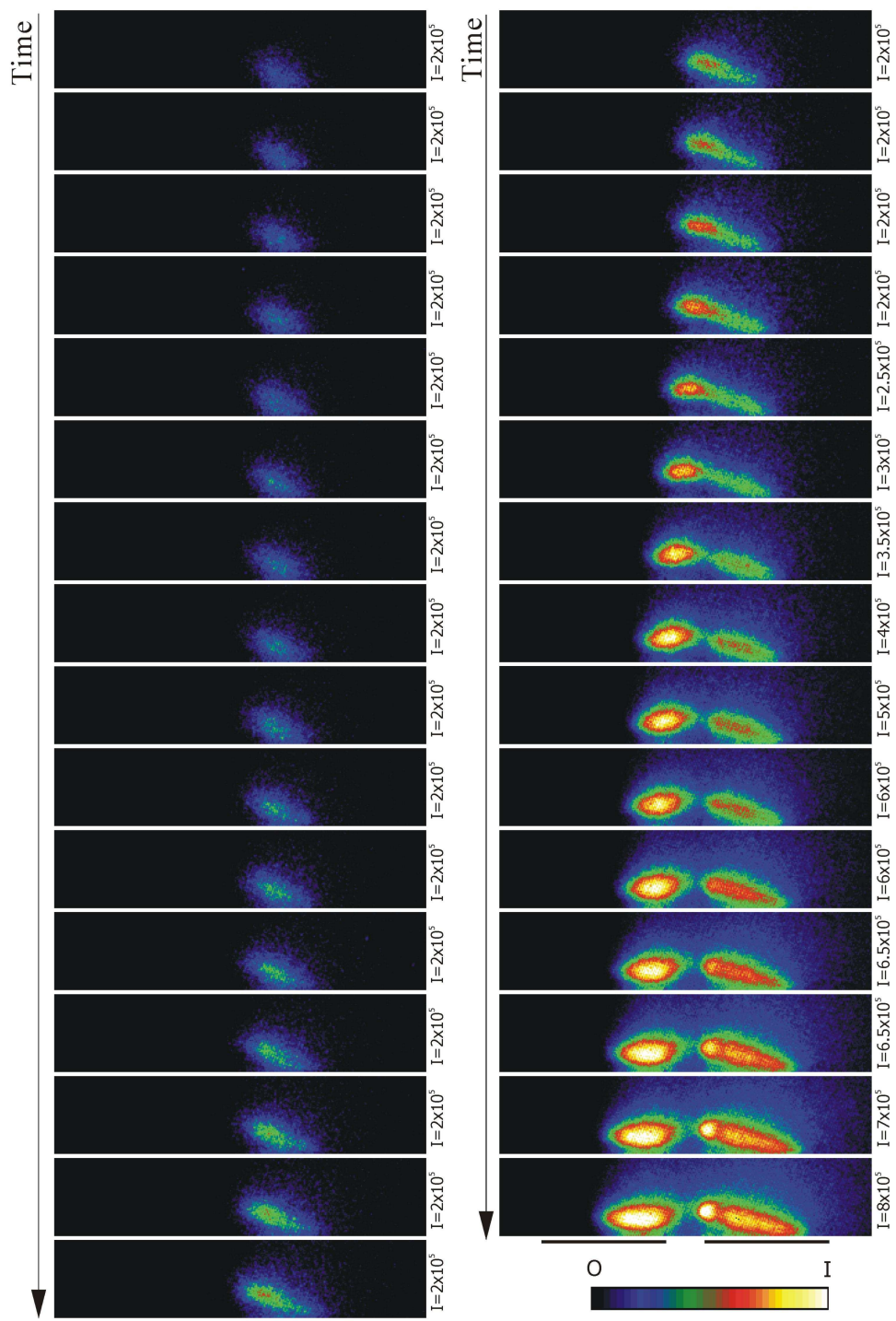
Figure 4.6: Sequence of images showing the light emission front that moves across the discharge gap. Each image was obtained at an integrating time of 5 ns, and is an accumulation of few hundreds thousand discharges.

where electrons have sufficient energy to cause excitation reactions with the background gas atoms. The energy needed for excitation and ionisation processes is about equal, and the lifetime of the excited states is in order of tens of nanoseconds for these discharge conditions. Hence, we can conclude that intense emission also indicates significant ionisation. Consequently, the set of images in figure 4.5 also can be interpreted as showing a region of ionisation buildup near the anode, which then moves across the electrode gap towards the cathode.

The observed phenomena are consistent with the conventional view of Townsend breakdown towards a glow discharge. Initially, when the applied voltage increases, some electrons are released by the MgO surface that were trapped during the previous discharge (with opposite voltage polarity). These so-called priming electrons are then accelerated by the applied anode voltage towards the anode. Close to the anode these electrons will achieve their highest energy, so this is where the ionisation starts first, creating an avalanche of electrons and increasing the ion density. With the applied voltage increasing continuously, more electrons will reach the anode area with even higher energy, in a continuous avalanche process, rapidly increasing the intensity of the emitted light.When the build-up of ions in the volume is high enough to screen the anode and to modify the potential between the electrodes, then the anode potential plane will move from the anode into the gas space, thereby increasing the electrical field strength at the cathode. This process can be seen in the emission images in figure 4.6, where the light emission rushes over the discharge gap from anode to cathode.

As was noted before, the first emission occurs above the anode surface, and does not occur at the position of maximum electric field (just above the region between the electrodes). This is consistent with the fact that the electrons follow the electric field lines while moving towards the anode surface. The ionisation wavefront develops in the opposite direction towards the cathode, forming a sheath above it, while the current reaches a maximum.

Once the ionisation wave front reaches the cathode, the Ar-ions and /or meta-stables might generate additional secondary electrons at the MgO cathode surface; the γ-value for ion-induced secondary electron emission for argon, however, is rather low.

In the case of argon, the ions stay on the MgO surface by electrostatic effect, effectively charging the capacitor formed by the dielectric layer between the cathode and the plasma. In the case of helium, the ions will generate secondary electrons through the Auger Neutralisation mechanism [12, 13]. In that case, ions generate electrons by the MgO surface instead of the positive ions attached to the surface. Because of the additional generation of electrons by the MgO surface in the case of helium, the firing voltage of the discharge will be much lower than for argon.

While charging the dielectric surface, the electric field across the gas is reduced, finally resulting in termination of the electron avalanche process, because of the neutralisation of the applied voltage to a level below the firing voltage.

The main conclusion that we can draw from the images of the PDP-like microdischarge is described as a single pulse Townsend discharge.

During the discharge, electrons were trapped on the anode surface. After the self-extinguishing phase and during the reversing of the voltage polarity of the discharge, they will be released again by the strong electrical field. They will then serve as a source of priming electrons from the cathode surface during the new discharge phase.

Finally, we have to note that in the case of metal electrodes the same discharge phenomenon have been found to occur, compared to those described above. This will be described in the next section. In the case of metal electrons however the source of priming electrodes has not been clearly identifired.

4.3   Breakdown to a glow discharge at low pressure

A discharge generated between metallic electrodes at low pressure is one of the simplest types of discharges. For the case of most simple discharge gases, the breakdown processes are reasonably well understood, and the breakdown to a stable discharge is expected to occur according to the so-called Townsend breakdown theory [6]. Hence, we expect that electron avalanches will cross the gap between the electrodes, steadily increasing in intensity until the whole region becomes sufficiently ionised for sheaths to develop at the electrode surfaces and a stable discharge to become established.

In the research described in this section, we analyse the breakdown processes in such a simple system by measuring the optical emission with an ICCD camera. The aim of this study was to identify the key features of the breakdown and to determine how the observed emission can be understood in terms of the standard breakdown theory. In addition to the aim of understanding breakdown in this particular system, we hope that the results from this relatively simple experiment will be useful in interpreting similar measurements made in more complicated discharge systems.

The electrodes used in this study were cylindrically symmetric and made from stainless steel. They were parabolic shaped and the tip had a curvature equivalent to radius of 4 mm. The motive for this shape is to be able to generate a reproducible discharge, both temporally and spatially. The gap between the electrode tips was 3.3 mm. The electrodes were positioned in the centre of a vacuum chamber filled with continuously flowing argon gas ar a pressure of 465Pa(3.5 Torr).

The discharge was generated by applying short pulses of a positive voltage to the upper
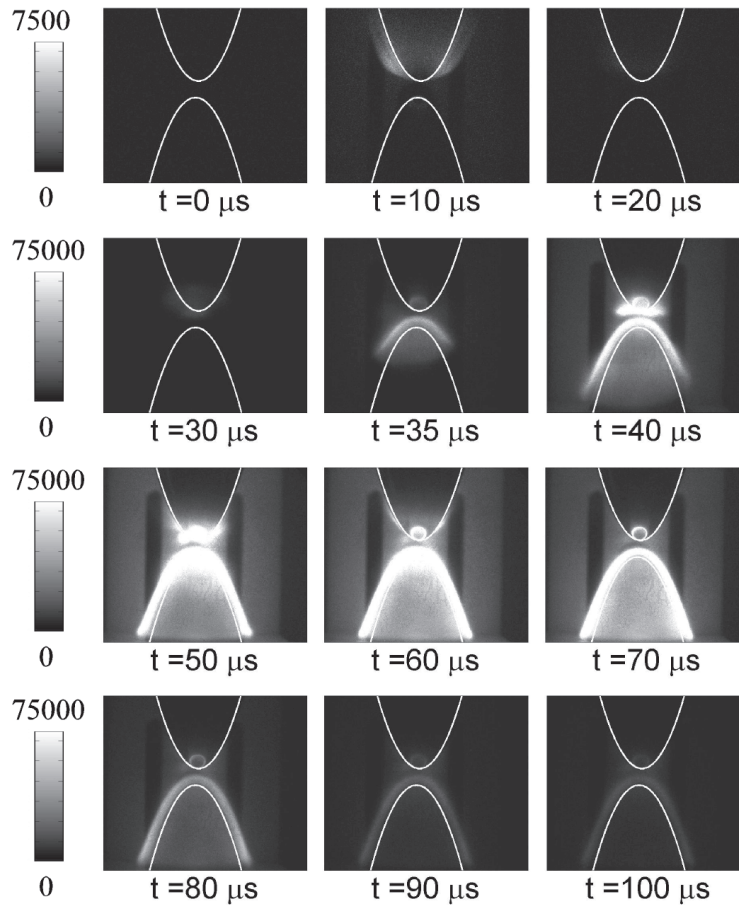
Figure 4.7: ICCD images of plasma breakdown. The top electrode is the anode, the bottom one is the grounded cathode. The color scale of the first three images is 10 times smaller than the rest of the images. See reference [14]

electrode. The lower electrode was kept at 0 V. The amplitude of the applied voltage pulses was 300 V, the pulse duration was 120 μs and the pulse repetition rate was 500 Hz. Compared to the 2 ms cycle, the 120 μs period of the discharge is rather short. The voltage pulse had a rise time of 25 μs.

Figure 4.7 is a series of ICCD images that shows an overview of plasma emission during the a complete breakdown cycle. The images between 10 and 20 μs show a week light flash occurring near the anode [14]. After 30μs, weak light emission appeared near the anode again. and the light emission had crossed the discharge gap and covered part of the cathode surface (image of 35 μs). Then the bright glow-like discharge emission covered the entire cathode surface and stabilized (images of 60 and 70 μs). This emission pattern

remained before the voltage dropped . After 70 μs, a brief afterglow plasma was observed which died out (80-100μs) when the voltage decreased.
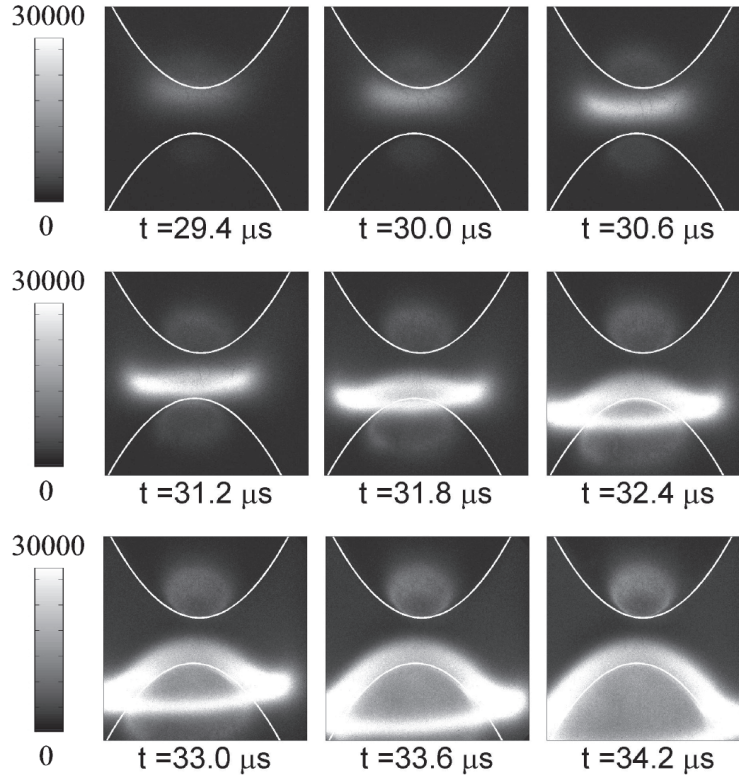
Figure 4.8: Sequence of images showing the formation of an emission front that moves across the electrode gap. Each images was obtained by integrating time of 100ns, and is an accumulation of 3000 discharges. taken from reference [14]

The emission crosses the discharge so rapidly that the changing features cannot be seen in detail in figure 4.7. A set of images with better spatial and temporal resolution is shown in figure 4.8. The set of images relate to a time range between 29 and 35 μs.

The features observed in the above two sets of images are consistent with standard low-pressure Townsend breakdown theory [6]. Initially, no light emission is observed because of the low electron density. Then, the continuous electron avalanches due to the secondary electron emission become stronger with time until they are sufficiently intense to cause observable light emission in front of the anode. Subsequently, the multiple electron avalanches cause a build-up of ions in front of the anode which modifies the electric field distribution in the discharge gap and screen the anode. this cause the anode potential to be extended into the discharge gap towards the cathode, so the light emission moves from anode to cathode.

Although this breakdown occurs over a much longer time than which in a PDP-like discharge, the behaviour of the plasma emission is remarkably similar to the emission of PDP-like discharge during the process of breakdown. As in that case, the moving emission region can be associated with an ionisation front. The front builds up on the anode and moves across the discharge gap to the cathode.

It can be concluded that the physical processes which occur during that the formation of the ionisation front are basically the same as those for the very different case examined in section 2.

4.4 Ignition of a straight discharge tube

The ignition phase of a straight discharge tube has been studied for many years and the general features are thought to be reasonably well understood. Previous studies have noted the importance of the tube and the surrounding electrical environment [2, 15]. However, some aspects of the discharge ignition are still poorly understood. Using an ICCD camera, the light emission during the breakdown process was investigated.
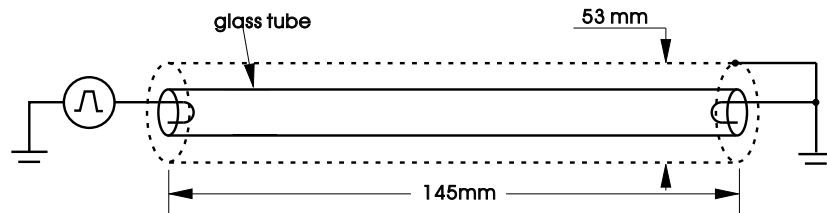
Figure 4.9: Schematic diagram of the straight discharge tube used for these studies. The glass tube has a inner diameter of 10 mm, outer diameter 12.5 mm. A inner diameter of 53 mm Faraday shield around the tube provides a stable electrical environment. See the Ph.D thesis of M. F. Gendre [16]

The dimensions of the gas discharge tube used in this research were based on those for a compact fluorescent lamp and they are shown in figure 4.9. Its length was 145 mm, with a inner radius of 5 mm, and the gas pressure was 3 Torr. The discharge was ignited with a pulsed dc voltage with a rise time of 3 μs and an amplitude of about -600 V. The voltage was applied to the cathode, and the anode was kept grounded at 0 V. The cathode filament was heated with a dc current to produce a constant flux of electrons via thermionic emission. In order to create a stable electrical environment, the discharge tube was surrounded by a grounded metal tube with a diameter of 53 mm.

Figure 4.10 shows the emission from the discharge tube at different times after the voltage pulse was applied, measured with an ICCD camera in the same manner as in
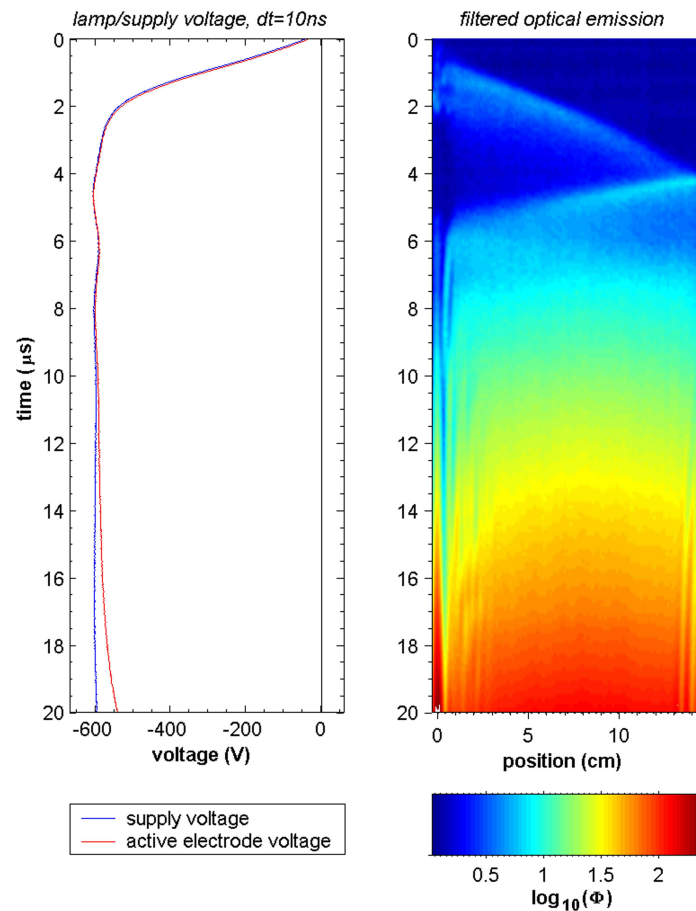
Figure 4.10: Schematic diagram of the straight discharge tube used for these studies. The glass tube has a inner diameter of 10 mm, outer diameter 12.5 mm. A 53 mm inner diameter Faraday shield around the tube provides a stable electrical environment. See the Ph.D thesis of M. F. Gendre [16]

the other two cases discussed before. Several distinct phases can be distinguished: 1) A short initial period, during which the voltage pulse reaches its peak. 2)A region of bright emission which moves from the cathode to the anode. 3) A second moving front, which propagates from the anode back towards the cathode. After this, the emission increases steadily all through the discharge tube, until a sharp transition stage in which the tube voltage drops, the tube current rises, and the discharge becomes stable. An important experimental observation is that the discharge will proceed to full breakdown only if the first emission front reaches the anode.

Discharge Property	PDP-like microdischarge	two electrode discharge	compact discharge tube
pressure p (Torr)	375	3.5	3.0
Max. applied voltage (V)	380	350	600
characteristic length (cm)	0.009	0.33	2.75/0.5 [1]
pd (Torr·cm)	3.375	1.15	8.25
Max.E/p (V·cm^{-1}·Torr^{-1})	113	303	73

Table 4.1: Comparison of important features of the discharge systems.

4.5 Discussion

When comparing the results obtained from the three systems examined above, it is useful to analyse the similarities and differences. There are obvious material and geometric differences, such as the dielectric material and MgO surface used for the PDP-like microdischarge, instead of the metal electrodes in case number two and the glass discharge tube in the third case. However, there are also differences in pressure and applied voltages. For studying the breakdown of the discharge, it also is appropriate to compare the pressure and dimension product pd and the electric field to pressure ratio E/p. The values for each discharge shown in the table 4.1.

It can be seen from the table 1 that the values of pd for each case are similar, while the values of maximum E/p range over an order of magnitude. Although the three discharges appear at first glance to be extremely different, there are some similarities. This similarity also could be inferred from the fact that in each case the system breaks down into a glow discharge rather than a filament, arc or other type of discharge. This is true even for the microdischarge, although in this case the discharge extinguishes before the stable situation is reached. When we compare the results obtained for the three discharges, we should expect the differences to be the result of geometric and material effects as well as intrinsic pressure and dimension effects.

When comparing the emission images from the three discharges, the obvious similarity is that an emission front is a key feature of the breakdown process in each case. In each case, this moving emission front, which we can assume to be associated with a region of large potential gradients, high electric fields and large ionisation, is very localised in space. It is also worth noting that, in the cases for which this could be verified, complete breakdown was characterised by a successful crossing of the front from one electrode to the

---

[1]For the discharge lamp, there are two important dimensions. The distance from electrode to ground is 3.0 cm, while the characteristic dimension of the discharge itself is the radius, which is 0.5 cm.

other.

Another conclusion that can be drawn is that breakdown processes in the first two cases were very similar. The presence of the dielectric surface in the pdp-like microdischarge prevented the discharge from becoming fully stable, but until the time at which the discharge began to extinguish, the breakdown processes in the pdp-like cell appeared to be proceeding in an almost identical manner to that observed in the basic two-electrode case. From this, we can conclude that the breakdown mechanisms in the two cases were very similar. The charges that reside on the dielectric surface will influence the electric field, and can perhaps also supply the first electron avalanches with seeding charges. However, from these measurements, we can only conclude that their presence does not make a qualitative difference to the processes that lead to the discharge being formed. We note that a different conclusion was reached in the study of Kozlov et al. [17], perhaps because of the different geometry and pressure of their system.

It can be concluded that the presence of the dielectric tube in the third system greatly influenced the breakdown process. Furthermore, the fact that the cathode was heated so that it continually emitted electrons into the gas makes this system behave differently. In this system, one clear phenomenological difference is that there is a first ionisation front that moves from the cathode to the anode, preceding the other ionisation wavefront from anode to cathode, also as observed in the other two systems. Also in this case, the ionisation moves down the tube because the wall of the tube become charged. thereby altering the applied electric field. Hence, the front moves because of a surface charging process, rather than because the volume charge builds up significantly.

Therefore, we can see that there are significant difference between the breakdown phenomena in the discharge tube on one hand, and the simple electrode system and the pdp-like microdischarge on the other hand. Nevertheless, the generation of an ionisation front is the critical feature of breakdown in all cases, even though the generation mechanism is different. Hence, the problem of optimising breakdown for any given situation might be reducible to the problem of generating the ionisation front that is necessary for breakdown to occur.

4.6   Conclusions

Using an ICCD camera, the plasma breakdown of several discharge systems has been studied. These measurements provide a good overview of the breakdown in each situation, and allow us to identify the crossing of an ionisation wave. The influence of the different material properites and different system geometries could be observed.

To understand specific details of each breakdown situation and to enable us to make

more comprehensive comparisons, direct measurement of specific plasma properties such as the spatial and temporal development of plasma emission lines during breakdown, electric field with Stark spectroscopy etc are needed.

References

[1] E.M.van Veldhuizen. Electrical Discharges for Environmental Purposes: Fundamentals and Applications. *Huntington: Nova Science Publishers*, 2000.

[2] R. E. Horstman and F. M. Oude Lansink. The starting process in long discharge tubes. *J. Phys. D: Appl. Phys.*, 21(7):1130–1136, 1988.

[3] W. J. M. Brok, J. van Dijk, M. D. Bowden, J. J. A. M. van der Mullen, and G. M. W. Kroesen. A model study of propagation of the first ionization wave during breakdown in a straight tube containing argon. *J. Phys. D: Appl. Phys.*, 36:1967–1979, 2003.

[4] T. Sugai, H. Yoshida, T. Shimada, T. Okazaki, and H. Shinohara. New synthesis of high-quality double-walled carbon nanotubes by high-temperature pulsed arc discharge. *Nano Lett.*, 3:769–773, 2005.

[5] R. Dorai and M. J. Kushner. Repetitively pulsed plasma remediation of NO_x in soot laden exhaust using dielectric barrier discharges. *J. Phys. D: Appl. Phys.*, 35(22):2954–2968, 2002.

[6] Y. P. Raizer. Gas discharge physics. *Berlin, Springer*, 1997.

[7] J. P. Boeuf. Plasma display panels: physics, recent developments and key issues. *J. Phys. D: Appl. Phys.*, 36(6):R53–R79, 2003.

[8] G. J. Pietsch and V. I. Gibalov. Dielectric barrier discharges and ozone synthesis. *Pure. Appl. Chem.*, 70(6):1169–1174, 1998.

[9] G. J. M. Hagelaar, G. M. W. Kroesen, U. van Slooten, and Schreuders H. Modeling of the microdischarges in plasma addressed liquid crystal displays. *J. Appl. Phys.*, 88(5):2252–2262, 2000.

[10] K.W. Whang and J. K. Kim. Discharge physics of alternating current plasma display panels (PDPs). *J. Comput. Phys.*, 1(2):295–303, 2005.

[11] R. Ganter, J. Ouyang, T. Callegari, and J. P. Boeuf. Physical phenomena in a coplanar macroscopic plasma display cell I. infrared and visible emission. *J. Appl. Phys.*, 91(3):992–999, 2002.

[12] H. D. Hagstrum. Theory of auger neutralization of ions at the surface of a diamond-type semiconductor. *Phys. Rev.*, 122(1):83–113, 1961.

[13] Y. Motoyama and F. Sato. Calculation of secondary electron emission yield γ from MgO surface. *IEEE Trans. Plasma Sci.*, 34(2):336–342, 2006.

[14] W. Wagenaars, M. D. Bowden, and G. M. W. Kroesen. Plasma emission imaging of a low-pressure argon breakdown. *Plasma Sources Sci. Technol.*, 14(2):342–350, 2005.

[15] A. V. Nedospasov and A. E. Vovik. *Sov. Phys.-Tech. Phys*, 5:1261, 1988.

[16] M. F. Gerder. Electrical breakdown in low-pressure discharge lamps: Pouly-diagnotic investigations. *to be published 2007.*

[17] K. V. Kozlov, H. E. Wagner, R. Brandenburg, and P. Michel. Spatio-temporally resolved spectroscopic diagnostics of the barrier discharge in air at atmospheric pressure. *J. Phys. D: Applied Physics*, 34(21):3164–3176, 2001.

Chapter 5

Atmospheric cold plasma

Abstract

A linear array of DBD surface discharges in the form of a flat plate, coated with an Al_2O_3 layer was used to generate a plasma in helium gas at one atmospheric pressure, in the presence of impurities from air; the discharge gap was 70 μm and the dielectric barrier was 30 μm thick.

At one atmosphere stable discharges are achieved using a square wave external voltage of about 300 Volt at frequencies from 20-100 kHz. The spectrum of the emitted light shows strong emission lines of the OH radical at 309 nm, in addition to N_2^+ (391 nm) and helium emission lines. The intensity of these lines was determined as a function of the applied frequency and the helium flow rate; also the time dependent behaviour was studied in detail.

It is concluded that the OH (309 nm) emission at atmospheric pressure is especially strong because of the photo-dissociation process, that might be responsible for the OH creation. The micro-plasma array plate with surface discharges in helium promises to be an imported tool for the creation of OH radicals and the generation of non-coherent 309 nm radiation, both of which might be used of sterilisation or treatment of skin diseases.

5.1 Introduction

5.1.1 Background

An electric discharge in gas produces a plasma: a medium that is unique in terms of electric properties and chemistry. The plasma releases charged species, short-living active radicals and energetic photons that are capable of very specific surface treatment. In the past decennia, plasmas have made an enormous career in solid state surface technology. Plasma processing of non-living materials, such as semiconductors, fabrics and even biological scaffolds, have become an indispensable techniques in industry. The largest added value in surface processing is achieved with the use of non-equilibrium (non-thermal or "cold") plasmas. These discharges contain energetic electrons at several eV, while the gas temperature remains relatively low. Cold plasmas range in temperature from room temperature to several hundreds of degrees Celsius. This is a comfortable temperature range, in which many (non-living) materials can be processed without thermal damage. Initially, surface treatment was performed exclusively by means of low-pressure plasmas, at $10^{-5} - 10^{-3}$ atm. This is because non-equilibrium conditions are easy to obtain at reduced pressures, which means that at low-pressure discharges are cold by nature . The performance of low-pressure plasmas is very high, and their versatility is enormous: the feasible processes include directional (anisotropic) etching, deposition of complex (e.g. nano-structured) layers and surface cleaning. In the biomedical area, bacterial sterilisation [1–3], biocompatible coatings [4] and surface functionalisation for cell adhesion and growth [5,6] are the best known applications.

The main drawback of low-pressure processing is the use of vacuum reactors. Firstly, vacuum equipment is inconvenient in operation: the costs are high, flexibility is low, materials to be processed must be introduced in batches, and contamination can occur during sample transfer in and out of the reactor. Furthermore, typical reaction rates at reduced pressures are low, and thus processing times are relatively long. Finally, the versatility is limited, because a large category of materials cannot withstand vacuum conditions. For example, vulnerable, porous organic materials, liquids, foodstuffs and living plant/animal tissues cannot be processed in low-pressure plasmas. Recently, new trends in plasma technology are visible: non-thermal atmospheric sources are constructed, and novel technologies of material processing by means of cold atmospheric plasmas are introduced [7,8]. At present, the main challenges are:

1. To replace low-pressure plasmas with atmospheric sources in traditional surface treatment.

2. To expand the applicability of plasma treatment to new categories of materials.

In the first approach, the major challenge lies in maintaining the same performance that is achieved by low-pressure plasma technology. In some cases this is relatively easy. Several techniques, such as cleaning, spraying, deposition, etc. do not drastically depend on specific properties of low-pressure plasma sources, so they can be easily adapted for ambient pressures. In addition, all chemical (gas phase and surface) reactions are much faster at atmospheric pressures, simply because of the 1000-10000 higher densities of reactants. However, some specific techniques, like anisotropic etching, rely on specific properties (electric field and chemistry) of the low-pressure plasma sheath; these techniques may be difficult to adapt.

The most common methods to generate (reasonably) cold plasmas under ambient pressures are surveyed in the next section. High frequency plasma jets, torches, needles, microwave sources and surgical plasma coagulation units are introduced and their properties are briefly described.

5.1.2 Methods of generation

Recent years have brought much progress in construction, operation and control of non-thermal atmospheric gas discharges. There are few general rules for obtaining an ionised medium in a non-equilibrium condition; these rules are valid at atmospheric as well as reduced pressures. Firstly, the electric signal used to drive the discharge should be either high-frequency, or transient with a short duration (ns-μs). This is to assure that only the light charge carriers (electrons) are able to respond and gain energy from the rapidly varying field. Secondly, the energy transfer from electrons to heavy particles should be made as inefficient as possible. This is easily obtained at reduced pressures, where all collisions are scarce. At atmospheric pressure in air the electron-atom collision frequency (ν_{ea}) is $2 \cdot 10^{12}$ Hz (momentum transfer) and $3.5 \cdot 10^7$Hz (energy transfer, ν_{ea}) multiplied with electron to atom mass ratio, m_e/m_a) at 1 eV electron energy (T_e). These numbers do not vary much for other gases and electron energies. To obtain non-thermal plasmas, one can thus only keep the electron density low, so that this energy transfer is minimised. In high-frequency discharges, electron-induced gas heating by elastic and inelastic collisions is the most important channel to dissipate the input power. Typical charge densities in non-thermal atmospheric plasmas are not lower than 10^{16} m^{-3}, and typically about ten to hundred times higher; the electron temperature is usually 1 eV or more. The power (or actually the power density) transferred from electrons to heavy particles per cubic meter of plasma volume is:

$$P = \frac{m_e}{m_a}n_e\nu_{ea}kT_e = 5.6 \cdot 10^5 - 10^6 W \cdot m^{-3}$$

at 1 eV and at the electron density of $10^{17} - 10^{18}$ m^{-3}. This can be seen as the minimum power necessary to sustain a plasma with the above given specifications: a MW flows from electrons to neutrals, so at least this power must be coupled into one cubic meter of discharge. Just for the comparison, the energy needed to heat a 1 m^{-3} of air is only 1.29 kJ K^{-1}. A MW of power is enough to heat the gas to a thousand degrees in just one second, and this would happen in a well-isolated system. On the other hand, sustaining one cubic meter of plasma with so little losses is not realistic. Man-made atmospheric plasmas tend to be small and self-constricted even in absence of external constraints. This is because the plasma activity (ionisation, etc.) can be sustained only above a certain value of the electric field strength, e.g. $3 \cdot 10^6$ V/m for air, and it is difficult to generate such high fields in a large volume. Thus, the plasma burns only in the high-field region, which is usually small, and it recombines quickly outside. An example of such a transition between the active plasma and the recombining afterglow has been treated numerically by Brok et al. [9]. In practice, common devices generate high electric fields by using narrow electrode gaps (few mm) or pointed electrodes. Naturally, such fields are spatially non-uniform, and the resulting typical dimensions of atmospheric plasmas are in the order of a few mm (plasma volume of about 10^{-8} m^{-3}). In such configurations, the power dissipated by electrons is only about 50 mW, which can be easily carried away due to various energy losses, such as thermal conduction, convection, fluid evaporation and radiation. In the examples given below it is shown that small size plasmas, with power input of about 1 W or less can be constructed, and that their temperature can be kept at the level that is comfortable for processing of organic materials. These plasmas seem to be the best choice for living tissue treatment. Other, more powerful sources can be also used, but preferably in the downstream/afterglow mode, i.e. where no power from the generator is coupled into the gas.

In designing cold plasma devices, two approaches can be distinguished: 1) reducing the input power and 2) enhancing the heat losses. To reduce the effective power, the following principles can be employed:

A   Reduction of operating voltage. The well-known Paschen breakdown curves predict the lowest breakdown voltage for noble gases: helium, neon and argon (e.g. [8]). Many non-thermal atmospheric sources are operated in helium; for example, at 200 V and a few mm electrode gap. Sources fed with argon tend to be hotter and more prone to arcing. In contrast to noble gases, plasmas operated in air require high breakdown voltages, and are usually filamentary and unstable.

B   Reduction of discharge current. This is the principle employed in dielectric barrier discharges (DBDs). The dielectric layer covering the electrode acquires charge upon

contact with plasma; this charge reduces further influx of charged plasma species and thus limits the plasma current.

C   Reduction of duty cycle. Plasma ignition requires only a certain voltage/field strength, but the electric signal need not be applied continuously. An effective method to reduce the power is to apply short (e.g. microsecond) pulses. The major advantage of this approach is that the actual voltages can be quite high (1-10 kV), which helps to sustain high ionisation rates and a high plasma activity.

To enhance heat losses from the source one can consider the following construction features:

a   Reduction of plasma surface to volume ratio. This serves to increase the losses by thermal conduction, and is the cooling principle in micro-plasmas.

b   Introduction of convective cooling. This is a very effective way to reduce the temperature of the plasma glow. Many designs employ large forced flows (several l/min) and resulting gas flow speeds on several m/s.

c   Introduction of volatile matter. Plasma can be operated in the vicinity of water or other liquids. For example, electric breakdown can be created under water, in a bubble of evaporated liquid; alternatively, liquid can be introduced into the plasma jet, or the plasma can be sustained in a chamber with a suspension of liquid droplets. The heat required for evaporation of the liquid forms a substantial energy sink.

Of course, combinations of these methods are possible. Below we shall briefly describe few examples of cold plasma sources that are currently used or considered for medical and environmental applications. For the particular source designs, the cooling principles (A-C, a-c) listed above are indicated.

1. Atmospheric Pressure Plasma Jet (APPJ) (A, b) [10, 11]. A radio-frequency (RF) jet was first introduced by the group of Selwyn. It is sustained at 13.56 MHz in a bipolar/coaxial configuration: a rod electrode confined in a 15 cm long grounded tube. The jet length is about 1 cm; power consumption is rather high (50-100 W), but forced convective cooling (50 l/m and 30 m/s gas flow and speed, respectively) keeps the temperature at moderate levels (100 ℃). APPJ operates in helium with admixtures; it can be used for etching, cleaning and bacterial decontamination.

2. Argon Plasma Coagulator (APC) (A, C, b, c) [12, 13]. This is the coagulation unit developed and commercialised by ERBE, which has been successfully used in numerous medical procedures (see figure 5.1). The design and power consumption (50-100
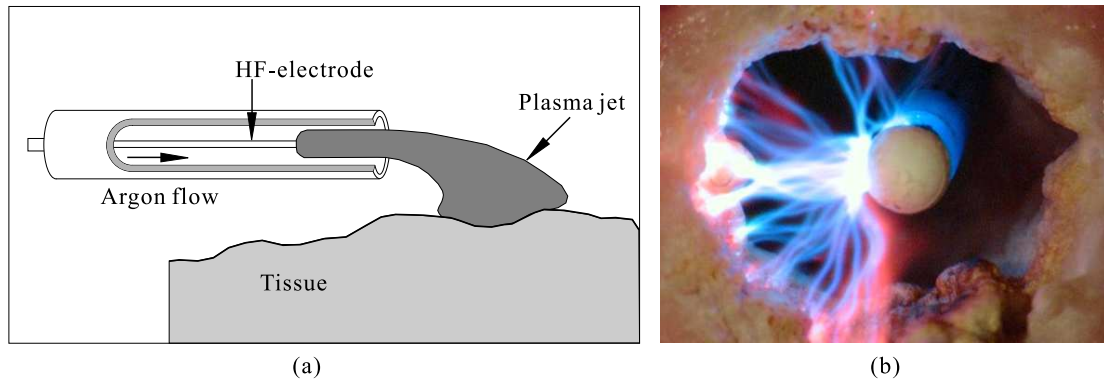
Figure 5.1: The Argon Plasma Coagulator (high-frequency atmospheric jet for various surgical application): a) is a schematic view of the device and b) is a picture of the discharge. Reporduced with the courtesy of Drs J. Raiser and M Zenker, ERBE-MED, Tübingen, Germany.

W) are similar to the APPJ, but the driving frequency is lower (350 kHz) and the feed gas is argon. An example of such a device is depicted in figure 5.1. APC was directly derived from an electrosurgical coagulation unit - a monopolar device, which applies electric current to the subject (the patient) and causes local tissue/blood coagulation at the point of highest current density, i.e. closest to the powered electrode. In APC the current is transferred through the ionised gas, so that treatment is essentially non-contact. Furthermore, plasma temperature of 100 ℃ and the action of charged particles contribute to devitalisation of the tissue. Nowadays other variants of coagulation units have been introduced, such as bipolar configurations and pulsed discharge operation. Numerous surgical applications are described in the next section.
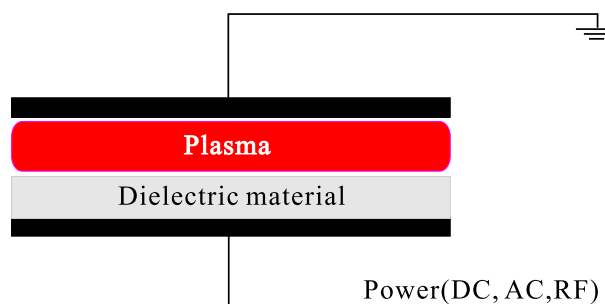
Figure 5.2: A general scheme of a dielectric barrier discharge (DBD). A dielectric layer may be place on one or both electrodes.

3. Dielectric Barrier Discharges (DBD) (A, B, C, a, b) [7, 14–16]. This is a very broad class of plasma sources. Usually the plasma is created between closely spaced parallel plates, where one or two plates are covered by a dielectric layer (Figure 5.2). Operating frequency can be AC (50 Hz, or in the kHz range) as well as RF, power consumption is 10-100 W. The plasma surface to volume ratio is large, and gas flow provides convective cooling. Pulsed operation is also possible [16]. One can obtain homogeneous discharge using noble gases (helium), but in presence of electronegative species (air) filaments are readily formed. DBDs can be used for bacterial decontamination, but the practical limitation is the narrow spacing between the electrodes, so that sample introduction is difficult. Downstream treatment is of course possible.
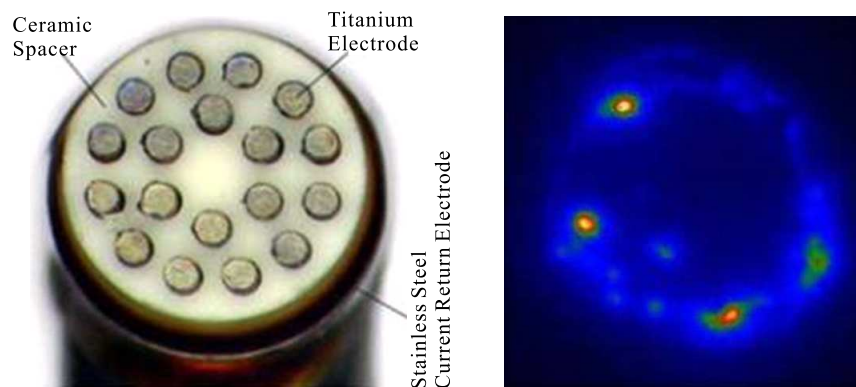

Figure 5.3: A device to create electric discharge in saline solution(left), and the CCD image of the discharge(right). Reproduced with the courtesy of Dr. K. R. Stalder, ArtheroCare Corp. Sunnyvale, CA.

4. Discharge in saline solution (C, a, c) [17–19]. This is an example of under-water corona discharge created by short (e.g. microsecond) electric pulses. The electrode is a "showerhead" of thin electrodes, which create small-size discharges in bubbles of evaporated liquid (Figure 5.3). These transient plasmas last for several milliseconds, but the total power is about 100 W. The plasma is particularly reactive because of efficient production of OH radicals. The action of this device is referred to as coblation. Simultaneous cutting and cauterisation, as well as non-thermal modification of connective tissue [17] are possible. The effects are fast, like is traditional surgery - the tissues are physically removed. Medical applications lie in arthroscopy, otorhinolaryngology, spine surgery and cosmetic surgery.

5. Atmospheric Pressure Glow Discharge - Torch (APGD-t) (A, a, b) [20]. This torch can be seen as a miniature plasma jet. Plasma is generated at 13.56 MHz in flowing

helium (1 l/min), power consumption is about 1 W. The glow is 0.5 mm in diameter and a few millimetres in length. An interesting design detail is that the injection of active species is done not directly in the feed gas, but in the downstream zone. This assures low ignition voltage due to the usage of pure helium, as well as sufficient production of chemically active species, necessary for effective surface treatment. APGD-t is used for surface treatment and studies on plasma interactions with living cells.

6. Microwave torch (A, b) [21]. This new microwave device has been constructed at the Max Planck Institute in Garching, Germany, and tested on patients in the Munich Hospital. The microwave source at 2.45 GHz and 100 W (Figure 4) is operated in flowing argon (3 l/min). Like in the APGD-t, downstream injection of other gases is possible. Operating on surfaces is performed using the downstream region (3 cm from the torch), where gas temperature is below 40℃. The major application of this source is wound healing and sterilisation.

7. Plasma pencil I (A, b, c) [22]. This is a plasma jet operated in argon. Driving voltage can be DC or AC, but usually it is RF at 13.56 MHz. Power consumption is 20-200 W, gas temperature depends on power, but usually it is quite high (> 300℃). This source can be also operated under water. Typical applications are cleaning and surface treatment.

8. Plasma pencil II (A, C, a, b) [23]. Plasma pencil is in principle a miniature jet with rather high gas flow (1-10 l/min). The difference from APGD-t and other jets is the electrode design and the voltage waveform. This source is driven by microsecond pulses with kV amplitude and repetition frequency of 1-10 kHz, the input power is 1-3 W. Gas temperature is close to room temperature. The intended applications lie in bacterial sterilisation and dentistry.

9. Plasma needle (A, C, a, b, c) [24]. Plasma needle is a simple device, consisting of a 13.56 MHz RF powered tungsten wire confined in a plastic tube (Figure 5.4). Feed gas is helium at a flow rate of 0.5-2 l/min, power input ranges from 10 mW to several Watts. Plasma needle generates a micro-plasma (0.1-2 mm glow size). In the 10-300 mW regime gas temperature is about the same as body temperature, above 1 W it can increase to 100℃ and more. It can be operated under water or internally in the body, using a specially constructed catheter. At present the needle is used for fundamental study of plasma interactions with living cells and ex vivo tissues, for surface functionalisation and for bacterial inactivation. The intended applications are: treatment of dental caries without drilling, tissue removal without inflammation,
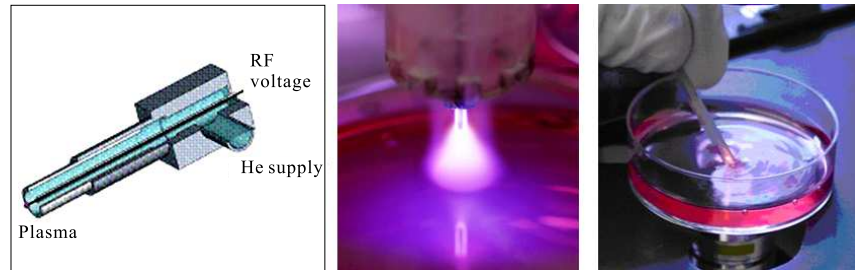
Figure 5.4: Plasma needle, a low-power radio-frequency atmospheric glow in helium. Left: a scheme of the device head, middle: a typical image of the glow, right: a new configuration to be operated under liquid (the plasma catheter, with membrane-closed head and helium recycling.)

treatment of skin diseases, ophthalmologic procedures (e.g. treatment of corneal ulceration, re-canalisation of lachrymal canal), and treatment of cardiovascular diseases (atherosclerosis).

10. Array of micro-plasmas (A, B, C, a, b). This relatively new way of cold plasma generation will be the subject of this chapter. The main aim is to generate a cold plasma with a large area and a reasonable degree of uniformity. Such a discharge has many potential applications is surface processing as well as in health care, food safety, etc. In fact, plasma arrays may be complementary to micro-plasmas in applications that require fast and homogeneous treatment of large surfaces. One might think about disinfection of large-area wounds (burns), cleaning of hands before entering the operation theatre, improving safety of fresh food products, and many others. The basic cooling principle is the same as in case of micro-plasmas: small size (thus large surface to volume ratio), usage of noble gases and convective cooling. The current design incorporates the principle of DBD (barrier discharge), but it evades the major drawback of DBDs, which is a small electrode gap. The details are given in the next section.

5.2 Summary of recently published results on DBD atmospheric helium discharges

Several groups have investigated the characteristics of a Helium Dielectric Surface Barrier Discharge at Atmospheric Pressure in the presence of nitrogen and water vapor from air in detail, both experimentally and theoretically.

5.2.1 Results by Foest and Golubovskii

It is found that the characteristics of atmospheric discharges in helium are strongly affected by contaminating species. Small quantities of nitrogen can change the characteristics from filamentary to a glow discharge. The species and their energy levels involved in so-called "non- hermetic" atmospheric systems, showing the effect of small quantities of nitrogen, is given by the figure 5.5 [25].

It is found that in addition to the direct ionization of helium at 24.6 eV, there is the
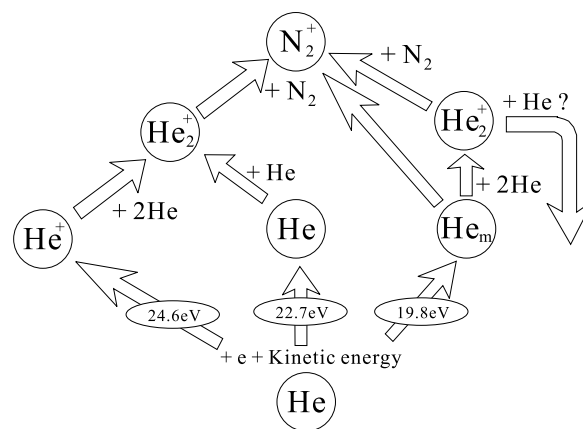
Figure 5.5: Diagram of the species and their energy levels involved in atmospheric systems of helium with impurity of nitrogen reported by Foest et al. [25].

Hornbeck-Molnar process, i.e., the ionisation by collision of highly excited states with helium atoms. This is found to be the most effective Penning ionisation. At high pressure, the conversion of ions causes the formation of N_2^+ ions within a time of 0.1 μs.

When the ionisation scheme shown in the figure 5.5 would be valid for such a non-hermetic system, then the excitation of meta-stable helium would be followed by ion formation with almost 100% efficiency. Foest et al., however, found that this is not the case at all [25]. Therefore they had to assume that an unknown additional mechanism results in the effective destruction of the helium meta-stable states. Because OH formation in a helium discharge, with nitrogen species present, is very effective at one atmosphere, we stipulate that this is the missing link in the diagram given by Foest.

For pure nitrogen gas Golubovski et al. considered the influence of two other effects: photo- electron emission and "electret" electron emission from mylar in a DBD with pure nitrogen gas [26].

Golubovski et al found a very strong effect of the electrode material on the uniformity of the DBD with pure nitrogen (7 kHz). They find that so-called electret materials like Teflon and PET are particularly effective in allowing a very large gap length. They hypothesize that this is the result of the creation of seed electrons, slowly emitted from these materials, with a decay time much longer than the lifetime of metastables.

Golubovski showed that in the presence of photoemission and in the absence of any other emission processes, even one incident electron might ignite a quasi-homogeneous glow discharge covering all the electrode area. They assume that at low frequencies, this effect may be the origin of the homogeneous glow barrier discharge.

5.2.2   Theoretical Model of Zhang & Kortshagen for He Glow discharge with 20 ppm nitrogen

Due to small leaks in real experimental systems, nitrogen impurities affect the properties of an atmospheric helium discharge. Strong nitrogen emission was reported earlier for a helium discharge in [27]. In order to quantify the effect of nitrogen, Zhang & Kortshagen (abbreviated below as Z&K) modeled a pure atmospheric helium discharge with 20 ppm of N_2 contamination.

Z&K have shown that in an atmospheric helium discharge, Penning ionization of nitrogen contamination is the dominant ionization mechanism in the discharge [28].

It leads to an elevated pre-ionization level before the discharge pulse that is essential for maintaining a uniform discharge. Increasing the driving frequency favors a transition from a filamentary to a uniform glow discharge. An increasing number of filaments with driving frequency are observed. They find that at a sufficiently high frequency the filaments in a helium discharge with 20 ppm of nitrogen coalesce, leading to a uniform discharge. Unfortunately their model does not include the effect of water vapor.

Z&K considered the following species in their model: electrons, atomic and molecular helium ions (He^+ and He_2^+), helium metastables (He^*), and nitrogen ions (N_2^+). The helium excited states of 2^3S and 2^1S were lumped into one single state He^* for simplicity.

A secondary electron emission coefficient for helium ions on the Al_2O_3 surface of γ_{sec} = 0.1 was assumed, which was adjusted to match the experimentally observed breakdown voltages.

For the structure analyzed by Z&K, in all cases, a sinusoidal ac voltage was applied. The thickness of the alumina dielectrics covering the electrodes was d = 1.5 mm with a relative permittivity $\varepsilon = 9$. The electrodes were 1.5mm thick, and the gap distance used was L = 5 mm. The electrodes had a diameter of 4 cm. The amplitude of the voltage was fixed at $V_{appl} = 1.5\,\text{kV}$; the driving frequency was varied. The reaction rates were assumed

according to table 5.1:

<div align="center">**Table 5.1:**</div>

Process	Notation	Rate coefficient	Reference
Direct ionization	$He + e \rightarrow He^+ + 2e$	α_1	[29]
	$N_2 + e \rightarrow N_2^+ + 2e$	α_2	[29]
Excitation	$He + e \rightarrow He^* + e$	from Bolzmann solver	
He^+ conversion	$He^+ + 2He \rightarrow He_2^+ + He$	$1.5 \cdot 10^{-31}[cm^6 s^{-1}]$	[30]
Stepwise ionization	$He^* + He^* \rightarrow He^+ + He + e$	$8.7 \cdot 10^{-10}[cm^3 s^{-1}]$	[30]
	$He^* + He^* \rightarrow He_2^+ + e$	$2.03 \cdot 10^{-9}[cm^3 s^{-1}]$	[30]
De-excitation	$He^* + e \rightarrow He + e$	$2.9 \cdot 10^{-9}[cm^3 s^{-1}]$	[30]
Penning ionization	$He^* + N_2 \rightarrow He + N_2^+ + e$	$7.6 \cdot 10^{-11}[cm^3 s^{-1}]$	[30]
	$He^* + N_2 + He \rightarrow 2He + N_2^+ + e$	$3.3 \cdot 10^{-30}[cm^6 s^{-1}]$	[30]
Charge transfer	$He_2^+ + N_2 \rightarrow N_2^+ + 2He$	$1.1 \cdot 10^{-9}[cm^3 s^{-1}]$	[30]
	$He_2^+ + N_2 + He \rightarrow N_2^+ + 3He$	$1.1 \cdot 10^{-9}[cm^3 s^{-1}]$	[30]
Recombination	$He^+ + e + e \rightarrow He + e$	$8.0 \cdot (T_g/T_e)^4[cm^6 s^{-1}]$	[30]
	$He_2^+ + e \rightarrow 2He$	$9.0 \cdot 10^{-9}[cm^3 s^{-1}]$	[30]
	$N_2^+ + e \rightarrow 2N$	$2.0 \cdot 10^{-7}[cm^3 s^{-1}]$	[30]

Z&K calculated that the build-up of the helium meta-stable density leads to an increase of the Penning ionization rate of nitrogen, which peaks about 2.5 μs after the He excitation and ionization peak. This result is qualitatively consistent with the delay between HeI emission and N_2^+ emission observed experimentally in [27].

Therefore it is to be expected that for an applied voltage with a frequency of 100 kHz or less, the effect of N_2^+ might play an important role. Due to the long lifetime of helium meta-stables the production of N_2^+ continues long into the afterglow phase of the current pulse, leading to a high density of N_2^+ ions in the afterglow until right before the next breakdown of the discharge. It is reasonable to expect that the presence of N_2^+ will have a significant impact on the breakdown and the uniformity of the Atmospheric pressure glow (APG), since it strongly affects the density of charge carriers at the beginning of the next breakdown. The Penning ionisation of nitrogen impurities leads to a higher effective ionisation coefficient at relatively low electric fields compared to a pristine helium discharge. Consequently, Z&K observe a decrease of the breakdown voltage required for the ignition of the discharge. In fact, no breakdown occurs in the simulation for the case above
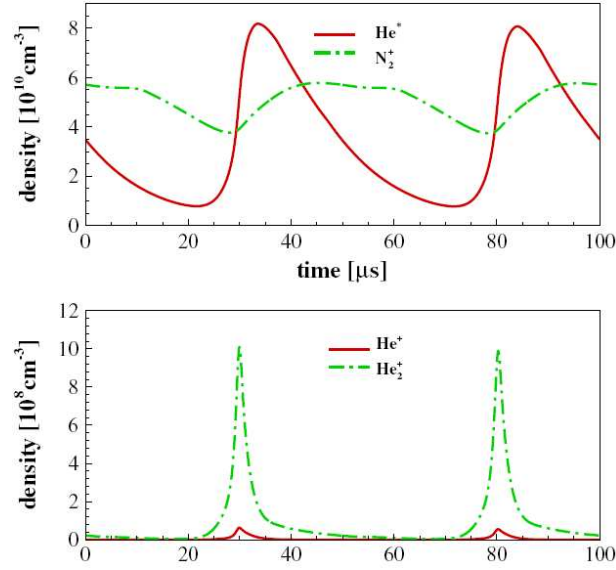
Figure 5.6: Calculated density of the different species in an atmospheric helium discharge with 20ppm of nitrogen added reported by Zhang and Kortshangen [28].

without the addition of nitrogen impurities. Furthermore, Penning ionisation can also elevate the pre-ionisation level at a lower electric field, which is believed to be an essential condition for obtaining the glow discharge at atmospheric pressure [15]. The effective overlapping of a large number of avalanches induced by the increased "seed" electron density is an important mechanism for reducing the transverse non-uniformity and for leading to a homogeneous glow discharge at atmospheric pressure [14].

The higher frequency case (25 kHz, and $\varepsilon_r = 9.0$) shows a typical DC type glow discharge structure, with a high electric field in a narrow cathode layer and a relative low electric field in a distinct positive column. The helium meta-stable production rate has a similar structure, following the behavior of the electric field.

The influence of nitrogen impurities manifests itself in Penning ionization of N_2 through collisions with metastables. It is much more important than charge exchange between helium and nitrogen; also direct ionization of nitrogen was found to be insignificant. The line-averaged species density shows that for a helium discharge with only 20 ppm nitrogen impurities, nitrogen molecular ions are the dominant ion species.

The Penning ionization not only decreases the gap breakdown voltage, but also increases the pre-ionization level, which is essential for maintaining a uniform glow discharge at atmospheric pressure. Helium and neon meta-stables have an excitation energy of 20 eV and 16.6 eV, respectively and they have enough energy to ionize nitrogen directly (ionisation energy, 15.6 eV), but argon metastables do not (11.6 eV).

Not surprisingly Z&K find that the dominant ionic species is N_2^+. The helium meta-stable production has only one peak, which is located inside the cathode layer. Below 20 ppm the dominant species for priming of the discharge however is N_2^+ produced.
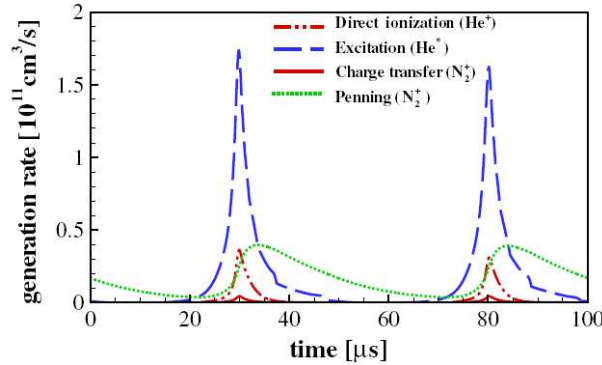
Figure 5.7: The line averaged generation rate for the different species in the Atmospheric Pressure Glow Discharge (APG) for $V_{appl} = 1.5kV$, f = 20 kHz, 20 ppm nitrogen reported by Zhang and Kortshangen [28].

Figure 5.7 shows the He^* meta-stable production in the presence of 20 ppm nitrogen, and also the much longer lasting production of the N_2^+ particles, reducing the breakdown voltage. The half-lifetime of the He^* particles as calculated by Z&K is about 20 μs, and therefore helium metastables are expected to be only effective at frequencies substantially higher than 10 kHz. Below 10 kHz however the only priming particles that are effective, are the N_2^+ particles, generated through the Penning effect. These calculations however assume that there is no other mechanism that reduces the lifetime of the helium metastables, contrary to the observations by Foest et al. [25].

5.2.3 Experimental results by Navratil et al on an atmospheric pressure helium and neon discharge in the presence of air

Navratil et al investigated experimentally the discharge properties at one atmosphere of both helium and neon [31]. They used a discharge structure, where the discharges were generated between two metal electrodes, both covered by an alumina layer and driven by an AC voltage at a frequency 10 kHz. The discharge gap used was was 2.2 mm and 5 mm, respectively. The current was monitored by measuring the voltage across a 100 Ω resistor, connected in series with the discharge cell.

Navratil also calculated the memory voltage transferred by the externally applied volt-

age onto the surface of the Al_2O_3 dielectric. The method used, to determine the wall voltage, described in their paper, was originally developed by Massines et al [15].

The gap voltage V_g and the memory voltage (or "wall-voltage") V_m were calculated from the applied voltage V_{appl} and the current I, by using equations (5.1) and (5.2), as described by Massines et al [15] :

$$V_{appl}(t) = V_g(t) + V_m(t) \tag{5.1}$$

$$V_m(t) = V_m(t_0) + \frac{1}{C_d} \int_{t_0}^{t} I(t')dt' \tag{5.2}$$

Here $V_{appl}(t)$ is the applied voltage, I(t) the measured current and C_d the effective capacitance of the dielectric layer. $V_m(t_0)$ is the initial memory voltage across the dielectric, which was adjusted in order to obtain the symmetrical evolution of the gap voltage (i.e. V_g (average) = 0).
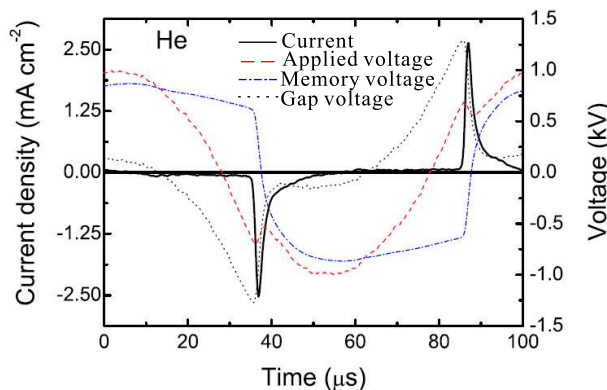
Figure 5.8: The calculation results for the gap voltage, memory voltage and applied voltage etc. reported by Navratil et al for an atmospheric discharge in helium. [31].

Navratil et al kept the value of the applied voltage close to the breakdown voltage, so that a single current peak per voltage half period is observed; the discharge operates in the so-called single peak mode (SPM).

Instead of calculating the memory voltage from the current, it can also be measured more directly using a capacitor in series with the discharge cell, instead of a series resistor. The voltage across the capacitor is then plotted as a function of the applied voltage, as described in Appendix A.2.

Navratil et al find that, besides N_2 emission of the second positive system, there is a strong OH emission in both neon and helium discharges (see figure 5.9 and figure 5.10).

The spectrum for neon shows, in addition to the line spectra, also a continuum of emission, with a (broad) maximum at about 280 nm. This phenomenon so far is unexplained.
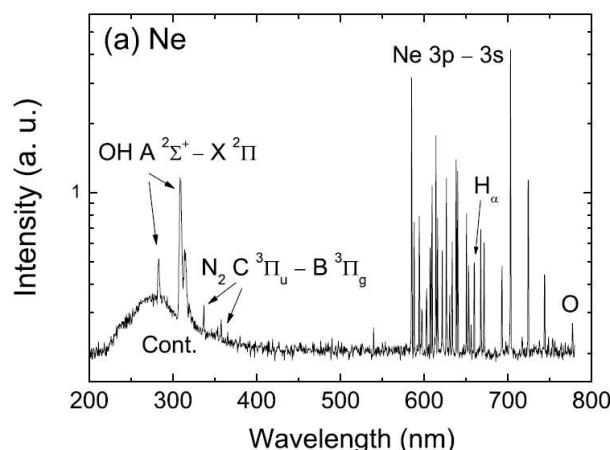
Figure 5.9: The typical neon spectrum of uniform glow discharge in a DBD in Single Pulse Mode reported by Navratil et al [31].

The decay of the intensity with time of the different emission lines in case of helium, as found by Navratil is shown in figure 5.11.

The intensity dependences of impurity emissions denote the role of meta-stables as in the case of the neon discharge.

Quite peculiar is the development of OH, the intensity of which increases faster than the discharge current (only for helium; not for neon).

In the case of helium (see figure 5.11), the same helium line at 707 nm was measured twice, at the beginning as the first measured line and then later after the measurement of other emissions (N_2^+, OH and He), in order to test the discharge stability and the reproducibility of the presented results. These two temporal dependences differ only slightly, and their maxima are as sharp as those of the neon lines. Consequently, helium is excited by the electron impact.

Navratil et al conclude that the observed time development with a CCD camera is in agreement with the Townsend mechanism of the discharge breakdown, which presumes the discharge sustenance by secondary electrons being created by ion bombardment of the cathode and by photo- ionisation.

5.2.4   The effect of water - OH-Emission (Ricard, Anakin)

The radiation of 309 nm OH emission in the afterglow in helium was explained already in 1999 by by Ricard et al [32].

Ricard et al considered the production of the radiative states OH(A) by the following
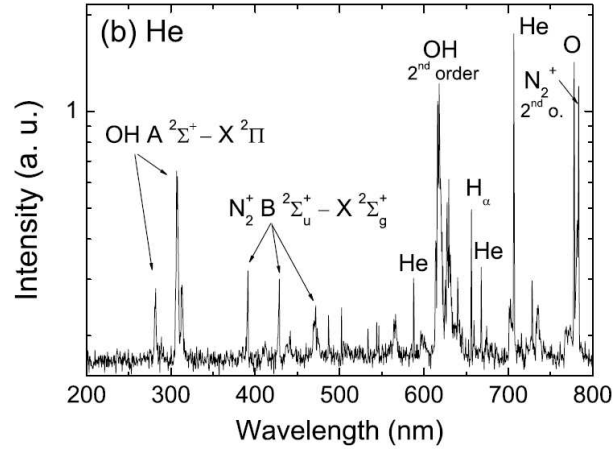
Figure 5.10: Helium emission spectrum of the uniform glow discharge in a DBD in Single Pulse Mode reported by Navratil et al [31].

rections:

$$He(2s^3S) + H_2O \rightarrow He + H_2O^+(X, A, B) + e \tag{5.3}$$

$$He(2s^3S) + 2He \rightarrow He_2(a) + He \tag{5.4}$$

$$He_2(a) + H_2O \rightarrow 2He + H_2O^+(X, A, B) + e \tag{5.5}$$

$$H_2O^+(A) + e \rightarrow OH(A) + H \tag{5.6}$$

$$OH(A) \rightarrow OH(X) + h\nu \tag{5.7}$$
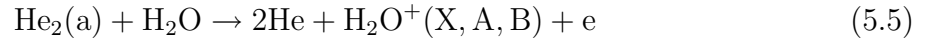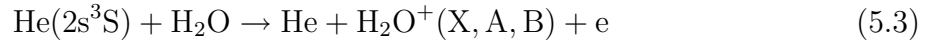
It was pointed out however by Anikin et al in their paper on a helium discharge (at 40 - 160 kPa with a nitrogen contamination corresponding to less than 0.8 kPa) that for a nitrogen level $p_{N2} < 10$Pa, the OH-radicals are produced by photo-dissociation of water molecules, by the active radiation in the wavelength range 70-100 nm stemming from the short living helium dimers

$$He^+ + 2He \rightarrow He_2^+ + He \tag{5.8}$$

$$He_2^+ + e \rightarrow He + He + h\nu \tag{5.9}$$

$$H_2O + h\nu \rightarrow OH(A) + H \tag{5.10}$$

In that case the emission intensity of the OH radicals depends in this case on the square of the helium pressure $(p_{He})^2$, and becomes very intense at one atmosphere.
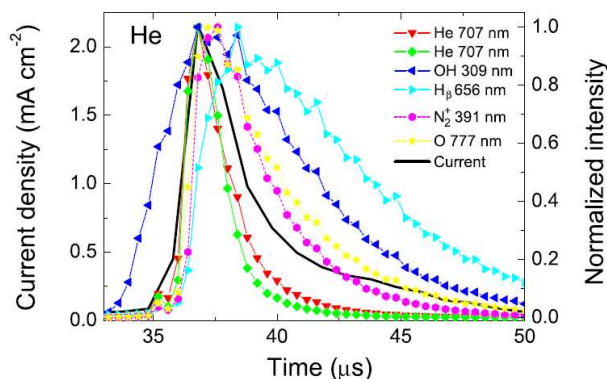
Figure 5.11: The temporal intensity development of various emissions of a helium discharge in comparison with the discharge current reported by Navratil et al [31].

5.2.5 Effect of oxygen on OH production

The effect of oxygen on the OH production in air and in argon has been investigated by Sankaranarayanan et al [33]. They performed laser-induced fluorescence measurements of OH radicals in a dielectric barrier discharge. The discharge was in a parallel plate geometry in atmospheric pressure air and argon. Although the air discharge consisted of discrete micro-discharges, two- dimensional images showed the spatial uniformity of the OH radical. Their results show that with increasing the power, the OH production decreases due to gas heating and increased ozone production.

Their conclusion is that the addition of O_2 increases the OH production at low concentrations; however, at higher O_2 concentration the OH concentration decreases due to increased electron attachment.

5.2.6 The effect of priming electrons on the discharge

A comparison of the energy levels of the meta-stable states of helium, neon and argon and the ionisation energy of N_2 supports the important role of indirect ionisation processes, e.g. Penning ionisation of N_2 molecules (equations (3) and (4)) as pointed out by different authors (e.g. Massines et al [15], Golubovskii et al [34]).

Navratil interestingly found that argon shows a filamentary DBD [31], when used under the same conditions as with helium and neon. The reason for this is said to be, that helium and neon metastables (with excitation energy of 20 eV and 16.6 eV, respectively) and He_2^* have enough energy to ionize nitrogen directly (ionization energy, 15.6 eV), but argon metastables do not (11.6 eV). Thus, in neon and helium the indirect ionisation of nitrogen may produce a preionization level, which is sufficient for an overlapping and a

coalescence of electron avalanches, as first proposed by Palmer [35] and by Levatter and Lin [36]. This avalanche coalescence leads to a suppression of the microdischarges and to the generation of the diffuse regime of the DBD.

5.2.7 Conclusions from the recently published results on DBD atmospheric helium discharges

From the published results on DBD type helium discharges, it is clear that at one atmospheric only the effect of nitrogen on the DBD helium discharge has been described in sufficient detail. The formation of N_2^+ ions by helium metasables through Penning ionization is the dominant effect. Foest however noticed that in real systems, too many helium metastables were lost by an unknown factor. The effect of water vapor, always present in non-baked non-hermetic systems, and the formation of OH radicals, was described by Navratil for DBD type of discharges. However, no spectral emission results of a surface barrier discharge system with helium have been found in the literature.

5.3 Design of a Micro Plasma Array Plate and Experimental setup

5.3.1 Experiment Setup

Figure 5.12 shows the experimental set-up used in order to ignite the plasma above the Micro Plasma Array Plate (MPAP). A quartz window is mounted in front of the plasma plate, at a distance of 15 mm allowing a continuous gas flow, and the analysis of the spectral properties of the gas discharge in the range of 200-850 nm.

5.3.2 Plate design

The plate design used for this study is identical to that used as a Plasma Display Panel (PDP), except that Al_2O_3 is used as a protective layer instead of MgO. The use of MgO is not very practical for an atmospheric discharge, because MgO easily reacts at room temperature with both H_2O and CO_2 from the air, requiring high temperatures for the desorption.

Figure 5.13 shows the cell design of the Micro Plasma Plate. To create a discharge on the surface of the Al_2O_3 layer, a voltage is applied to the external terminals X and Y of
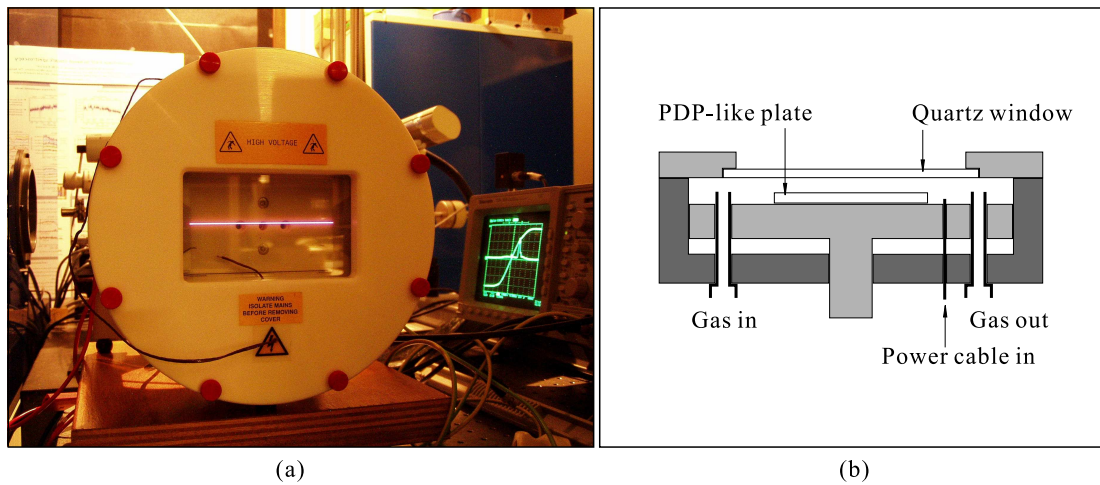
(a)   (b)

Figure 5.12: Plate support and gas supply. a) is the photo of the setup; b) is the design of the setup.

the plate, alternating between a positive and negative value, at a frequency of typically 100 kHz, sustaining the generation of discharge pulses.

The structure of the plasma plate we used in our setup is shown in figure 5.14. The etched Indium Tin Oxide (ITO) pattern forms the electrodes; an inner gap d of 70 μm is formed between each pair of ITO electrodes; the outer gap separating this pair with the adjacent electrodes is wide enough to avoid vertical "cross-talk". Each ITO electrode is partially covered by an aluminium electrode of 80 μm width, in order to reduce the resistance and allow external biasing. A dedicated micro-plasma array source might be constructed in the future using only aluminium as electrodes, without the need for ITO. The specially shaped terminals are designed to match the electrode pitch to that of flexible foils to connect the electrodes to the power supply. A dielectric layer of 30 μm thickness covers the electrode structure, and finally an Al_2O_3 layer is deposited on top of the plate by sputter deposition in argon (the pressure of Ar filled in chamber was about 10^{-2} mbar of argon, after pumping the chamber to 10^{-6} mbar). The dielectric constant of the dielectric barrier layer is about 12, so that the capacitance between the electrodes and the plasma is of the order of 0.3 nF/cm^2 of electrode area used to generate the plasma. The pitch between the electrode pairs is 1080 μm, as used in a 42-inch PDP; the effective ITO electrode area for a single line pair of is about 1 cm^2. The design of the terminal pads is critical and a conformal coating has to be used to avoid undesired discharges in that area.
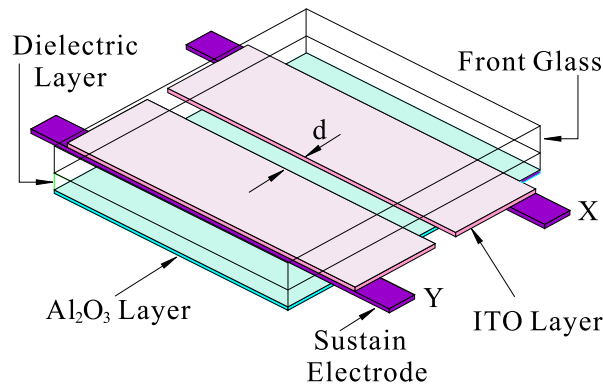
Figure 5.13: Cell design of the Micro Array Plasma Discharge Plate, showing the ITO gap, defining the discharge gap parameter d, covered by the transparent dielectric layer, and a Al$_2$O$_3$ layer.

5.3.3   Electrical Equivalent of the Plasma Plate and Biasing Scheme

The electrical equivalent circuit is shown in figure 5.15. The plasma is represented by either a capacitance C_p in case of no discharge, or by a short circuit, in case of a plasma discharge. C_d is a dielectric capacitance between each ITO electrode and the plasma; typically a dielectric capacitance value is 320pF/cm^2. C_{xy} is capacitance between the X and Y terminal also resulting from the dielectric. For a single line of discharges with 0.5cm^2 area per electrode, the approximate value for the dielectric capacitance per electrode is C_d = 160 pF, resulting in an effective capacitance of 80 pF, for the two capacitors in series, during the discharge.

5.3.4   Electrical Diagnostic Means

A shunt resistor of 100 kΩ is used to measure the applied voltage. The current waveform is measured, across a 500 Ω series resistor.

The applied voltage is a quasi-square wave pulse at a variable frequency from 10-100 kHz, by amplifying a square wave pulse. The rise time is about 1 μs, determined by the slew rate of the amplifier; the voltage waveform exhibits some overshoot, depending on the frequency.

Figure 5.17 shows the measured voltage and current waveforms for a single plasma line, at a voltage level where virtually the whole line was ignited and sustained.

At 50 mA peak current, the 500 Ω series resistor, gives some voltage loading effect during the plasma discharge, as can be seen from the dip in the voltage measured over the X-Y terminals. Using a 500 Ω resistor, the voltage drop is about 25 V. Lower values of the series
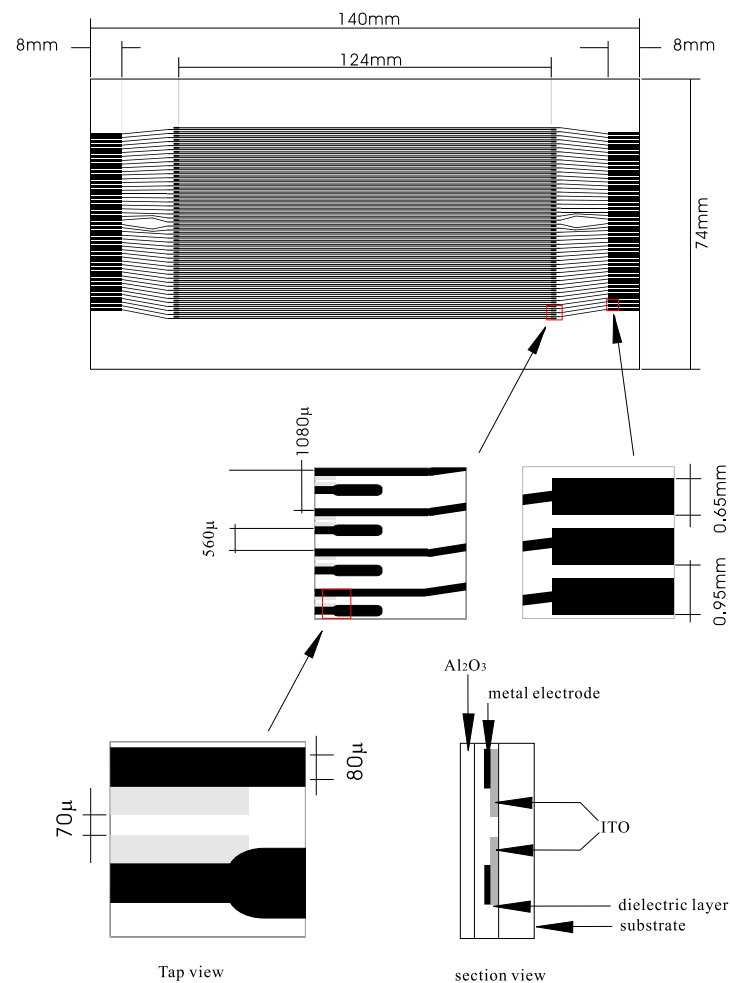
Figure 5.14: shows the design of a plasma plate used in this study to generate the array of micro-plasmas.

resistor were used to compare the impact on the light emission; the emission properties showed no qualitative differences, only the total amplitude was a little bit higher. Using a 50 Ω series resistor a voltage drop occurs of only 2.5 V (1%). As shown by Golubovskii et al however a low value of series resistance can induce instabilities (see section 4). We used 500 Ω also to reduce the measurement noise, in order to accurately determine the current waveform.

The value of the applied voltage at the moment of the initiation of the plasma current pulse, we call the "breakdown voltage" V_{BD} . The actual voltage across the helium gas, resulting in the plasma breakdown is of course different from this value. The voltage resulting from the memory charge, stored in the previous cycle on the surface of the Al_2O_3
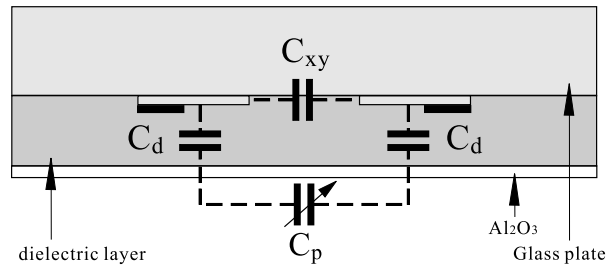
Figure 5.15: Electrical equivalent of a single line of the Micro Plasma Array Plate.
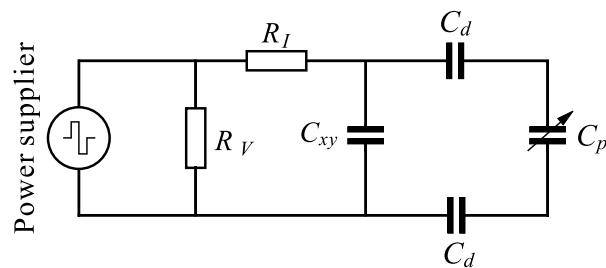
Figure 5.16: Biasing scheme for the Micro Plasma Array Plate.

layer, is in fact added to the externally measured V_{BD}, thereby sustaining the discharge. This memory voltage is calculated using formula (1.2). The applied voltage level needed to sustain the discharge $V_{applied}$(sus, min) assures the full development of this memory charge.

Figure 5.17 also shows the small displacement current, which is proportional to $C_{eff} \times dV/dt$, where C_{eff} is the effective dielectric capacitance between ITO electrodes and the plasma in case of no discharge (approximately equal to C_d). For the constant $350V/\mu s$ slope and the measured displacement current of near 5 mA. we find an effective capacitance of about $15 \cdot 10^{-12}$ Farad or 15pF, when there is no discharge.

In all cases tested, there was only a single current pulse, contrary to systems using a sinusoidal waveform, where multiple discharges can occur easily, due to the improper build-up of the charge on the MgO surface, called "wall-charge" in PDP jargon and "memory charge" in DBD jargon.

Figure 5.17 also shows the voltage across the helium gas; this voltage is also called the "gap- voltage", because it is the voltage across the gap formed above the Al_2O_3 surface; it has been calculated (for didactic purposes) using formula (1.1) and (1.2) by subtracting the memory voltage across the dielectric capacitance from the applied voltage. As can be
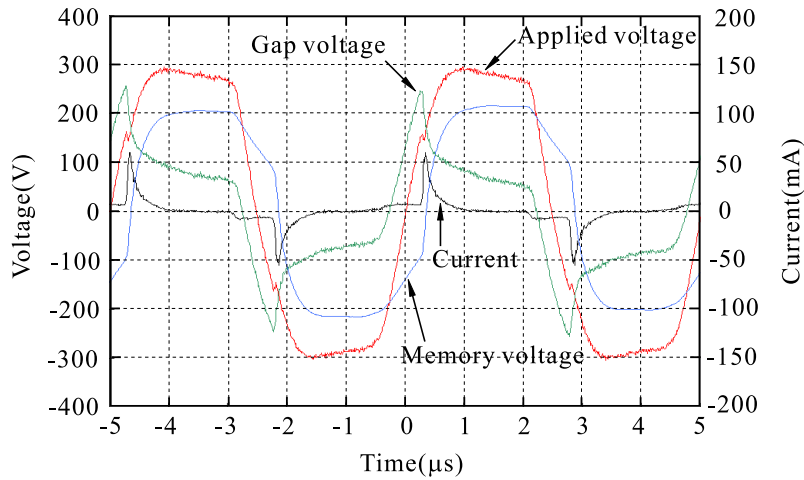
Figure 5.17: Externally applied voltage, resulting current and calculated memory voltage and gap voltage according to formulas (1.1) and (1.2) using the effective value of C_d=80 pF working frequency is 100 kHz and helium flow rate is 4 l/min

seen in figure 5.17 This gap voltage shows a maximum at the start of the plasma discharge current, and corresponds to the so-called "breakdown voltage" or "firing voltage" of the surface discharge. See e.g. Reference [31]

5.3.5 Design considerations for a future full panel biasing system

For the driving of a single line, as in our case, the peak discharge current for a single discharge line of 10 cm length in helium gas is of the order of 50 mA. In order to allow the use of all 48 lines in the small DBD plate, the peak current will increase to about 2 Ampere. At a sustain voltage of 300 V the average current in the panel is so high that the glass plate cracks at 100kHz. A similar situation occurs in a Plasma Display Panel during aging at full intensity, but in actual use the duty cycle is reduced. In our case we can improve the efficiency of the discharge in the future, by reducing the capacitance of the dielectric. This will be used in future designs dedicated to the generation of OH radical emission from atmospheric helium discharges.

For PDP operation a dielectric capacitance value of 0.3 nF/cm² is typically used. For atmospheric plasma generation this should be reduced to at least 0.1 nF/cm², enabling operation at 100 kHz without cracking the panel.

As the thickness of the dielectric layer should preferably not be increased, this value should be achieved by selecting a dielectric with a permittivity of about 4 instead of the currently used value of 12.

Instead of the voltage generator used in these experiments, a so-called "sustainer" should be used, identical to that used in a PDP, resulting in about 80% energy recovery. In such a sustainer the voltage is a full square wave, effectively created by "swinging" the voltage from +300 V to −300 V. With a sinusoidal generator this energy recovery of the displacement current is not possible. Therefore in this study all experiments are using a square waveform, simulating the PDP "sustainer" circuit, by using a voltage generator with a rise time of 0.65 μs, determined by the voltage generator.

5.3.6 Optical Diagnostic Means
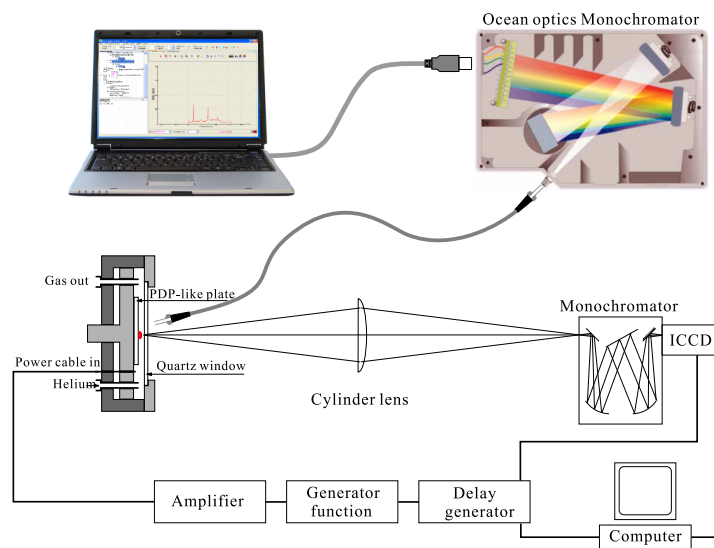
Figure 5.18: Optical measurement setup for the plasma emission from the micro plasma plage.

The spectral measurement system is shown in Figure 5.18. Two different monochromators were used for the plasma spectra measurement. For time-averaged spectral measurements we used an Ocean Optics H2000+ spectrometer, with two different gratings for the UV range and visible range, covering in total the range of 200-850 nm, This monochromator can only integrate the emission over a time much larger than the discharge cycle.

In order to measure the spectra with high temporal resolution, an ICCD (same as the ICCD introduced in chapter 4) combined with a monochromator (JOBIN YV H25) was employed for the measurement of the intensities of lines during the discharge. The system has a temporal resolution of 5 ns and the wavelength resolution can be 0.1 nm.

For the spectral measurements only a single line in the plate was ignited, as shown in figure 5.24. Another reason is that the panel temperature has to be kept close to room

temperature. We verified this by measuring the surface temperature using a thermocouple, which was removed for the actual measurements, as it disturbed the discharge.

(a)

(b)
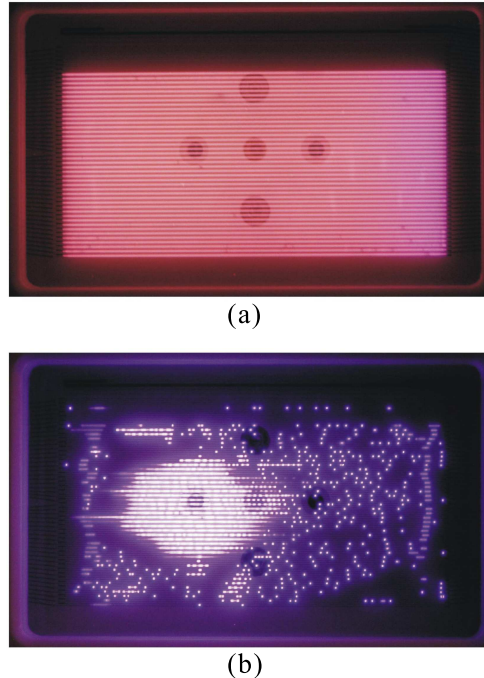
Figure 5.19: Plasma discharge patterns at 100kHz, two different helium flow rates. Top view: 4 l/min of helium; bottom view : 0.5 l/min of helium.

5.4 Single line atmospheric surface discharge

5.4.1 Discharge modes

Figure 5.19 shows the plasma discharge patterns at two different helium flow rates; the applied voltage was same in both cases. a) frequency:100 kHz, helium flow rate: 4 l/Min with a uniform discharge pattern, and the characteristic red 707 nm color from helium; b) frequency:100 kHz, helium flow rate: 0.5 l/Min showing irregular filamentary discharge with deep blue color from nitrogen (391 nm) (Note: the mounting holes of the supporting structure can be seen through the semi-transparent plate.)

Depending on the voltage that was applied we observe two distinct modes of discharge that we called the High voltage mode (figure 5.20a) and the Glow-mode (figure 5.20c).

At low voltage only a soft glow is excited, while at a higher voltage we see the development of a much higher intensity emission, gradually growing from one side of the panel,

while increasing the voltage (figure 5.20b).

(a)

(b)

(c)
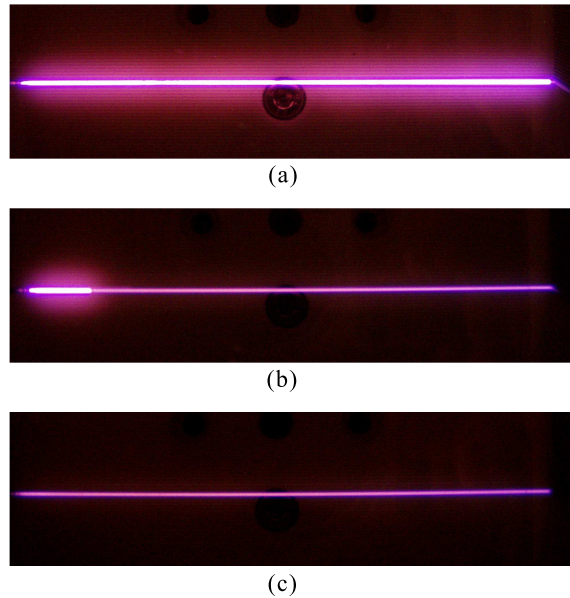
Figure 5.20: Single line emission at three levels of applied voltage: a) high voltage; b) intermediate voltage ; c) lowest voltage with fully ignited line plasma. The intensity as function of voltage is shown in figure 5.26

5.4.2 Flow rate and frequency dependance of the surface discharge breakdown voltage

Figure 5.21 shows both the applied sustain voltage and the applied voltage for which the helium plasma breakdown occurred, in a single line array of micro-discharges at one atmosphere of helium at low frequency. The applied voltage was made high enough so that the discharge properly sustained at each frequency. The measurements were made after aging of the Al_2O_3 surface, by applying a 10 kHz discharge for at least 30 minutes.

Figure 5.22 shows the breakdown voltage as a function of frequency for a high helium flow rate (4l/min). We observe that below 60 kHz there is an almost linear increase in breakdown voltage, while above 60kHz the breakdown voltage is constant at 150 V amplitude.

The increase in breakdown voltage at lower frequencies is associated with an increased delay time of the plasma breakdown, as shown in figure 5.23.

Figure 5.21: Applied voltage needed to sustain the discharge and breakdown voltage across the XY terminals at a frequency of 20 kHz.

We checked whether the increase in breakdown and the associated change in delay time for low frequencies could be the result of a different rate of voltage change, during ramp up/down, when changing the polarity of the applied sustain voltage. We found that for the driving system used, the change in dV/dt was negligible, and independent of the frequency.

5.4.3 Spectral characteristics $200-850$ nm

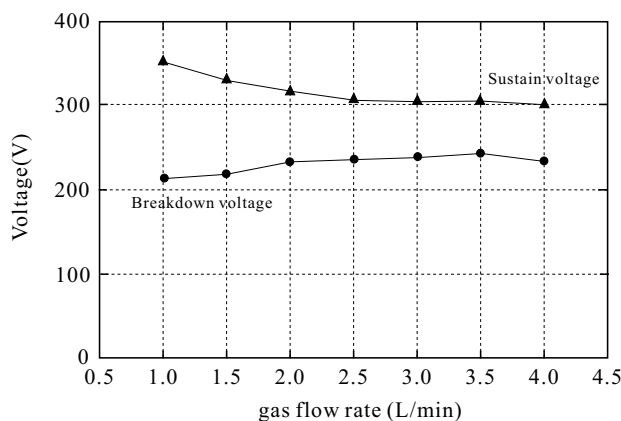The spectral emission from the Micro Plasma Array Plate, using helium gas at atmospheric pressure is shown in figure 5.24. The emission wavelengths and their origin are given in Table A.1 for the different species.

The dominant spectral lines emitted by the Micro Plasma Array Plate, using helium gas at atmospheric pressure, are found to be the 706 and 728 nm peaks of helium, but in addition very strong lines from the OH radical at 309 nm, and N_2^+ emission at 391 nm are found. All other lines are insignificant; especially remarkable is that almost no atomic nitrogen lines were detected.

The spectrum consists of almost the same lines as was observed in the plasma needle by I. Kieft (see figure 5.25) [39]. The plasma needle, as we mentioned in the introduction of this chapter, is a simple device, consisting of a 13.56 MHz RF powered tungsten wire confined in a plastic tube (Figure 5.4). Feed gas is helium at a flow rate of 0.5-2 l/min, power input ranges from 10 mW to several Watts. But the transition of OH at 309nm is the highest peak, also the transitions of OH (309 nm) and N_2^+ (391 nm) are even higher than the He (706 nm). The ratios of these two peaks to He (706 nm) are much larger than the Micro Plasma Array Plate case. Because the plasma generated by plasma needle is in a situation more open to the air, more N_2 and H_2O is involved in the discharge, and more
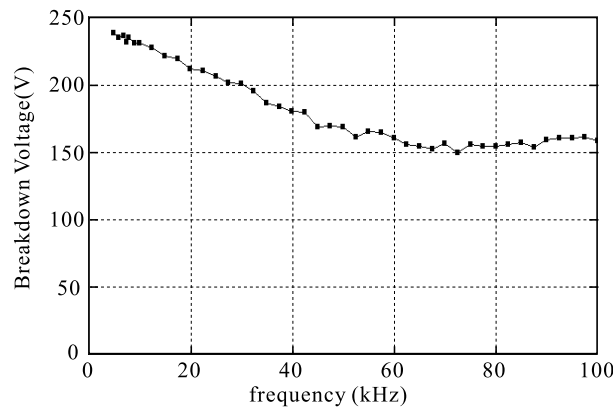
Figure 5.22: Surface discharge breakdown voltages in 1 atmosphere of helium as a function of frequency(helium flow rate: 4 l/min)

transitions related to N_2, N_2^+ found. It is understandable that the spectrum of plasma needle has a higher peak of OH 309nm and N_2^+ 391nm than the Micro Plasma Array Plate.

5.4.4 Glow mode versus high−voltage mode

Figure 5.26 shows the spectral intensities as a function of the applied sustain voltage. At a high voltage, a glow discharge from the full line can be observed at the full intensity above 330 V (figure 5.20a). When reducing voltage below 320 V, the intensity suddenly drops on one side of the panel (figure 5.20b), completely reducing to a soft glow mode (figure 5.20c)when further reducing the voltage. In the voltage mode above 330 V, the spectral intensity is independent of the applied voltage.

Figure 5.27 compares the spectra for the two modes; the intensity for the glow mode are magnified by a factor of about 20. In the High-Voltage mode the intensity of visible light emission (helium 706 nm and 728 nm) is about 20 times higher than in the low-Voltage Mode (see figure 5.26 for absolute comparison).

Both spectra show approximately the same ratio of OH-line to the 587 nm helium-line emission intensity. As can be seen from figure 5.27 the ratio of the N_2^+ peaks to the helium peaks (e.g. 587 nm) however is different. In the helium glow mode the 391 nm and 427 nm N_2^+ lines are relatively strong, while in the high voltage mode they are relatively reduced.

5.4.5 Dynamics of the OH and N_2^+ emission lines

The dynamical processes of He^+, N_2^+ and OH generation were investigated using an ICCD camera. Figure 5.28 shows the development over time of the emission lines, for He (706
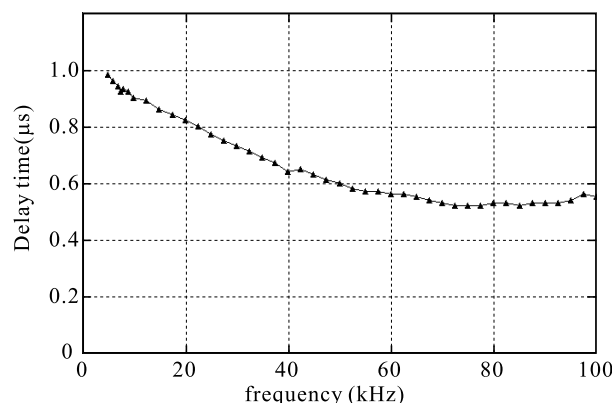
Figure 5.23: Time delay between plasma breakdown and applied sustain voltage as a function of frequency for flow rate of $4l/min$ of helium.

nm), N_2^+ (427 nm) and OH (309 nm), compared to the plasma current buildup.

The plasma current pulse rises very steeply and decays in approximately 150 ns. The helium 706 nm light intensity over time is almost proportional to that of the current pulse. For the N_2^+ line (427 nm) there is a 50 ns delay between the rising edges compared to that of helium line (706 nm). After reaching its highest level, the N_2^+ intensity drops to a $1/e$ level within about 400 ns.

It is only then, that the OH (309 nm) intensity starts to increase significantly, reaching its highest point even later than the end of current pulse. The lifetime of the OH line is also much longer; it has a lifetime of about 1200 ns.

5.4.6   Effect of flow rate

The helium flow rate was changed from 1 l/min to 4 l/min of helium; the resulting spectra for 1 and for 4 l/min are shown in figure 5.29.

At 4 l/min helium of flow the intensity of the OH (309 nm) peak increases with respect to the He (706 nm), while N_2^+ (391 nm) drops dramatically, and the other nitrogen emission lines are very low.

In figure 5.30 we plot the spectrum line emission intensities as a function of the atmospheric helium flow rate. We see that the OH intensity increases almost linearly with the helium flow rate, and then saturates above 3 l/min helium flow rate. At the same time we observe a dramatic reduction of the N_2^+ line emission.
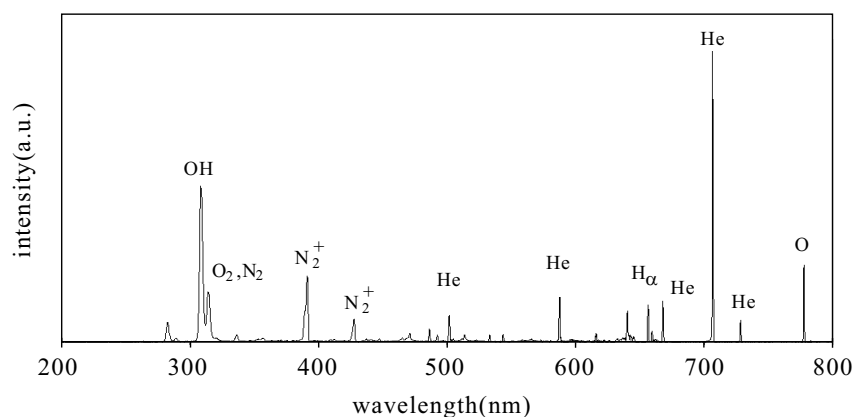
Figure 5.24: Emission spectra of the Micro Plasma Array Plate measured at 4 l/Min helium gas flow at atmospheric pressure and an Al_2O_3 electrode surface.
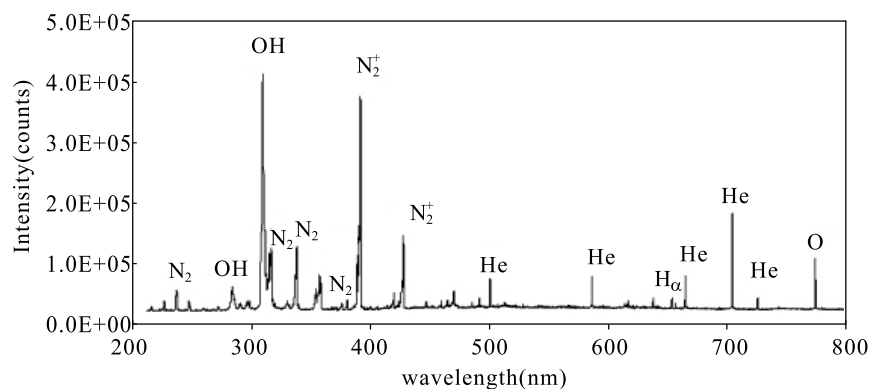
Figure 5.25: Emission spectrum for plasma needle. Emission lines were ascribed to He, N_2, N_2^+, OH^* and O^*.

5.4.7 Effect of time

The applied voltage needed to sustain the discharge and the actual externally measured breakdown voltage, is quite stable at 20kHz or lower frequencies, as shown in the figure 5.31.

At a much higher frequency, like 100 kHz, however the voltage needed to sustain the discharge continuously increased with time during 1 hour, while the breakdown voltage was reduced, as shown in figure 5.32.

Detailed investigation requires further study of this phenomenon, especially focusing on the physical and chemical effects occurring at the Al_2O_3 surface under helium plasma excitation. However, this goes beyond the present investigations of the basic behavior of a

Table 5.2: information of species and transition of lines in helium atmospheric discharge.

Excited species	Wavelength(nm)	Transition	References
OH	309	$OH(A^2\Sigma^+ \to X^2\Pi)$	[37]
N_2	316	$N_2(C^3\Pi_u \to B^3\Pi_g)$	[38]
N_2	337	$N_2(C^3\Pi_u \to B^3\Pi_g)$	[38]
N_2	358	$N_2(C^3\Pi_u \to B^3\Pi_g)$	[38]
N_2	380	$N_2(C^3\Pi_u \to B^3\Pi_g)$	[38]
N_2^+	391	$N_2^+(B^2\sum_u^+ \to X^2\Sigma_g^+)$	[38]
N_2^+	427	$N_2^+(B^2\sum_u^+ \to X^2\Sigma_g^+))$	[38]
He	501	$3^1P \to 3^3D$	[20]
He	587	$3^1P \to 3^3D$	[20]
He	667	$3^1P \to 3^3D$	[20]
He	706	$3^1P \to 3^3D$	[20]
He	728	$3^1P \to 3^3D$	[20]
O	777	$3^1P \to 3^3D$	[20]
H_α	656	$n = 3 \to n = 2$	[20]

one atmosphere helium surface discharge.

In this study we determined the change in intensity of the major spectra over the 1-hour period, as shown in figures 5.33. The spectral lines are shown in two groups. The first group shows a continuous increase in intensity, while the second group exhibits an initial decrease in intensity. In order to be able to work with a single grating during the measurements, the major helium 706nm line was not measured; instead the 502 and 587 nm helium lines are shown.

From these results we conclude that initially both the He and N_2 lines are reduced during the first 20 minutes, while both the OH and N_2^+ lines rapidly grow. After that that, all spectral lines, continue to increase rapidly, showing some saturation after 1 hour.
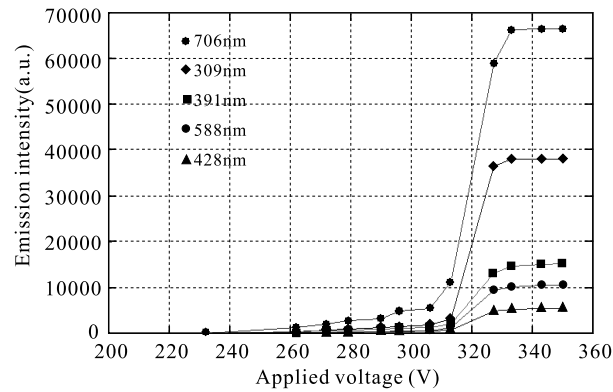
Figure 5.26: Spectral emission of the single line micro plasma plate as a function of the applied sustain voltage (100 kHz, 4 l/min of helium).
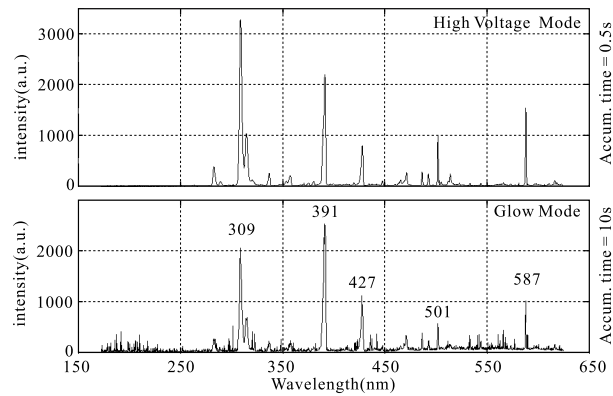
Figure 5.27: Spectral emission distributions for the single line array of micro plasmas in helium (4 l/min); glow mode intensities x10.

5.5 Discussion on the characteristics of the Plasma Array Surface Discharge

5.5.1 OH emission intensity

The most intense spectral line that we found in the Micro-Array Plasma Plate is that of the OH radical. It is one of the best oxidant agents that is known, and therefore of great interest. Also the 309nm radiation from OH is of great interest for medical treatment of e.g. psoriasis. As was pointed out by Anikin et al in their paper (see section 5.2.4), at very low levels of nitrogen ($p_{N_2} < 10$Pa), that is at high flow rates of helium in our setup, the OH-radicals are produced by photo-dissociation of water molecules by the active radiation
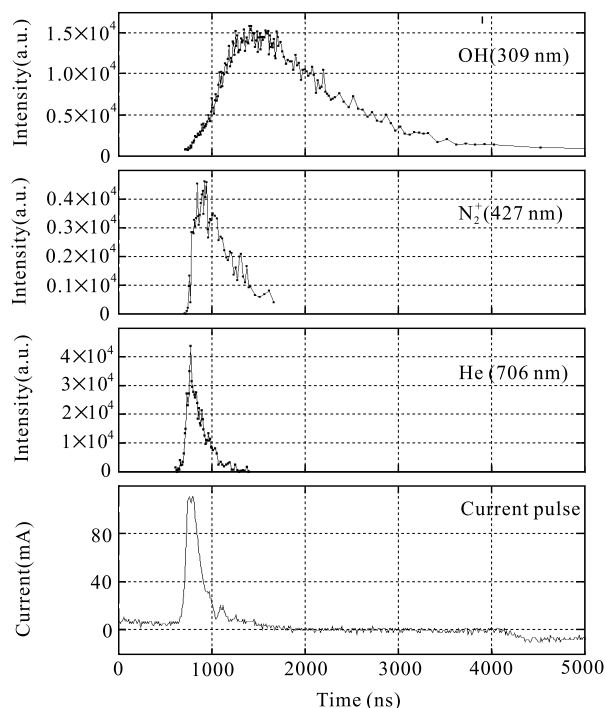
Figure 5.28: Development of the intensity of the helium (706 nm), the N_2^+ (427 nm) and the OH(309 nm) line intensity and the plasma current waveform versus time (from top to bottom) for a single line of the Micro Plasma array in helium at atmospheric pressure using a sustain frequency of 100 kHz and helium flow rate of 4 l/min.

in the wavelength range 70-100 nm stemming from the short living helium dimers.

From figure 5.30 we see that the OH intensity increases almost linearly with the helium flow rate, and then saturates above 3 l/min helium flow rate. At the same time we observe a dramatic reduction of the N_2^+ line emission. At 4 l/min helium flow the OH generation dominates, while at 1 l/min N_2^+ is the dominant emission process in our atmospheric plasma system.

From the reaction formula 5.8, 5.9 and 5.10 we saw that the emission intensity of the OH radicals depends on the square of the helium pressure (p_{He})2, probably explaining why at one atmosphere the OH emission is very strong.

In figure 5.28 we saw that the lifetime of the helium emission is very short. The excitation mechanism almost instantaneously follows the discharge current. The decay process is much slower, resulting in the observed decay time of more than 1 μs for the OH line emission.

The time dependant intensity profiles for helium, N_2^+ and OH are similar to those observed by Navratil et al. The most important difference is the value in lifetimes of the
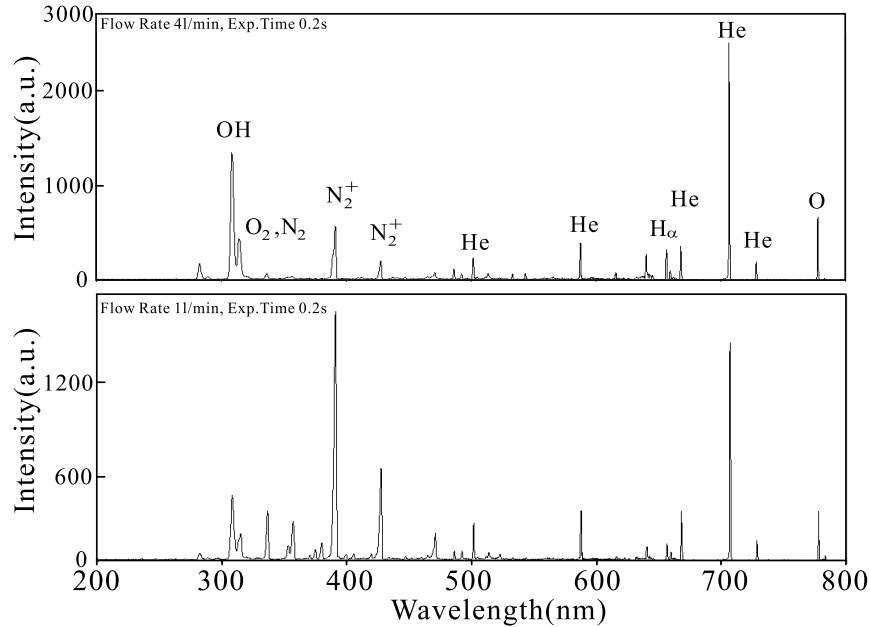
Figure 5.29: Effect of flow rate on the spectral emission of Micro Plasma Array in helium at 100 kHz. Top graph is for the flow rate of 4 l/min, bottom is for 1 l/min.

emission peaks. The current peak has a duration of only 150nsec, the N_2^+ of 400 ns and the OH intensity of 1200 ns, compared to 2000/4000/7000 μs respectively in the case of Navratil. Also we do not observe the anomalous early start of the OH intensity. Instead it starts only after the helium intensity is fully decayed. This might be caused by the long lifetime of OH($A^2\Sigma^2$)

We have to note that the pd values by Navratil were 25-60 times larger, while we operated much closer to the Paschen minimum voltage [40], using a pd value of about 10 Torr.cm (see appendix). Finally we used a dielectric capacitance value of 160 pF, instead of the capacitance of 6 pF used by Navratil et al.

5.5.2   Time dependent effects in the helium discharge

The OH intensity is directly related to the amount of water vapor in the system, therefore, it is clear that the time dependant effects that we have observed must be strongly related to the supply and desorption of water vapor from the surfaces inside our non-hermetic non-baked system.

After ignition of the discharge the temperature of the plate will gradually increase. At the same time the helium plasma will "clean" the Al_2O_3 surface by converting physically and chemically adsorbed water into OH. This will also affect the secondary electron emis-
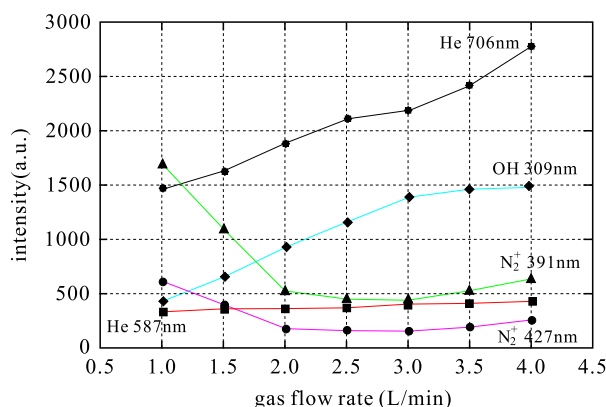
Figure 5.30: Spectral emission of the single line emission intensities as a function of the atmospheric helium flow rate.
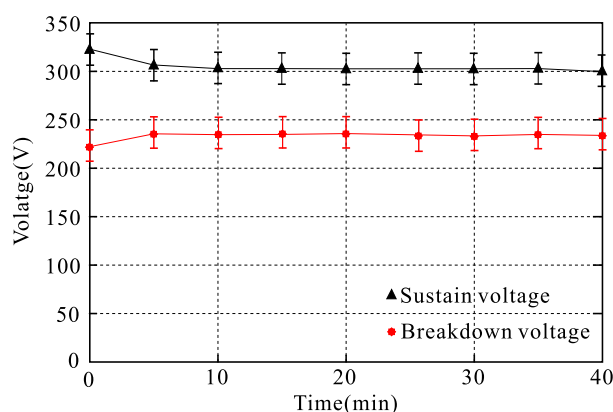
Figure 5.31: The applied voltage for minimum sustain and breakdown voltage as the function of time of plate working (working frequency: 20 kHz; gas flow rate: 4 l/min.).

sion coefficient of Al_2O_3 for helium ions. Finally the helium gas supplied also contain some water vapor.

The temperature of the plate was measured during operation, with helium flowing at 4 l/min, at a distance of about 1 cm away from the single line discharge, the temperature increase was only a few degrees Celsius higher than room temperature, but in the future in situ measurement is needed.

The details of the different mechanisms requires further study, where a controlled level of water vapor and plate temperature, should be used to quantify these different effects.
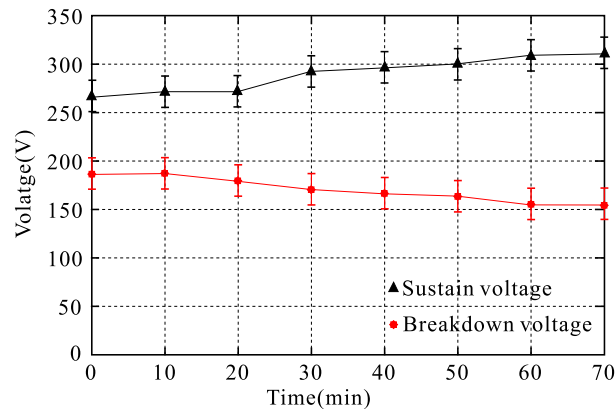
Figure 5.32: The applied voltage for minimum sustain and breakdown voltage as the function of time of plate working (working frequency: 100 kHz; gas flow rate: 4 l/min.)

5.5.3 Frequency dependent effects

The priming effect of helium meta-stables in the presence of N_2

After reversal of the externally applied voltage, the memory charge reduces the value of minimum voltage needed to sustain the discharge. This is only true however as long as there are sufficient priming electrons to re-ignite the discharge.

Penning ionization of nitrogen appears to be the most important source of priming electrons in a helium gas with nitrogen contamination present (see reference [28], and table 5.1).

If the meta-stable lifetime becomes too short, compared to the time between two reversals of the applied voltage, then the number of priming particles will also become smaller, and the minimum sustain voltage will increase. From figure 5.6, we see that (in the absence of water vapor) the He* lifetime is such that the density of meta-stables is significantly reduced after about 50 μs. It is however difficult to determine the lifetime of all the helium meta-stables valid for our conditions, where both water vapor and nitrogen is present. The value of 50 μs would correspond to one half period of a 10 kHz sustain frequency; at that frequency the sustain voltage would be expected to be significantly higher than at e.g. 100 kHz.

However, when we reduced the sustain frequency from 100 kHz down to 10 kHz we did not find a significant increase in sustain voltage; on the contrary, it is virtually constant. But we do see a linear increase in the value of the breakdown voltage, below a frequency of 60 kHz. (see figure 5.22)
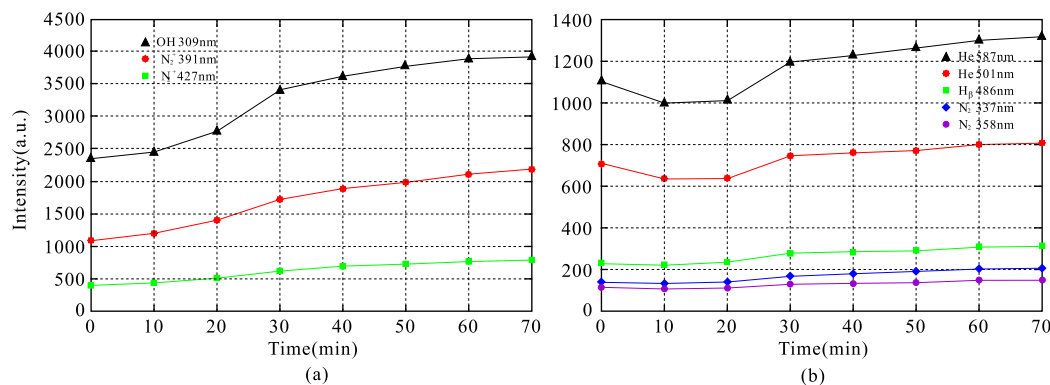
Figure 5.33: intensity change of the spectral lines for the 1 atmosphere helium plasma surface discharge (100 kHz, 4 l/min flow rate) on a Al_2O_3 surface as plate working time. (a) is for the lines of OH and N_2^+; (b) is the lines of He and N_2

5.5.4   Voltage dependent effects

The voltage dependant effects that we observed, are not well understood. Helium metastables have an energy of 20.0 eV, which is sufficiently high to generate electrons by the Penning ionization of nitrogen, for which 15.6 eV is needed. Thus, in helium the indirect ionisation of nitrogen may produce a preionization level. In a discharge at low voltage, the major source of electrons is through direct ionization of helium, resulting in the observed helium Glow Mode. At a higher voltage strong He_2 dimer emission [41] is generated by the discharge, dramatically increasing the OH formation by photo-dissociation, relative to that of N_2^+, as described in section 5.2.

5.5.5   Summary

In the present work, we are using a surface discharge with a thin dielectric, which differs from the standard DBD discharge systems studied by Zhang & Kortshagen (Z&K) and Navratil, in the following way (see table 1.3):

1. The pd value is 60 times smaller in our case, operating close to the Paschen minimum voltage value.

2. The capacitance per unit of area in our system is about 20-60 times higher.

3. The reduced field strength E/p is 10-25 times higher than for the case of Z&K and Navratil.

Table 5.3: Comparison of the discharge characteristics.

Term	Z&K Model calculations	Navratil Exp. Setup	Micor plasma plate Exp. Setup
Surface material	Al_2O_3	Al_2O_3	Al_2O_3
Dielectric material	Al_2O_3	Al_2O_3	PDP-glaze
Thickness dielectric	$1500\mu m$	$700\mu m$	$30\mu m$
Permittivity(ε_r) (Rel.Diel. Constant)	9.0	9.4	12.0
Electrode are(A)	12 cm^2(round)	4 cm^2(square)	0.5 cm^2(per line)
Capacitance per cm^2	2.5pF	6.0pF	160pF
discharge gap (d)	5 mm	5 mm	80 μm
pd(Torr·cm)	380	380	6
Sustain voltage(V)	1500	700	300
Field strength($E = V_{sus}/d$)	$3 \cdot 10^5$	$1.4 \cdot 10^5$	$4 \cdot 10^6$
Reduced field(E/p)	$4V/(Torr \cdot cm)$	$2V/(Torr \cdot cm)$	$50V/(Torr \cdot cm)$
Sustain frequency	10-25kHz	10kHz	20-100kHz

5.5.6 Comparison with an atmospheric Argon discharge in the Micro Array Plate

We also tested the Al_2O_3 coated Micro Plasma Plate with 100% argon gas. In that case no uniform glow mode is found. Instead, similar to Navratil with argon gas and Al_2O_3 surface, we observe a strong filamentary discharge as shown in figure 5.35. The plate can only be ignited using a Tesla coil.

The resulting spectra are shown in figure 5.36 and 5.37. Also in this case we observe a strong 309 nm OH emission, but the 391 nm N_2^+ emission line is virtually absent. The reason for this is, that argon meta-stables with an energy of 11.6 eV do not have enough energy to ionize nitrogen directly (ionization energy is 15.6 eV), contrary to helium meta-stables, that have an excitation energy of 20 eV , respectively. Therefore the argon metastables are relatively abundant, and the energy of 11.6 eV is sufficient to dissociate water molecules.

Moon compared the intensity of the 309nm OH line for 100% helium and 100% Ar in a RF excited system, and found that the OH intensity for argon is 5 times smaller, compared to 100% helium [37], see figure 5.34.

According to Hibert at al the OH ($A^2\Sigma^+$) generation in an argon discharge is by the
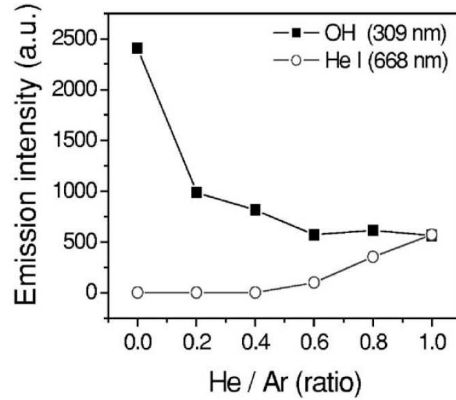
Figure 5.34: Emission intensity from excited helium atom(668 nm) and OH (309 nm) at various He/Ar mixing ratios reported by Moon et al [37].

dissociation of water by Ar-metastables [42]

$$Ar^*(4p) + H_2O \rightarrow Ar(3p) + OH^*(A^2\Sigma^+) + H \tag{5.11}$$

$$OH^*(A^{2+}) + H_2O \rightarrow OH(X^2\Pi) + H_2O \tag{5.12}$$
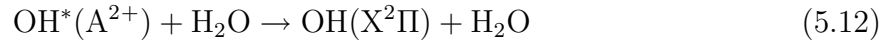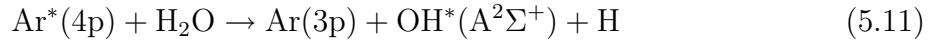
There is equilibrium between OH($A^2\Sigma^+$) production in reaction (5.11) and the quenching of this last with water molecule in reaction (5.12)

From the results with both the helium and the argon discharges, we conclude that at in non- hermetic systems at one atmosphere, in both cases strong OH emission is generated.

The mechanism however might be different. Helium dimer photons can directly dissociate water molecules. The argon dimer photons however have an energy of only 9.84 eV (126 nm), compared to 17.7 eV for the helium dimer, while the metastables cannot ionize N_2.

Therefore in atmospheric helium, maybe photo-dissociation of water is responsible for the OH generation, while in argon the generation of OH is by by argon metastables.

In a follow-up study, focused on argon based gas discharges, the emission properties of the Micro Array Plasma Plate, with different ratios of helium-argon, will be analyzed in more detail.

5.5.7 Al_2O_3 surface as a possible source of priming electrons

For the ignition of an argon or a nitrogen discharge a dielectric barrier is often made from a special electret material like Teflon or PET. Electrons stored in the electret material
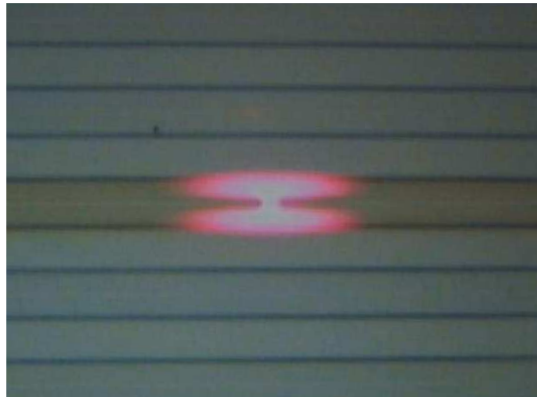
Figure 5.35: "H"patten Argon discharge on the Micro Plasma plate using a sustain frequency of 100 kHz and argon flow rate of 2 l/min.

during one cycle of the waveform, are released again after each voltage reversal. In this way a uniform glow discharge can also be made with either argon or nitrogen gas [26].

Al_2O_3 might also be used as a source of stored priming electrons in the case of a surface plasma plate. When Al_2O_3 is evaporated by Electron Beam deposition, like in our case, the resulting layer contains a high density of oxygen defects, called F-centers (This name was given in the past, because of the discoloration that is produced by them; the letter F indicates the German word Farbe, meaning color)

These oxygen defects can easily be filled by either a [OH]-hydroxyl ion, or by a [H]-hydride ion. In both cases these ions create stable electron traps just below the conduction band, from which priming electrons can easily be created, after voltage reversal, by the high field strength in the Micro Array Plasma Plate.

The emission spectrum for neon by Navratil et al shows, in addition to the line spectra, also a continuum of emission, with a (broad) maximum at about 280nm. This phenomenon so far is unexplained. On a possible explanation would be, that this emission originates from the Al_2O_3 surface, as a result of electron-hole pair recombination, created by the excitation by neon dimer UV light, which has an energy sufficient to excite the Al_2O_3 bandgap; it is not clear however, why the helium dimer radiation does not produce the same effect.

Figure 5.36: Spectrum in blue region of argon discharge on micro plasma plate using a sustain frequency of 100 kHz and argon flow rate of 2 l/min.

5.6 Conclusions

The micro plasma plate with surface discharge in helium is a promising tool for the application of bio-medical, such as sterilization and the treatment of skin diseases and food. More measurement for further understanding the mechanism of creating the OH emission is needed. In order to be applied for the bio- or food treatment the research to replace the quartz window with porous film is also needed. We have tested the atmospheric dielectric surface discharge using a Micro Plasma Plate in helium at atmospheric pressure, with the plate coated by Al_2O_3. Embedded electrodes were used, separated by a discharge gap of 70 μm. Stable and uniform atmospheric discharges were achieved by applying a 300 V sustain voltage at frequencies from 20 -100 kHz. We compared the results with those obtained for other helium atmospheric dielectric discharge systems. In the "non-hermetic" atmospheric pressure discharge system, a stronger OH (309 nm) emission was obtained, compared to a DBD surface discharge. The OH emission in our case might be created by photo-dissociation. We also found that the intensity of the OH emission strongly changed with the ratio of nitrogen leaking into the discharge system (by changing the helium flow rate). The duration of the OH emission in each half cycle is more than 1.2 μs, which is much longer than the duration of the discharge current (only 0.2-0.3 μs). The peak intensity of the OH emission has about 0.7 μs delay compared to the current peak. The research shows that the breakdown voltage increased when the applied frequency is decreased down to 20 kHz. This phenomena might be explained by the limited lifetime of the metastable particles, in the gas between voltage reversals. The research also shows a strong time dependent emission at high sustain frequencies. This could be the result of two processes
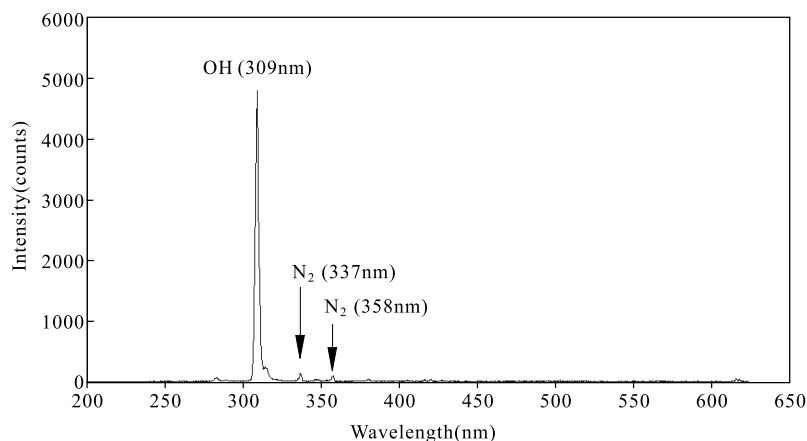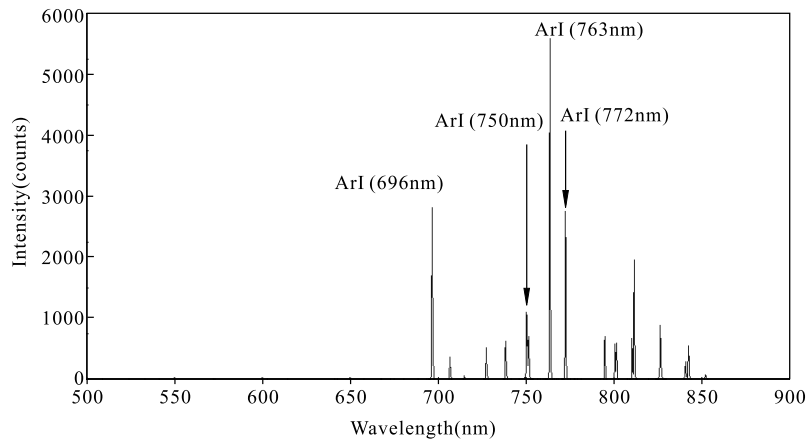
Figure 5.37: Spectrum in red region of argon discharge on micro plasma plate using a sustain frequency of 100 kHz and argon flow rate of 2 l/min

active at the same time: cleaning of the Al_2O_3 surface, thereby improving the secondary electron emission, and desorption of water, thereby depleting the source for OH radicals.

The micro plasma plate with a surface discharge in atmospheric helium is a promising tool for the application of bio-medical, such as sterilization and the treatment of skin diseases and food. More measurements are needed for further understanding the mechanisms of the creation and maximization of the OH emission. In order to be applied for the bio- or food treatment, the currently used quartz window will have to be replaced by a porous film.

References

[1] M. Moisan, J. Barbeau, M. C. Crevier, J. Pelletier, N. Philip, and B. Saoudi. Plasma sterilization. methods and mechanisms. *Pure Appl. Chem.*, 74(3):349–358, 2002.

[2] N. Philip, B. Saoudi, M.C. Crevier, M. Moisan, J. Barbeau, and J. Pelletier. The respective roles of UV photons and oxygen atoms in plasma sterilization at reduced gaspressure the case of $N_2 - O_2$ mixtures. *IEEE Trans. Plasma Sci.*, 30(4):1429–1436, 2002.

[3] I. A. Soloshenko, V. V. Tsiolko, V. A. Khomich, A. V. Shchedrin, A. I.and Ryabtsev, V. Yu. Bazhenov, and I.L. Mikhno. Sterilization of medical products in low pressure glow discharges. *Plasma Phys. Rep.*, 26:792–800, 2000.

[4] S. F. Cogan, D. J. Edell, A. A. Guzelian, Y. Ping Liu, and R. Edell. Plasma enhanced chemical vapor deposited silicon carbide as an implantable dielectric coating. *J. Biomed. Mater. Res.*, 67(3):856–867, 2003.

[5] R. d'Agostino, P. Favia, Ch. Oehr, and M. R. Wertheimer. Plasma processes and polymers: 16th International symposium on plasma chemistry Taormina, Italy, June 22-27, 2003. *ISBN: 3-527-40487-2*, 2005.

[6] M. Mattioli-Belmonte, G. Lucarini, L. Virgili, G. Biagini, L. Detomaso, P. Favia, R. D'Agostino, R. Gristina, A. Gigante, and C. Bevilacqua. Mesenchymal stem cells on plasma-deposited acrylic acid coatings: an in vitro investigation to improve biomaterial performance in bone reconstruction. *Journal of Bioactive and Compatible Polymers*, 20(4):343–360, 2005.

[7] K.H. Becker, U. Kogelschatz, K.H. Schoenbach, and R.J. Barker. Non-equilibrium air plasmas at atmospheric pressure. *IOP publishing ISBN 0-7503-0962-8*, 2005.

[8] H.W. Selwyn, G.S.and Herrmann, J. Park, and I. Henins. Materials processing using an atmospheric pressure,RF-generated plasma source. *Contrib. Plasma Phys.*, 6:610–619, 2001.

[9] W. J. M. Brok, M. D. Bowden, J. van Dijk, J. J. A. M. van der Mullen, and G. M. W. Kroesen. Numerical description of discharge characteristics of the plasma needle. *J. Appl. Phys.*, 98(1):013302–013302–8, 2005.

[10] J.Y. Jeong, S.E. Babayan, V.J. Tu, J. Park, I. Henins, R.F. Hicks, and G.S. Selwyn. Etching materials with an atmospheric-pressure plasma jet. *Plasma Sources Sci. Technol.*, 7:282–285, 1998.

[11] J. Park, I. Henins, H. W. Herrmann, and G. S. Selwyn. Discharge phenomena of an atmospheric pressure radio-frequency capacitive plasma source. *J. Appl. Phys.*, 89(1):20–28, 2001.

[12] *www.erbe-med.de.*

[13] J. Waye. Delivery system for argon coagulator offers non-contact method for control of GI bleeding. *Gastroenterology Endoscopy News, June*, 1997.

[14] U. Kogelschatz. Filamentary, patterned, and diffuse barrier discharges. *IEEE Transactions on Plasma Science*, 30(4):1400–1408, 2002.

[15] F. Massines, A. Rabehi, Ph. Decomps, R. Ben Gadri, P. Segur, and Ch. Mayoux. Experimental and theoretical study of a glow discharge at atmospheric pressure controlled by dielectric barrier. *J. Appl. Phys.*, 83(6):2950–2957, 1998.

[16] K. Okazaki and T. Nozaki. Ultrashort pulsed barrier discharges and applications. *Pure Appl. Chem.*, 74(3):447–452, 2002.

[17] K.R. Stalder, J. Woloszko, I.G. Brown, and C.D. Smith. Repetitive plasma discharges in saline solutions. *Appl. Phys. Lett.*, 79(27):4503–4505, 2001.

[18] J. Woloszko, K.R. Stalder, and I.G. Brown. Plasma characteristics of repetitively-pulsed electrical discharges in saline solutions used for surgical procedures. *IEEE Trans. Plasma Sci.*, 30(3):1376–1383, 2002.

[19] K.R. Stalder, D.F. McMillen, and J. Woloszko. Electrosurgical plasmas. *J. Phys. D: Appl. Phys.*, 38(11):1728–1738, 2005.

[20] V. Léveillé and S. Coulombe. Design and preliminary characterization of a miniature pulsed RF APGD torch with downstream injection of the source of reactive species. *Plasma Sources Sci. Technol.*, 14:467–476, 2005.

[21] R. Pompl, T. Shimizu, H.-U. Schmidt, W. Bunk, F. Jamitzky, B. Steffes, K. Ramrath, B. Peters, W. Stolz, T. Urayama, R. Ramasamy, S. Fujii, and G.E. Morfill. *Proc. 6th International conference on Reative Plasma and 23rd Symposium on Plasma Processing, Matsushima/Sendai, Japan, January 24-27*, 2006.

[22] J. Janca, M. Klima, P. Slavicek, and L. Zajickova. HF plasma pencil- new source for plasma surface processing. *Surf. Coat. Technol.*, 116:547–551, 1999.

[23] M. Laroussi and X. Lu. Room-temperature atmospheric pressure plasma plume for biomedical applications. *Appl. Phys. Lett.*, 87(14):113902(3), 2005.

[24] E. Stoffels, A.J. Flikweert, W.W. Stoffels, and G.M.W. Kroesen. Plasma needle: a non-destructive atmospheric plasma source for fine surface treatment of (bio)materials. *Plasma Sourcess Sci. Technol.*, 11:383–388, 2002.

[25] R. Roest, V. A. Maiorov, Yu. B. Golubovskii, J. F. Behnke, and M. Schmidt. Study of a helium atmospheric pressure dielectric barrier discharge at 100kHz. *ICPIG*, 2004.

[26] Y. B. Golubovskii, V. A. Maiorov, P. Li, and M. Lindmayer. Effect of the barrier material in a Townsend barrier discharge in nitrogen at atmospheric pressure. *J. Phys. D: Appl. Phys.*, 39(8):1574–1583, 2006.

[27] C. Anderson, M. Hur, and P. Zhang. Two-dimensional space-time-resolved emission spectroscopy on atmospheric pressure glows in helium with impurities. *J. Appl. Phys.*, 96:1835–1839, 2004.

[28] P. Zhang and U Kortshagen. Two-dimensional numerical study of atmospheric pressure glows in helium with impurities. *J. Phys. D: Appl. Phys.*, 39(1):153–163, 2006.

[29] Y. P. Raizer. Gas discharge physics. *Berlin, Springer*, 1997.

[30] J. M. Pouvesle, A. Bouchoule, and J. Stevefelt. Modeling of the charge transfer afterglow excitecd by intense electrical discharges in high pressure helium nitrogen mixtures. *J. Chem. Phys.*, 77:817–825, 1982.

[31] Z. Navratil, R. Brandenburg, D. Trunec, A. Brablec, P. Stahel, H-E Wagner, and Z. Kopecky. Comparative study of diffuse barrier discharges in neon and helium. *Plasma Sources Sci. Technol.*, 15(1):8–17, 2006.

[32] A. Ricard, P. Decomps, and F. Massines. *Surf. Coat. Technol.*, 112:1–4, 1999.

[33] R. Sankaranarayanan, B. Pashaie, and S. K. Dhali. Laser-induced fluorescence of OH radicals in a dielectric barrier discharge. *Appl. Phys. Lett.*, 77(6):2970–2972, 2000.

[34] Y. B. Golubovskii, V. A. Maiorov, J. Behnke, and J. F Behnke. Modelling of the homogeneous barrier discharge in helium at atmospheric pressure. *J. Phys. D: Appl. Phys.*, 36(1):39–49, 2003.

[35] A. J. Palmer. A physical model on the initiaiton of atmospheric-pressure glow discharges. *Appl. Phys. Lett.*, 25(3):138–140, 1974.

[36] J. I. Levatter and Shao-chi . Necessary conditions for the homogeneous formation of pulsed avalanche discharges at high gas pressure. *J. Appl. Phys.*, 51(1):210–222, 1980.

[37] Se Youn Moon, Jewoo Han, and W. Choe. Control of radio-frequency atmospheric pressure argon plasma characteristics by helium gas mixing. *Physics of Plasmas*, 13:013504, 2006.

[38] A. Rahman, V. Yalin, A.P.and Surla, O. Stan, K. Hoshimiya, Z. Yu, E. Littlefield, and G. J. Collins. Absolute UV and VUV emission in the 110-400nm region from 13.56 MHz driven hollow slot microplasmas operating in open air. *Plasma Sources Sci. Technol.*, 13:537–547, 2004.

[39] I. E. Kieft, E. P. v. d. Laan, and E. Stoffels. Electrical and optical characterization of the plasma needle. *New J. Phys.*, 6:149, 2004.

[40] V. V. Elsbergen, P. K. Bachmann, and T. Juestel. Ion-induced secondary electron emission a comparative study. *SID Int. Symp. Dig. Tech. papers*, pages 220–223, May 2000.

[41] W. E. Wentworth, Q. Yang, S. Wiedeman, S.D. Stearns, and J. Madabushi. Excited species from a pulsed discharge in helium at one atmosphere pressure. *spectra*, 49(9):1282–1298, 1995.

[42] C. Hibert, I. Gaurand, O. Motret, and J. M. Pouvesle. [OH(x)] measurements by resonant absorption spectroscopy in a pulsed dielectric barrier discharge. *J. Appl. Phys.*, 85:7070–7075, 1999.

Chapter A

Appendix

A.1 Helium and Al_2O_3 surface effects

A.1.1 Energy levels in helium

Figure A.1 shows the Scheme of the excited states of atomic helium.

A.1.2 Secondary electron generation by Auger neutralization at the dielectric surface

The ionization energy E_i is 24.6, 21.6, 15.8, 14.0, and 12.1 eV respectively for helium, neon, argon, krypton, and xenon respectively.

For Auger neutralization the condition $E_i > 2(E_g + \chi)$ has to be fulfilled. For MgO with $E_g = 7.8$ eV and $\chi \sim 1$ eV it means that only helium and neon ions can generate secondary electrons at the MgO surface by Auger neutralization. The same is true for Al_2O_3 with $E_g = 8.4$-9.0 eV. Argon ions on Al_2O_3 cannot generate secondary electrons by Auger neutralization, and therefore have a very low ion induced secondary electron emission.

A.2 Secondary electron emission and the Paschen curve

The ion-induced SEE coefficient γ_i is defined as the ratio of the number of electrons emitted and the number of ions incident on surface. It depends strongly on the type of cathode material and on the type of ions, and determines the firing voltage of a discharge. The
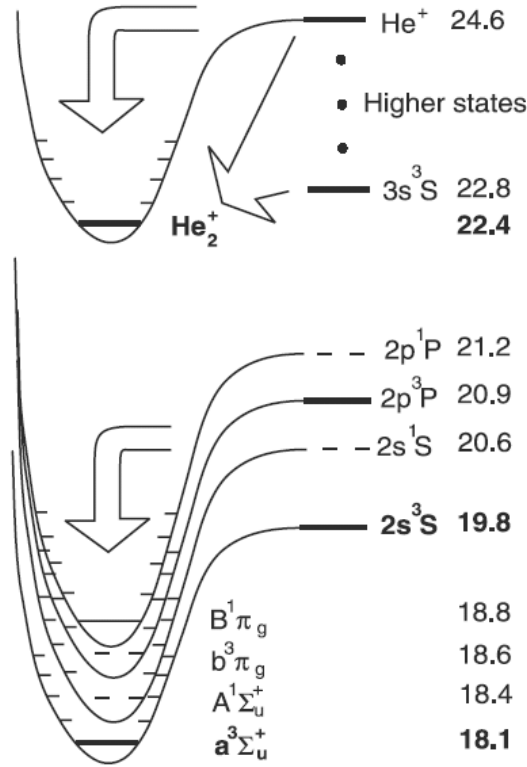
Figure A.1: Scheme of the excited states in atomic helium [1].

value of γ_i can be calculated directly from the ionisation cross section, as depicted in the process shown in figure A.3(a). The value of a is a function of the value of E/p, as shown given in figure A.3(b) for the different gases.

The Paschen curve is the relationship between the firing voltage of a discharge and the value of pd, where p is the gas pressure and d is the discharge gap. For low-pressure levels it can be described analytically for pure gases. For atmospheric pressure level the Paschen curve, as published by Raizer [3] applies:

$$V_F = \frac{D^2 \cdot p \cdot d}{(ln\frac{C \cdot p \cdot d}{ln(1/\gamma+1)})^2} \qquad (A.1)$$

where $V_f = V_g$(firing) is the gap voltage at which firing occurs, and γ(gamma) is the secondary electron emission coefficient. C and D are gas dependant constants, and are given in table A.1.

From table I we see that this formula applies for the range used in our Micro Plasma Array Plate, with E/p = 50 V/(Torr.cm). Please note that this formula and the associated constants deviate from the formula, applicable for low pressure levels, and mostly quoted in
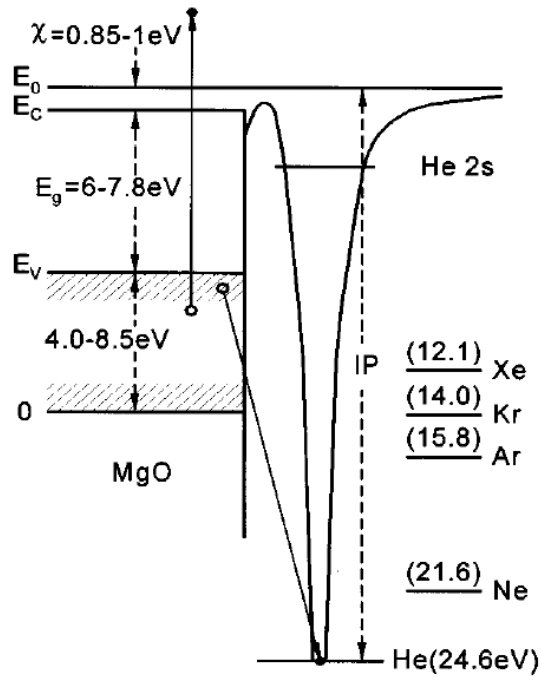
Figure A.2: Energy diagram showing potential emission of secondary electrons via Auger neutralization of the He ion; the example is for an MgO surface. The gas-phase ionization potentials of various noble gas ions are given in units of eV. [2]

the text books; that formula gives wrong results for atmospheric discharges, and should not be used in our case. Please also note that the formula strictly applies only for a standard DBD vertical discharge, and not for a surface discharge.

Figure A.4 shows the calculated Paschen curves for helium; these curve the gap voltages at which breakdown is expected to occur, for different values of gamma. The actual value of gamma can become higher than the maximum possible value of γ_i =0.5 of Auger neutralisation. As shown by Elsbergen and Bachmann [4–6], for small E/p (i.e., large pd values), γ_{eff} is strongly influenced by photo-induced emission processes [7] and is usually much higher than γ_i.

For a gamma of 0.1 in the case of the DBD system of Navratil, the gap breakdown voltage following from the Raizer curve is 1750 V, compared to the 1200 V reported. The lower gap breakdown voltage might be explained by the effect of additional photo-electron emission at low E/p values of system of Navratil [7].

In the case of an AC surface discharge, there is not a constant pd value. Instead, effectively the discharge gradually grows to a much higher value, while the ionisation front moves over the protective Al_2O_3 surface, and then the cycle is repeated, by starting again
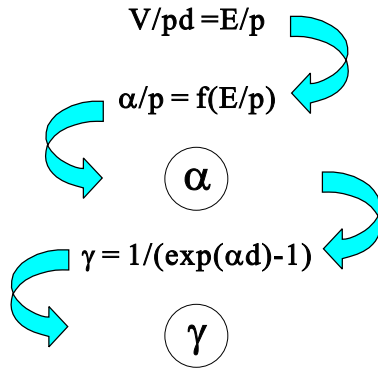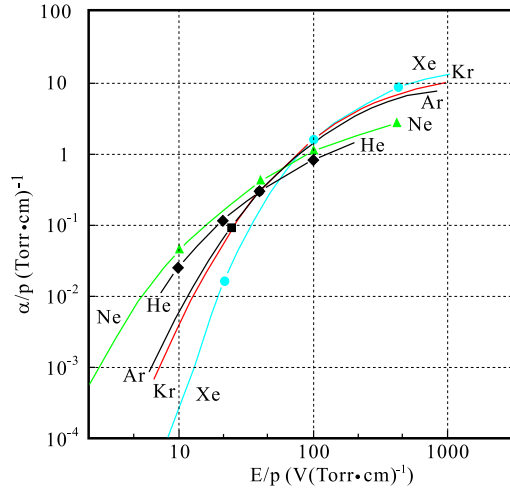
(a)   (b)

Figure A.3: a):Electron generation by ionisation, and b): dependence of α/p on E/p for several gases.

at its lowest value.

In the case of our system, the gap breakdown voltage value of about 240 V (see figure 5.17) would correspond to pd = 15 (Torr · cm), for a gamma value of 0.1. This translates into an effective gap length of about 200 μm, instead of the geometrical gap length of 70 μm. Alternatively, the effective gamma value might be lower than the value of 0.1.

The actual value of gamma can become higher than 0.5, for instance in case of photo-electron emission.

A.3   Gap and firing voltage measurement

The voltage across the discharge gap, can be calculated directly from the current, as was done in chapter 5 of this thesis, by using the formulas (5.1) and (5.2).

Alternatively, the measurement of the Paschen curve, can be made in the way described by Elsbergen en Bachmann [4–6]. This setup is shown in figure 3. By plotting the so-called "Lissajous" figure, when an external reference capacitor C_{Ref} ,of known value, is put in series with the DBD cell, the plasma firing voltage V_f can be determined. Firing of the plasma results in charge transfer between the cell and C_{Ref}. By making the reference capacitor much larger than the DBD capacitance, the effect of charge transfer can be neglected. We can then plot the voltage V_R across the reference capacitor, as a function of the applied voltage Va, and determine the actual firing voltage $V_f = V_g$ of our cell from
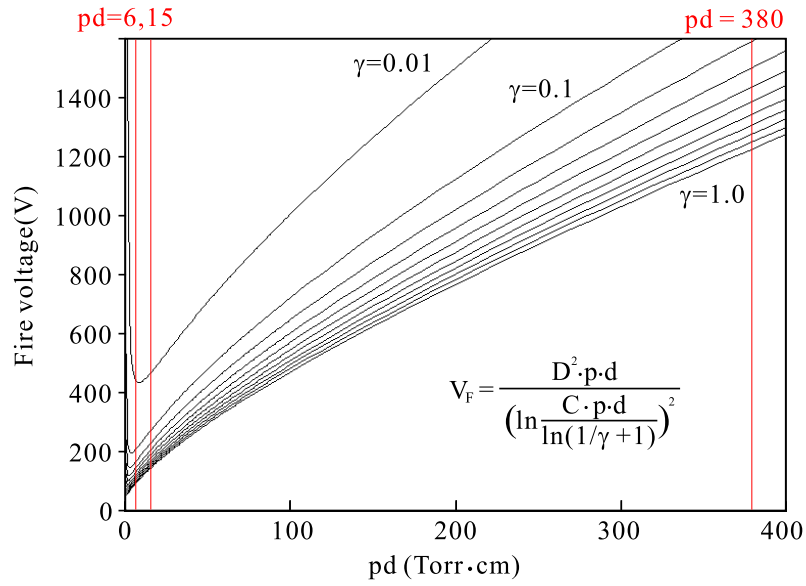
Figure A.4: Calculated Paschen curve for helium using formula 1 by Raizer [3].

Figure A.5: Set-up of the Paschen curve measurement method, by plotting a "Lissajous" figure, with an external reference capacitor put in series with the DBD cell C_{Ref} is the reference capacitor, C_{diel} is the capacitance of the dielectric substrate and C_{gap} of the discharge gap.

Table A.1:

Gas	C $(Torr \cdot cm)^{-1}$	D $V \cdot (Torr \cdot cm)^{-1/2}$	E/p rang of validity $(V \cdot (Torr \cdot cm)^{-1})$
He	4.4	14.0	<100
Ne	8.2	17.0	<250
Ar	29.2	26.6	<700
Xe	65.3	36.1	<1200

the Lissajous data.

The plot results in a straight line, without a plasma discharge, and in a "Lissajous"-like figure A.5(b), as soon as the plasma ignites. Upon increasing the applied voltage V_{appl} to the firing voltage V_f, the plasma ignites. The values Vs and $V_{\Delta R}$ shown in figure A.5 can then be used to determine the voltage V_f across the discharge gap, for which the breakdown actually occurs.
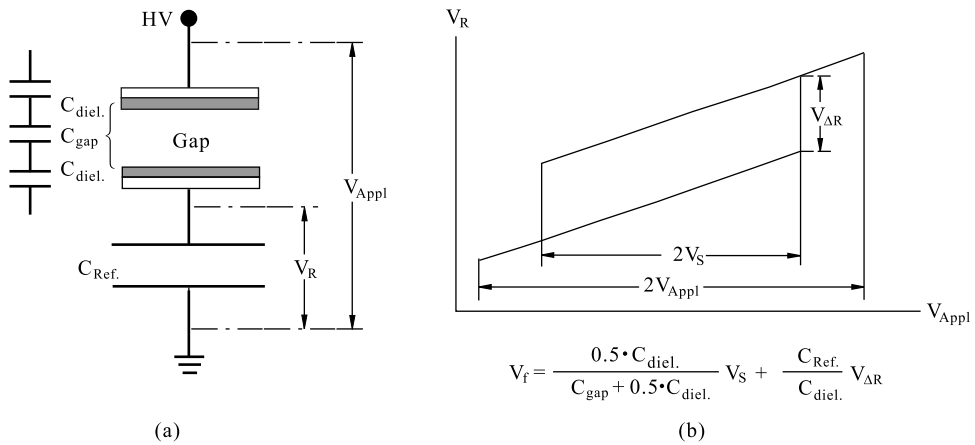
Figure A.5(a) is the set-up of the Paschen curve measurement method, by plotting a "Lissajous" figure, with an external reference capacitor put in series with the DBD cell. C_{Ref} is the reference capacitor, C_{diel} is the capacitance of the dielectric substrate and C_{gap} of the discharge gap, when there is no discharge.

References

[1] Y. B. Golubovskii, V. A. Maiorov, J. Behnke, and J. F Behnke. Modelling of the homogeneous barrier discharge in helium at atmospheric pressure. *J. Phys. D: Appl. Phys.*, 36(1):39–49, 2003.

[2] K. S. Moon. Electron ejection from MgO thin films by low energy noble gas ions: Energy dependence and initial instability of the secondary electron emission coefficient. *J. Appl. Phys.*, 86(7):4049–4051, 1999.

[3] Y. P. Raizer. Gas discharge physics. *Berlin, Springer*, 1997.

[4] V. V. Elsbergen, P. K. Bachmann, and T. Juestel. Ion-induced secondary electron emission a comparative study. *SID Int. Symp. Dig. Tech. papers*, pages 220–223, May 2000.

[5] V. V. Elsbergen, P. K. Bachmann, and G. Zhong. Ion induced secondary electron emission: Single Crystals and Surface Modification. *Intl. Display Workshop 2000, IDW2000 Conf. Proc.*, page 687, 2000.

[6] P.K. Bachmann, V.v. Elsbergen, D.U. Wiechert, G. Zhong, and J. Robertson. CVD diamond: A novel high $\gamma-$ coating for plasma display panels. *Diamond and Related Materials*, 10:809, 2001.

[7] A. V. Phelps and Z. Lj. Petrovic. Cold-cathode discharges and breakdown in argon: surface and gas phase production of secondary electrons. *Plasma Sources Sci. Technol.*, 8(3):R21–44, 1999.

Summary

One of the most important discharge parameters is the electrical field strength. In glow discharges, this is the driving force behind many processes. Many applications that use a glow discharge depend on the behavior at the boundary, and the electric field is closely connected with other discharge properties in this region. Therefore it is necessary to understand the spatial distribution of the electrical field in a discharge. However, it is very difficult to measure. The common method is to use electrical probes, but this is of limited use because of perturbation problems.

In this thesis, a spectroscopic method for measuring electrical fields is reported that is based on the Stark effect. This method is applied for both krypton and xenon gas discharges. This method is based on comparing the experimentally determined position and shift of spectral lines with the results of calculations based on solving the Schrödinger equation.

A good agreement between calculations and experimental results was achieved for the excitations from $5s$ to nf for krypton and $6s'$ to nf for xenon, where n is the principle quantum number. It has been shown that a good accuracy can be obtained at high electrical field strengths and at large principle quantum numbers.

In addition to these f state excitations, we also observed the Stark effect for the p states in noble gas atoms. A simplified hydrogen-like calculation was applied to the p states of noble gas atoms, despite the complication of the Rydberg electrons penetrating the ionic core shells.

We find that there is a good agreement between the theoretical calculation and the experimental results. The resolution of the electrical field measurements using Stark shift of np levels is almost the same as for the Stark splitting of f levels in the case of argon or krypton. For higher transitions, excited from the metastable state to the p state, however, it is easier to measure the Stark effect for the p-states.

For xenon atoms exited from $6s'[1/2]_0$, the intensities of both Laser optogalvanic (LOG) signals are almost the same. When measuring the electric field in the range of 500-1500V/cm, a higher resolution can be obtained by using $13p$ level shifts instead of $13f$.

Similar effects are also visible in the nf spectra of krypton and argon. However, when using np states to measure the electric field, an accurate calibration of the excitation wavelength is needed. Also, in a high field, the shift of the np levels is less sensitive than the splitting of nf states.

In a further research effort, we used an ICCD camera to study the plasma breakdown in PDP-like micro-gap discharges. The results were compared to systems with a much larger gap and high voltages. The measurement of the plasma light emission provides a good insight of the breakdown process in each situation, and the results allow us to identify that the crossing of an ionization wave is the critical feature of the breakdown process in all these different systems. The influence of the different material properties and the different geometries is also described.

An atmospheric cold plasma source was also investigated. A linear array of dielectric barrier discharges in the form of a flat plate coated with an Al_2O_3 layer was used to generate a plasma in helium gas at atmospheric pressure, in the presence of impurities from air. The discharge gap was 70 μm and the dielectric barrier was 30 μm thick.

At one atmosphere, stable discharges are achieved using a square wave external voltage of about 300 Volt at frequencies from 20-100 kHz. The spectrum of the emitted light shows strong emission lines of the OH radical at 309 nm, in addition to N_2^+ (391 nm) and helium emission lines. The intensity of these lines was determined as a function of the applied frequency and the helium flow rate, and the time dependent behavior was studied in detail.

It is concluded that the OH (309 nm) emission at atmospheric pressure is especially strong because of the photo-dissociation process, that might be responsible for the OH creation. The micro-plasma array plate with surface discharges in helium promises to be an promising tool for the creation of OH radicals and the generation of non-coherent 309 nm radiation, both of which might be used of sterilization or treatment of skin diseases.

SAMENVATTING

De elektrische veldsterkte is een van de belangrijkste parameters voor gasontladingen. In glimontladingen is het de drijvende kracht achter vele processen. Veel toepassingen van een glimontladingen worden bepaald door de eigenschappen aan de grenzen, en het elektrische veld is nauw verbonden met de andere eigenschappen in dat gebied. Het is daarom noodzakelijk om de ruimtelijke verdeling van de elektrische veldsterkte in een ontlading te kennen, maar dat is moeilijk te meten. De meest gebruikelijke methode is het gebruik van sondes, maar die zijn slechts beperkt toepasbaar vanwege de complicatie van de verstoring van het te meten veld.

In dit proefschrift wordt verslag gedaan van een spectroscopische methode gebaseerd op het Stark-effect voor het meten van het elektrische veld in een glimontlading, en de methode wordt toegepast op een krypton en een xenon gas ontlading. Deze methode voor het bepalen van de elektrische veldsterkte is gebaseerd op de resultaten van laser optogalvanische spectra (LOG) en berekeningen rond het oplossen van de Schrödinger-vergelijking.

We vinden een goede overeenkomst tussen de berekende en gemeten waarden voor aanslagen vanuit de $5s$ toestand naar nf voor krypton en voor de $6s'$ overgangen naar de nf toestanden; Hierbij is n een geheel getal, het hoofd kwantum getal. Aangetoond wordt dat de hoogste nauwkeurigheid bereikt wordt in het geval van een zeer sterk elektrisch veld en voor een grote waarde van het kwantum getal n.

Naast de aanslagen vanuit de f-toestand hebben we ook metingen gedaan aan aanslag vanuit de p-toestand van edelgas atomen. Een vereenvoudigd waterstof-achtig atoommodel werd toegepast op de p-toestanden van edelgas atomen, ondanks het probleem van het doorkruisen van de electronbanen van de ionenkern, door Rydberg elektronen met een kleiner kwantum impulsmoment. We vinden een goede overeenkomst tussen de theoretische berekeningen en de experimentele resultaten. Het scheidend vermogen bij de metingen van de elektrische veldsterkte door middel van het Stark effect van de np-niveaus is bijna even goed als die voor de Stark splitsing voor de f-niveaus van argon of krypton. Voor de hogere overgangen, aangeslagen vanuit de metastabiele p-toestand, blijkt het gemakkelijker te zijn

123

om het Stark effect toe te passen op de f-toestanden.

Voor xenonatomen, aangeslagen vanuit de $6s'[1/2]_0$ toestand, zijn de intensiteiten van de LOG signalen bijna even groot. Voor het bepalen van veldsterktes van 500 - 1500 V/cm kan evenwel een hoger scheidend vermogen bereikt worden door gebruik te maken van $13p$ niveau overgangen in plaats van de 13 f niveaus. Vergelijkbare effecten worden gevonden voor de nf-spectra van krypton en argon. Wanneer we evenwel de np-niveaus gebruiken voor het meten van de elektrische veldsterkte, dan is een zeer nauwkeurige ijking noodzakelijk van de golflengte van het licht waarmee de toestanden worden aangeslagen. Bovendien zijn bij een hoge veldsterkte de np niveaus minder gevoelig voor niveausplitsing dan de nf-toestanden.

In hoofdstuk 4 gebruiken we een ICCD-camera voor het bestuderen van de gasontladingen bij een structuur gelijk aan die in plasma displays (PDP). De resultaten worden vergeleken met systemen met een veel grotere elektrode afstand bij veel hogere spanningen. De metingen van het uitgezonden zichtbare licht verschaffen een goed inzicht in het doorslagmechanisme in elk systeem en de resultaten laten zien dat het oversteken van het ionisatiefront het meest kritische verschijnsel is bij het doorslagproces in al deze verschillende systemen. Daarnaast wordt ook de invloed van de verschillen in materiaaleigenschappen en geometrieen beschreven.

In hoofdstuk 5 van dit proefschrift wordt een atmosferisch, koud plasma onderzocht. Een rij van ontladingen over het oppervlak van een dielectrisch materiaal (DBD) werd geanalyseerd. Een rij van elektrode-paren, ieder met een gasontladingsspleet van 30 μm, is begraven onder een 30 μm dikke dielectrische laag, die aan het oppervlak voorzien is van een dunne laag aluminiumoxide. Deze rij gasontladingen werd ontstoken bij atmosferische druk, in de aanwezigheid van onzuiverheden die vanuit de lucht het systeem kunnen binnendringen.

Bij een druk van één atmosfeer blijkt dat in dit systeem stabiele homogene ontladingen ontstaan bij het aanleggen van een wisselspanning van 300 Volt amplitude en een frequentie van 20.000 to 100 .000 Hz. Het spectrum van het uitgezonden licht vertoont de sterke emissielijnen van het OH-radikaal bij 309 nm golflengte, naast die van geïoniseerde stikstof moleculen N_2^+ bij 391 nm, en de helium-emissielijnen. De intensiteit van deze lijnen is gemeten als functie van de toegepaste frequentie en de helium-stroomsnelheid, en ook het tijdafhankelijke gedrag is in detail bestudeerd.

De conclusie is dat de emissie van OH (309nm) bij atmosferische druk bijzonder sterk zou kunnen zijn, speciaal door het fotodissociatie proces, waarbij de zeer kortgolvige (70-100nm) aangeslagen helium moleculen (H_2^* -dimeren) water splitsen in OH en waterstof atomen.

De micro-plasmaplaat, met oppervlakte ontladingen in atmosferisch helium, is een veel-

belovend instrument voor het genereren van OH radicalen en van niet-coherente 309nm straling, die beide gebruikt zouden kunnen worden voor sterilisatie doeleinden of het behandelen van huidziekten.

Acknowledgement

At the end of my Ph.D study in the group of Elementary Processes in Gas discharges (EPG) at Technische Universiteit Eindhoven (TU/e), looking back I'd like thank the people who help me to finish this thesis. I must say I could not have finished it without your encouragement and support.

First I'd like to thank my first supervisor Gerrit Kroesen. He has given me this chance to work and study in this beautiful country, live and know the friendly people here.

Special thanks to my second supervisor Harm Tolner for his generous help on the micro plasma plate and the PDP-like discharge, also his patient and friendly instructions and the discussions during the course of my studies were appreciated very much.

Thanks go to Mark Bowden, my copromotor. The contribution of this thesis about LOG measurements and plasma emission were under his direction. Especially it was his encouragement and patient direction in the early time when I arrived in the Netherlands. Also Eva Stoffels: thanks you for willing to be my copromotor after the departure of Mark Bowden. She brought me into a new research area - atmospheric cold plasmas.

I would like to give special thanks to Erik Wagenaars. We shared same lab and both of us were working on the Stark effect and plasma emission. A lot of help came from him during my Ph D. work, such as the discussions and suggestions on the experiment set-up, data processing and analysis, writing papers and also the Dutch translation in daylife.

I am grateful to all the technicians in the EPG group for their help in designing and building up the experimental set-up. Thanks go to Loek Baede for the discussions and knowledge on the optical and vacuum systems. It was Huib Schouten who helped me making the LOG box. Evert Ridderhof: thank you for helping me to solve the problems in the lab and the office desktop. Also Charlotte Groothuis shared her optical design experience and sport experience, even from where she is now on the high mountains of Chile .

I would like to thank Hjmalmar Mulders to help me to measure the spectra of the micro plasma plate and Wouter Brok to coach me to use the Plasimo code.

I am grateful to Rina Boom, our secretary, for her generous helps all the time.

Acknowledgement

I would like to thank my colleagues: Lukas Grabowski, Maxime Gendre, Raymond Sladek, Bart Broks, Tanya Nimalasuriya, Tanja Briels, Arjan Flikweet, Mark Beks, Nienke de Vries, Jan van Dijk, Michiel van den Donker, Bart Hartgers, Joost van der Mullen, Winfred Stoffels, Eddie van Veldhuizen. Also thanks to my ex-colleagues Xiaoyan Zhu, Misha Sorokin, Jerome Remy, Ingrid Kieft, Gabriela Paeva, Erik Kieft, Jaap Feijen.

I am grateful to Dr Gerrit Oversluizen and Daiyu Hayashi, in Philips Research Eindhoven and Philips Forschungslaboratorien Aachen to supply the PDP plate and PDP cells to me.

I'd like to thank all help from the friends in the Chinese student association in TU/e.

I would like to thanks my friends, Prof Zhao Hong, Dr. Jiang Kejian and Dr. Li Bin, in China to help my family to deal with many things.

I want to thank Prof. Sun Jian in Xi'an Jiaotong, with your recommendation, I got the opportunity to study in TU/e. I'm deeply grateful to my mother Jiang Shuzi and my father Jiang Bingzheng for their love, encouragement and support. I want to thank my brother Jiang Bo and his family for taking care of my parents during my stay in Netherlands.

Last I'm deeply grateful to my lovely wife Cheng Xiangming, it was her love, encouragement and support, which enabled me to finish this thesis. Thank to her for taking care of my parents when I was in the Netherlands. Thank her for taking care of our son and his study. I would like thank my son, Jiang Yifan. Your victories in cycling inspired me to face the difficulties and overcoming them.

Curriculum vitae

July 31, 1960   Born in Xi'an, Shaanxi Province, China

September 1979 - July 1983   Bachelor of science in physics,
                                         Dept. of Physics,
                                         Northwest University of China.

September July 1983 - August 1988   Teaching physics in
                                         Xidian University, China

September 1988 - July 1991   Master of mechanical manufacture,
                                         Dept. of mechanical Engineering,
                                         Xi'an Jiaotong University, China

July 1991 - April 2002   Teacher in Institute of
                                         laser and infrared application ,
                                         Dept. of Mechanical Engineering,
                                         Xi'an Jiaotong University, China

April 2002 - November 2006   Ph.D. research in the group:
                                         Elementary Processes in Gas Discharges,
                                         "Stark spectroscopy on rare gas atoms"
                                         Eindhoven University of Technology,
                                         The netherlands.